Title

Fracture sealing by mineral precipitation: The role of surface heterogeneities on precipitation-induced transport property alterations

Permalink

https://escholarship.org/uc/item/3d60n1wt

Author

Jones, Trevor

Publication Date

2018

UNIVERSITY OF CALIFORNIA,
IRVINE

Fracture sealing by mineral precipitation: The role of surface heterogeneities on precipitation-induced transport property alterations

DISSERTATION

submitted in partial satisfaction of the requirements
for the degree of

DOCTOR OF PHILOSOPHY

in Civil and Environmental Engineering

by

Trevor Jones

Dissertation Committee:
Associate Professor Russell Detwiler, Chair
Assissant Professor Mo Li
Professor Brett Sanders

2018

DEDICATION

This dissertation is dedicated to my wife and family, whose support and encouragement have guided me through my academic career.

TABLE OF CONTENTS

LIST OF FIGURES

ACKNOWLEDGMENTS

I would like to thank my advisor, Dr. Russell L. Detwiler for his guidance and encouragement to explore new, challenging ideas.

Special thanks to the members of my committee, Dr. Brett Sanders and Dr. Mo Li.

I would also like to thank Ricardo Medina for the thoughtful, and often light-hearted, discussion around the lab, classroom, and office.

I would like to thank the U. S. Department of Energy, the Henry Samueli Foundation, and the Department of Civil & Environmental Engineering for providing financial support for my Ph.D. degree.

CURRICULUM VITAE

Trevor Jones

EDUCATION

Doctor of Philosophy in Civil and Environmental Engineering **2018**
University of California, Irvine *Irvine, Ca*

Masters of Science in Civil and Environmental Engineering **2015**
University of California, Irvine *Irvine, Ca*

Bachelors of Science in Civil and Environmental Engineering **2013**
University of California, Irvine *Irvine, Ca*

RESEARCH EXPERIENCE

Graduate Research Assistant **2013–2018**
University of California, Irvine *Irvine, Ca*

Undergraduate Research Assistant **2011–2013**
University of California, Irvine *Irvine, Ca*

TEACHING EXPERIENCE

Teaching Assistant **2013-2018**
University of California, Irvine *Irvine, Ca*

Guest Lecturer **2014-2017**
University of California, Irvine *Irvine, Ca*

REFEREED JOURNAL PUBLICATIONS

Fracture sealing by mineral precipitation: The role of small-scale mineral heterogeneity **2016**
Geophysical Research Letters

Mineral precipitation in fractures: Using the level set method to quantify the influence of mineral heterogeneity on transport properties **2018**
Under Review

Mineral precipitation in fractures: When do surface heterogeneities matter? **2018**
In preparation

High-Resolution experiments on chemical oxidation of DNAPL in variable-aperture fractures: Delineation of three time regimes **2015**
Water Resources Research

REFEREED CONFERENCE PROCEEDINGS

Fracture sealing caused by mineral precipitation: The role of aperture and mineral heterogeneity on precipitation-induced permeability loss (*Invited, Poster Presentation*) **Dec 2017**
Fall Meeting AGU

Predicting mineral precipitation in fractures: The role of local heterogeneity on the feedback between precipitation and permeability (*Oral Presentation*) **Dec 2016**
Fall Meeting AGU

Experimental observations of calcite precipitation in fractures: The role of physical and chemical heterogeneity on the persistence of preferential flow paths (*Oral Presentation*) **Dec 2015**
Fall Meeting AGU

Fracture aperture alteration induced by calcite precipitation (*Oral Presentation*) **Jun 2015**
49th U.S. Rock Mechanics/Geomechanics Symposium, ARMA

Fracture-aperture alteration induced by calcite precipitation (*PosterPresentation*) **Dec 2013**
Fall Meeting AGU

Open Source Software

Level Set Single Fracture Reactive Transport `https://github.com/spl-detwiler/LS_SFRT`
A single-fracture reactive transport model developed in MATLAB. Flow and transport is simulated via finite-volume integration of the 2D depth-averaged Stokes and advection-diffusion-reaction equation. Fluid-rock reactions are simulated using the level set method, which allows for three-dimensional alteration of the fracture surfaces due to fluid-rock reactions.

ABSTRACT OF THE DISSERTATION

Fracture sealing by mineral precipitation: The role of surface heterogeneities on precipitation-induced transport property alterations

By

Trevor Jones

Doctor of Philosophy in Civil and Environmental Engineering

University of California, Irvine, 2018

Associate Professor Russell Detwiler, Chair

Fractures are often leakage pathways for fluids through low-permeability rocks that otherwise act as geologic barriers to flow. Flow of fluids that are in chemical disequilibrium with the host rock can lead to mineral precipitation, which reduces fracture permeability. When fracture surfaces contain a single mineral phase, mineral precipitation leads to fast permeability reduction and fracture sealing. However, the feedback between precipitation and permeability may be disrupted by mineral heterogeneities that localize precipitation reactions and provide paths of low-reactivity for fluids to persist over relatively long time-scales. In this dissertation, I explore the role of mineral heterogeneity on precipitation-induced permeability reduction in fractures. To do this, I use a combined experimental and numerical approach to test three hypotheses: (1) Mineral heterogeneity prolongs fracture sealing by focusing flow into paths with limited reactive surface area, (2) Precipitation-induced transport alterations at the fracture-scale are controlled by three-dimensional growth dynamics at the grain-scale, and (3) The effects of mineral heterogeneity become more pronounced as mineralogy and surface roughness become autocorrelated over similar length-scales.

Direct measurements of mineral precipitation using transmitted light methods in a transparent analog fracture show that mineral heterogeneity can lead to the progressive focusing of flow into paths with limited reactive surface area, which is in support of (1). In this experiment, flow focusing led to a 72% reduction in the max precipitation rate; measurements of the projected mineralogy show that this was due to focusing of large dissolved ion concentrations into regions that contained 82% less reactive surface area than the fracture-scale average. Results from a newly developed reactive transport model that simulates precipitation-induced fracture surface alterations as a three-dimensional process are in good qualitative agreement with these experimental observations. Comparison of these results with a reactive transport model that represents precipitation as a 1D alteration of the fracture surfaces show that this flow-focusing process is driven by lateral growth of reactive minerals across the fracture-plane, which supports (2). Lastly, results from simulations in fractures that contain varied degrees of heterogeneity show that precipitation leads to a competition between two feedbacks: (i) precipitation-induced reactive surface area enhancement, which increases precipitation rates, and (ii) precipitation-induced permeability reduction, which decreases precipitation rates. When surface roughness and mineral heterogeneity provide persistent paths of limited surface area, the reactive transport becomes very sensitive to local permeability reduction. Simulation results show that this prolongs the fracture-sealing process and can lead to a reduction in fracture-scale precipitation rate, which supports (3). Furthermore, the results presented in this dissertation demonstrate that predictions of fracture sealing by mineral precipitation can be easily misinformed by studies that ignore small-scale mineral heterogeneity and neglect the three-dimensional nature of precipitation-induced fracture surface alterations.

Chapter 1

Introduction

1.1 Motivation

Fluid transport through the Earth's crust is a central concern of Earth scientists, hydrogeologists, and engineers as it affects the structural evolution of crustal rocks (e.g., Bons, 2001; Dempsey et al., 2012; Audet and Burgmann, 2014; Anders et al., 2014), dictates water resource management strategies (Custodio, 2002; Lachassagne et al., 2005), and controls solute fluxes across environmental boundaries (Harvey and Bencala, 2010; Boano et al., 2014). The rate of fluid transport is controlled by two parameters: (a) the hydraulic gradient which is linked to local atmospheric and weather cycles, and (b) the permeability of the rock which is an intrinsic property of the geologic environment. While permeability is typically measured and interpreted as a static parameter, it is widely acknowledged that permeability varies both in space and time due to thermodynamic (e.g., Yong-Fei, 1993; Powell and Holland, 2010), chemical (e.g., Lasaga, 1984; Putnis, 2002), and mechanical stresses (e.g., Cook, 1992; Ameli et al., 2014) that control the rates at which crustal rocks are altered. Although the mechanisms controlling spatial and temporal permeability alterations have been studied extensively, predicting the sign and rate of these changes in nature remains challenging.

In deep consolidated rocks, permeability is largely controlled by fractures that are orders-of-magnitude more permeable than the surrounding rock matrix (Zimmerman and Bodvarsson, 1996; Berkowitz, 2002). However, as infiltrating fluids interact with minerals on the fracture surfaces, fluid-rock reactions can lead to mineral precipitation, which reduces fracture permeability. Evidence of these geochemically-induced permeability reduction processes persist throughout nature, from mineralized veins in bedrock outcrops (e.g., Okamoto and Sekine, 2011; Anders et al., 2014; Tokan-Lawal et al., 2015), to rock weathering profiles that quantitatively detail the transformation of consolidated rocks to unconsolidated sediments (White and Brantley, 2003; Marques et al., 2017). Laboratory measurements of mineralization and rock weathering provide support for the conceptual models that attribute these alteration processes to the coupling between reactive fluid flow and fracture surface alterations (Fisher and Brantley, 1992; White and Brantley, 2003; Fisher and Brantley, 2014). However, laboratory measurements of rock weathering and vein sealing often predict time-dependent alteration rates that are orders-of-magnitude larger than measurements acquired in the field (White and Brantley, 2003). Developing a quantitative understanding of the feedback between mineral precipitation and fracture permeability is critical to a mechanistic understanding of how low-permeability crustal rocks evolve over geologic timescales.

In addition to these natural phenomena, mineral precipitation-induced permeability alteration plays an important role in engineered environments that aim to utilize the subsurface for enhanced energy production and waste storage. For example, geothermal reservoirs often exist in tight-rock environments where fractures provide the dominant pathway for fluid flow and heat extraction (Henneberger and Browne, 1988; Rowland and Sibson, 2004; Dempsey et al., 2012). Combined injection/extraction of fluids that are in chemical disequilibrium with the host rock can lead to mineral precipitation and fracture permeability reduction (Pandey et al., 2014, 2018; van den Heuvel et al., 2018), which has the undesired effect of reducing energy extraction efficiencies. Alternatively, in subsurface reservoirs used to store anthropogenic CO_2 or heavy-metals, induced precipitation provides a promising mechanism to trap contaminants and limit transport across environmental systems (DeJong et al., 2006; Fujita et al., 2008; Ebigbo et al., 2012; Matter et al., 2016).

In these engineered environments, anthropogenically imposed far-from-equilibrium conditions may cause mineralization reactions to occur over much shorter timescales than natural weathering and sealing processes. Further, nearby injection/extraction of fluids at high pressures may induce large hydraulic gradients that perturb the precipitation processes by forcing flow in regions of decreasing permeability. Our understanding of how mineral precipitation affects formation properties in far-from-equilibrium conditions is limited.

1.2 Mineral precipitation in fractures

Mineral precipitation occurs when the local pore-fluids become oversaturated with dissolved ions that are readily incorporated onto the fracture surface. As precipitation depletes dissolved ions from solution, subsequent reactions become limited by transport processes that replenish dissolved ion concentrations within resident fluids. This replenishment process can occur via two mechanisms: (1) diffusion of dissolved minerals from the rock matrix to the fracture surfaces (Bons, 2001; White and Brantley, 2003), or (2) long-range advection of a supersaturated fluid that displaces resident pore-fluids (Boles et al., 2004; Hilgers and Urai, 2002).

Mineral precipitation under the conditions described in (1) are common during vein-filling processes within deep bedrock. In these deep environments, brittle deformation of the rock (e.g. fracture generation) reduces the pressure within the pore-fluids that fill the fracture void, which leads to precipitation of dissolved ions from solution onto the surrounding mineral facies (White and Brantley, 2003). As precipitation depletes dissolved ions from solution, diffusion from the surrounding matrix replenishes ion concentrations (Fisher and Brantley, 1992; Knoll et al., 2008). This constant replenishment of dissolved ions leads to uniform precipitation across the fracture surface that eventually fills the void, leaving a weakly cemented mineral vein. Increased mechanical stresses within the fracture will induce failure (Landrot et al., 2012), which again reduces local pore pressures and promotes precipitation. These "crack-seal" cycles are well-behaved and lead to the development of blocky precipitate structures that provide a detailed history of the mechanical evolution of the rock (Anders et al., 2014; Ankit et al., 2015).

My research will focus on precipitation that is driven by the displacement of local pore-fluids via long-range advection of a supersaturated solution. Precipitation that occurs under case (2) leads to a dynamic feedback between precipitation and local permeability, which alters the rate at which dissolved minerals are transported to reactive surfaces over time (Lee and Morse, 1999; Hilgers and Urai, 2002; Hilgers et al., 2003). Under these conditions, precipitation is influenced by the relative rates of dissolved ion transport (by both advection and diffusion) and reaction kinetics at the mineral surfaces (Battiato and Tartakovsky, 2011). When the mass flux onto the fracture surface is large relative to the advective flux through the fracture, precipitation is expected to remain focused near the fracture inlet. Lee and Morse (1999) and Hilgers and Urai (2002) separately examined this end-member scenario in a flat-walled fracture and demonstrated that at the time of fracture sealing, e.g. complete reduction in fracture permeability, large portions of the downstream end of the fracture remained void of precipitated minerals. Therefore, without alternate mechanisms that drive fluid further into the fracture over time, precipitation in a homogeneous fracture is only expected to seal portions of the fracture closest to the source of infiltrating fluids (Verma and Pruess, 1988; Singurindy and Berkowitz, 2005)

1.3 The role of fracture-surface heterogeneities

Real fractures contain surface roughness (Brown, 1995) and mineral heterogeneities (Glassley et al., 2002) that perturb the feedback between precipitation and permeability alteration. Chaudhuri et al. (2012) examined the role of surface roughness on precipitation-induced permeability reduction and showed that precipitation rates will be fastest in large apertures that carry the largest flux of dissolved ions. Because precipitation reduces fracture aperture, fluid-rock reactions in uniform-mineralogy fractures can progressively smooth the surfaces and cause small-aperture bands to form oriented perpendicular to the mean flow direction. These small-aperture bands lead to faster permeability reduction than would be expected if surface roughness is ignored (Verma and Pruess, 1988; Singurindy and Berkowitz, 2005). As suggested in the experiments performed by Lee and Morse (1999), this would cause large portions of the fracture to remain void of precipitated minerals at the time of fracture sealing.

Rapid permeability reduction may be disrupted by mineral heterogeneities on the fracture surface by allowing large-aperture paths void of reactive minerals to persist late into the reactive transport. Despite numerous investigations of mineral precipitation fractured rocks (Lee and Morse, 1999; Hilgers and Urai, 2002; Fujita et al., 2008; Chaudhuri et al., 2008, 2012) relatively few studies have focused on the influence of mineral heterogeneity on precipitation-induced permeability alterations (Menefee et al., 2017). This is due to significant challenges in measuring the distribution of minerals at the fracture-scale (White and Brantley, 2003; Li et al., 2007). Recent experimental measurements demonstrate that porous and fractured rocks exhibit mineral heterogeneity down to the pore scale (Peters, 2009; Ellis and Peters, 2016; Beckingham et al., 2016, 2017). However, because precipitation is expected progressively seal the fracture, the role of surface mineralogy on precipitation-induced permeability evolution has not been examined in detail.

1.4 Models of mineral growth

Efforts to predict the evolution of fracture transport properties resulting from precipitation-induced reactive surface alterations generally employ two different approaches: (i) mechanistic models that describe the dynamics of the free-boundary problem of a reactive mineral extending into the void-space of the fracture (e.g. Ankit et al., 2015; Wendler et al., 2016), or (ii) simplified models that ignore the dynamics of mineral growth in an effort to model the flow and transport processes that control local precipitation rates (e.g., Deng et al., 2018; Menefee et al., 2017, 2018).

Mineral precipitation driven by the displacement of local pore-fluids via the long-range advection of a supersaturated solution is typically modeled using (ii). In these cases, direct solution of the Navier-Stokes equations with boundary conditions defined along the fracture surfaces provide a rigorous solution of the three-dimensional velocity field (e.g., Boutt et al., 2006; Lee et al., 2015). Using this velocity-field, the three-dimensional advection-diffusion-reaction equation can be solved within the fracture to quantify reaction rates at the fracture surface (Szymczak and Ladd, 2009; Starchenko et al., 2016). Precipitation onto the fracture surface alters the local surface geometry, and thus the local boundary conditions, which requires adaptive meshing or embedded boundary methods to account for precipitation-induced surface alterations throughout the fracture transport (Molins, 2015; Starchenko et al., 2016; Li et al., 2010).

A more computationally efficient approach is to depth-average the flow and transport equations across the fracture aperture. This results in two-dimensional equations that provide a reasonable estimate of flow and reactive transport through rough-walled fractures (e.g., Detwiler and Rajaram, 2007; Szymczak and Ladd, 2011). However, these models typically represent reactive surface alterations using simple 1D alteration methods that ignore the dynamics of the free-boundary problem (Menefee et al., 2017). Measurements from naturally filled mineral veins and weathered rocks show that precipitation can lead to non-uniformly distributed, and arbitrarily oriented, cements (Okamoto and Sekine, 2011; Tokan-Lawal et al., 2015). Further, the development of geometrically non-uniform precipitates may have effects on fluid flow and dissolved ion transport that are not well-represented with simple surface alteration methods (Ankit et al., 2015; Wendler et al., 2016; Kling et al., 2017).

1.5 Research objectives

Recent core-scale studies of mineral precipitation in fractures demonstrate that mineral heterogeneity localizes precipitation throughout the reactive transport (Menefee et al., 2017, 2018). However, the short time-scales and simple modeling methods used to quantify the impact of mineralogy on fracture transport alterations limits our quantitative understanding of how these localized reactions affect fracture permeability over larger spatial and temporal scales. In this dissertation I use a combined laboratory and numerical approach to quantify the mechanisms that control precipitation-induced permeability alterations in a fracture. To do this, I test three hypotheses:

1.5.1 Mineral heterogeneity prolongs fracture-sealing by focusing flow into paths with limited reactive surface area.

Local precipitation rates are controlled by the balance between two processes: (1) dissolved ion transport to the mineral surface which replenishes ion concentrations, and (2) ion incorporation onto the mineral surface which depletes dissolved ion concentrations (Detwiler and Rajaram, 2007). Because precipitation reduces the fracture aperture, replenishment via (1) is expected to decrease over time which would reduce the local precipitation rate. Further, when interconnected paths of low-reactivity persist along the length of the fracture, progressive sealing of local apertures may focus flow into regions of low-reactivity, which can prolong the sealing process. To test this, I conducted an experimental investigation of precipitation in a heterogeneous fracture. During this experiment, I measured fracture aperture reduction rates and dissolved ion transport to quantify the effects of flow alteration on fracture reactivity and sealing. Results from this experiment are presented in Chapter 2.

1.5.2 Precipitation-induced transport alterations at the fracture-scale are controlled by the three-dimensional growth dynamics at the grain-scale.

Good agreement between observations from mineralized veins and mechanistic models that simulate precipitation as a free-boundary problem suggest that precipitation-induced fracture surface alterations are inherently three-dimensional (Ankit et al., 2015; Wendler et al., 2016; Kling et al., 2017). The high-computational expense of theses methods limit the application of these models to conditions in which precipitation is driven by advective processes. However, because precipitation rates will be fastest along the mineral face with the largest solute flux (Weeks and Gilmer, 2007), these three-dimensional alterations may be a first-order mechanism that drives transport alterations across the fracture. To test this hypothesis, I developed a reactive transport model that employs a three-dimensional surface alteration method to model mineral precipitation under advection-dominated transport conditions. To quantify the impact of three-dimensional surface alterations, I compare results from the 3D model to experiments, as well as simulation results in which 3D surface alterations are ignored. Results from these simulations are presented in Chapter 3.

1.5.3 The effects of mineral heterogeneity become more pronounced as mineralogy and surface roughness become autocorrelated over similar length-scales.

Mineral heterogeneity and fracture surface roughness vary of a wide range of length-scales (Brown, 1995; Peters, 2009; Ellis and Peters, 2016). As the spatial correlation length for each distribution approach similar scales, regions of large solute fluxes may become cross-correlated with large interconnected regions of low-reactivity minerals. The prevalence of these low-reactivity paths may allow large solute fluxes to persist deep into the fracture prior to reacting with the primary mineral phases. However, the abundance of low-reactivity regions also provides a large capacity for reactive minerals to grow across the fracture plane, which would increase local reactive surface area and precipitation rates. To quantify the competition between these two mechanisms, I use the model developed in Chapter 3 to simulate precipitation in fractures that contain varied degrees of surface heterogeneity. Results from these simulations are presented in Chapter 4.

Chapter 2

Experimental investigation of the role of small-scale mineral heterogeneity on fracture sealing by mineral precipitation

2.1 Introduction

Fractures provide dominant pathways for fluid flow through low-permeability crustal rocks. However, in many subsurface environments, fluid-rock interactions lead to mineral precipitation, which can significantly reduce fracture permeability. This fracture sealing process can have the desired effect of enhancing the ability of geologic seals to isolate, for example, overpressurized CO_2 (Huerta et al., 2013; Matter et al., 2016), hydrocarbons (Boles et al., 2004), or hydrothermal fluids (Chaudhuri et al., 2012), and may be enhanced by microbial processes in efforts to isolate contaminants (Cuthbert et al., 2013; Mountassir et al., 2014). On the other hand, precipitation-induced permeability reduction within fault zones limits dissipation of increasing pore pressures, which can result in the undesired effect of more frequent seismic events (Audet and Burgmann, 2014; Yarushina and Bercovici, 2013). Quantifying the mechanisms that lead to mineral precipitation in fractures and the resulting precipitation rates is critical to predicting the response of low permeability rocks to precipitation-induced permeability changes.

Mineral precipitation in fractures occurs when: 1) local conditions (e.g., temperature or pressure) change, causing mineral solubility in resident fluids to decrease; or 2) resident fluids are displaced by a supersaturated fluid. In case 1, precipitating minerals are quickly depleted from the pore fluid limiting the extent of the reaction process (Fisher and Brantley, 1992). Here, we focus on case 2, where advection provides a continuous source of dissolved minerals, leading to significant mineral precipitation over time. Under these conditions, mineral precipitation is influenced by the relative timescales associated with surface reactions and advective transport of dissolved minerals. When the mass flux of dissolved minerals onto a fracture surface is large relative to the advective flux of dissolved minerals through the fracture, precipitation occurs predominantly near the fracture inlet. Experimental studies in idealized fractures consisting of two-dimensional, parallel-sided channels with uniformly reactive surfaces confirm this conceptual model and suggest rapid reduction in fracture permeability (Lee and Morse, 1999; Hilgers and Urai, 2002; Hilgers et al., 2003). However, real fractures exhibit both heterogeneous surface mineralogy (Landrot et al., 2012; Peters, 2009; Glassley et al., 2002) and three-dimensional surface roughness (Brown, 1995).

Mechanistic models of mineral precipitation on fracture surfaces that incorporate grain-scale heterogeneity demonstrate complex local variability in mineral precipitation rates (Lander and Laubach, 2015a; Ankit et al., 2015). These models assume that reaction kinetics are the rate-limiting process during precipitation and that the fracture-filling fluid remains uniformly supersaturated with respect to the precipitating minerals. This is a reasonable assumption in systems near equilibrium where reaction rates are very slow; however, for systems driven further from equilibrium by anthropogenic activities (fluid injection/production) or seismic events, reaction rates will be faster, leading to concentration gradients within individual fractures.

We present the first direct measurements of mineral precipitation in a variable-aperture fracture with heterogeneous surface mineralogy. Transparent fracture surfaces allowed us to use light-transmission techniques to quantify the impact of evolving transport pathways on precipitation rates over the 82-day duration of the experiment. Our results reveal that, despite early rapid precipitation near the fracture inlet, flow pathways connecting large-aperture regions persisted. These persistent flow pathways had significantly less reactive surface area, which led to a 72% reduction in the peak precipitation rate at the end of the experiment. Thus, the formation of preferential flow paths will significantly lengthen the time scale required to seal a fracture by mineral precipitation.

2.2 Overview of Experiment

We constructed a transparent variable-aperture fracture (15 x 15 cm) by mating two borosilicate glass surfaces: one rough and one smooth (for assembly details, see Arshadi et al. (2015)). To create mineral heterogeneity, we seeded the flat surface with isolated regions of $CaCO_3$ using a modified procedure developed by Nancollas and Reddy (1971). The initial $CaCO_3$ distribution was heterogeneous and isotropic (Figure 2.1a), covering 12% (27 cm^2) of the fracture surface (for details of $CaCO_3$ seeding and transmitted light measurement process, see supplementary material).

We measured the fracture aperture field both before reactive flow initiation (Figure 2.1b; $\langle b \rangle = 0.0142$ cm and $\sigma_b = 0.0042$ cm) and weekly during the reactive flow experiment to

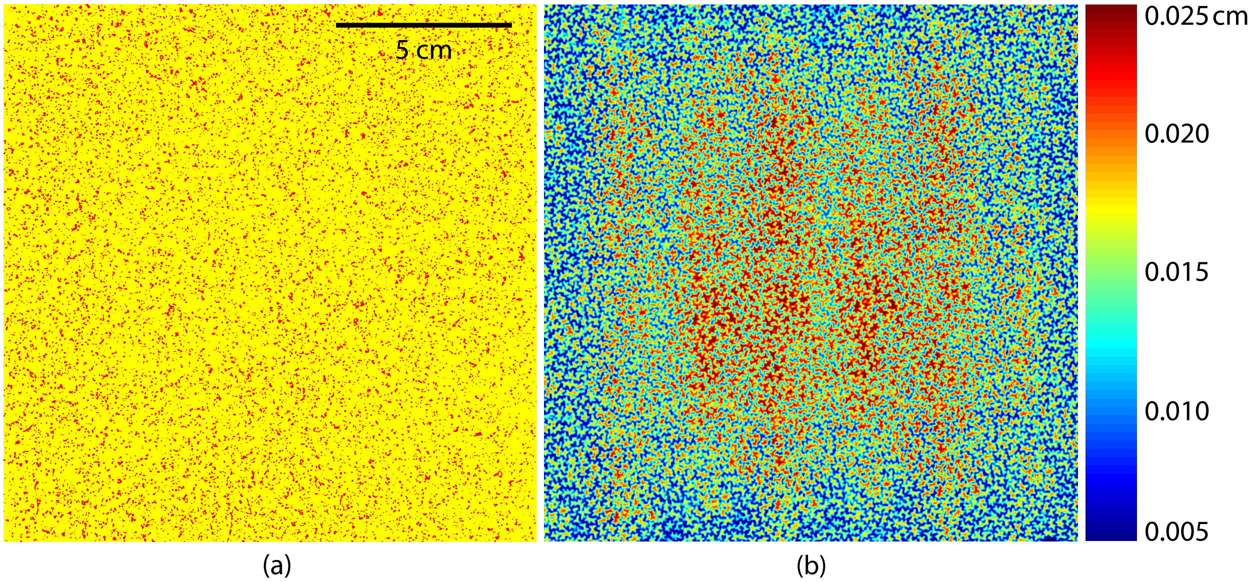

Figure 2.1: (a) $CaCO_3$ regions (red) initially cover 12% of the bottom glass surface and were uniformly distributed across the bottom fracture plate. Precipitation reactions occurred at $CaCO_3$ reaction sites (red) and not on the unaltered borosilicate glass (yellow). (b) The initial fracture aperture field with short-wavelength variability due to glass roughness and long-wavelength variability caused by small undulations of the glass surface. Reactive flow was from left to right.

directly quantify precipitation rates within the fracture. This has the advantage that precipitation rates can be determined locally throughout the fracture at high spatial resolution, unlike precipitation rates calculated from measurements of influent and effluent [Ca^{2+}], which provide only a fracture-scale measurement of precipitation rates. To measure fracture aperture, b, we filled the fracture with a non-reactive dye tracer (1/16 g/L of FD&C Blue #1, $\log(\Omega_{CaCO_3}) = 0$) and measured light absorbance, $\ln(I_{cl}/I_{dye})$, where I_{cl} and I_{dye} are measured intensities with the fracture filled with clear and dyed water (Detwiler et al., 1999). Light absorbance was directly converted to high-resolution (83 x 83 μm pixels), accurate (± 1% of the mean aperture) measurements of fracture aperture.

Because the processes controlling the initial deposition of $CaCO_3$ on the flat glass were independent of the spatial structure of the rough-walled glass, the initial random aperture and mineral-distribution fields exhibited no cross-correlation. Variograms of the initial $CaCO_3$ and aperture distributions (Figure 2.2) indicate correlation lengths of 0.015 cm and 0.05 cm, respectively. The fracture aperture and chemical heterogeneity are consistent with those measured in natural rocks (Brown, 1995; Landrot et al., 2012).

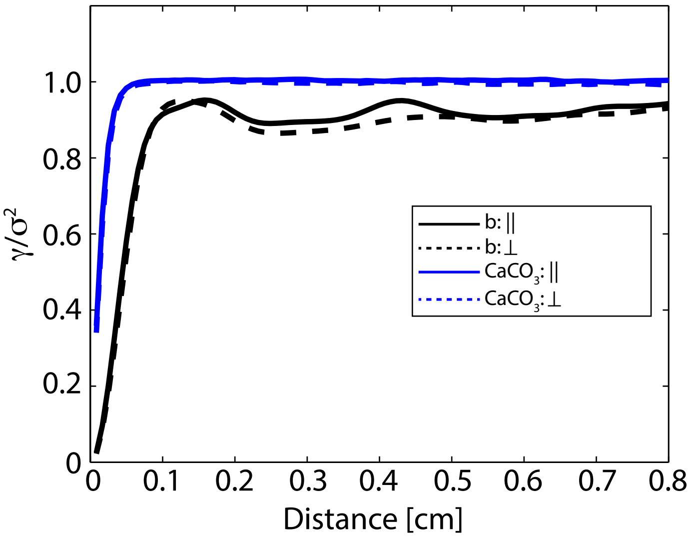

Figure 2.2: Normalized semi-variograms (γ/σ^2, where σ^2 is variance) for the $CaCO_3$ and aperture distributions measured parallel ($\|$) and perpendicular ($\perp$) to the flow direction. Small-scale aperture variability and mineral heterogeneity are both isotropic with correlation lengths of 0.05 and 0.015 cm, respectively.

During the reactive flow experiment, continuous-flow syringe pumps (Teledyne ISCO, MODEL 500D) injected a well-mixed $CaCl_2$–$NaHCO_3$ solution, $log(\Omega_{CaCO_3}) = 1.44 \pm 0.1$, into the fracture at 0.5 ml/min. We paused reactive flow during weekly aperture measurements and imaged the fracture while filling it with the nonreactive dye. We used the corresponding light absorbance measurements to calculate evolving dye concentration fields (C/C_o, where C_o is the injected dye concentration) within the fracture (Detwiler et al., 2000). These dye concentration measurements highlight fracture-scale changes in the flow field caused by $CaCO_3$ precipitation.

2.3 Results

Figure 2.3 shows the normalized dye concentration fields (C/C_o) measured at 0.3 injected pore volumes at $t = 0$ and $t = 82$ days (Figure 2.3a), where t is the time from the onset of reactive flow. At t=0, the C/C_o field shows that initial aperture variability enhanced spreading in the mean flow direction (left to right). At the leading edge of the injected dye front, thin tendrils with elevated C/C_o indicate the presence of weak preferential flow paths. Variability in the mean velocity caused some long-wavelength variations in C/C_o. However, due to mixing between fast and slow flow paths, C/C_o quickly approached 1 across the flow field. At $t = 82$ days, the C/C_o field changed significantly. Local precipitation-induced aperture reduction caused thin channels, in which $C/C_o \sim 1$, to extend far into the fracture and created low flow regions adjacent to the dominant flow paths ($C/C_o << 1$). At about 6 cm from the inlet, channels of high C/C_o began to spread laterally and decrease in magnitude, indicating the absence of newly precipitated minerals and delineating the extent of the reaction zone.

Precipitation-induced flow alterations caused a marked reduction in mineral precipitation rate. To quantify precipitation rate, $R = -\dfrac{db}{dt}$ ($\frac{\mathrm{cm}}{\mathrm{s}}$), we subtracted sequential aperture field measurements and divided them by the time interval between the two measurements. To minimize the effects of long wavelength variations in the initial velocity field, we segmented the R measurements into three streamtubes, each with different mean velocities (see supplementary material for streamtube details). Within each streamtube, we averaged R perpendicular to the mean flow direction to yield one-dimensional $\bar{R}$ profiles in the flow direction. Figure 2.3b plots $\bar{R}$ along the middle streamtube at early and late time. At early time, $\bar{R}$ was largest at the fracture inlet and decreased monotonically in the mean flow direction. After 82 days of $CaCl_2$-$NaHCO_3$ injection, $\bar{R}$ decreased significantly. Preferential flow channeling caused a 72% reduction of the precipitation rate at the fracture inlet, from 7.1 to $1.9 \cdot 10^{-10}$ $\frac{\mathrm{cm}}{\mathrm{s}}$. Further from the inlet, the preferential flow paths increased in width and

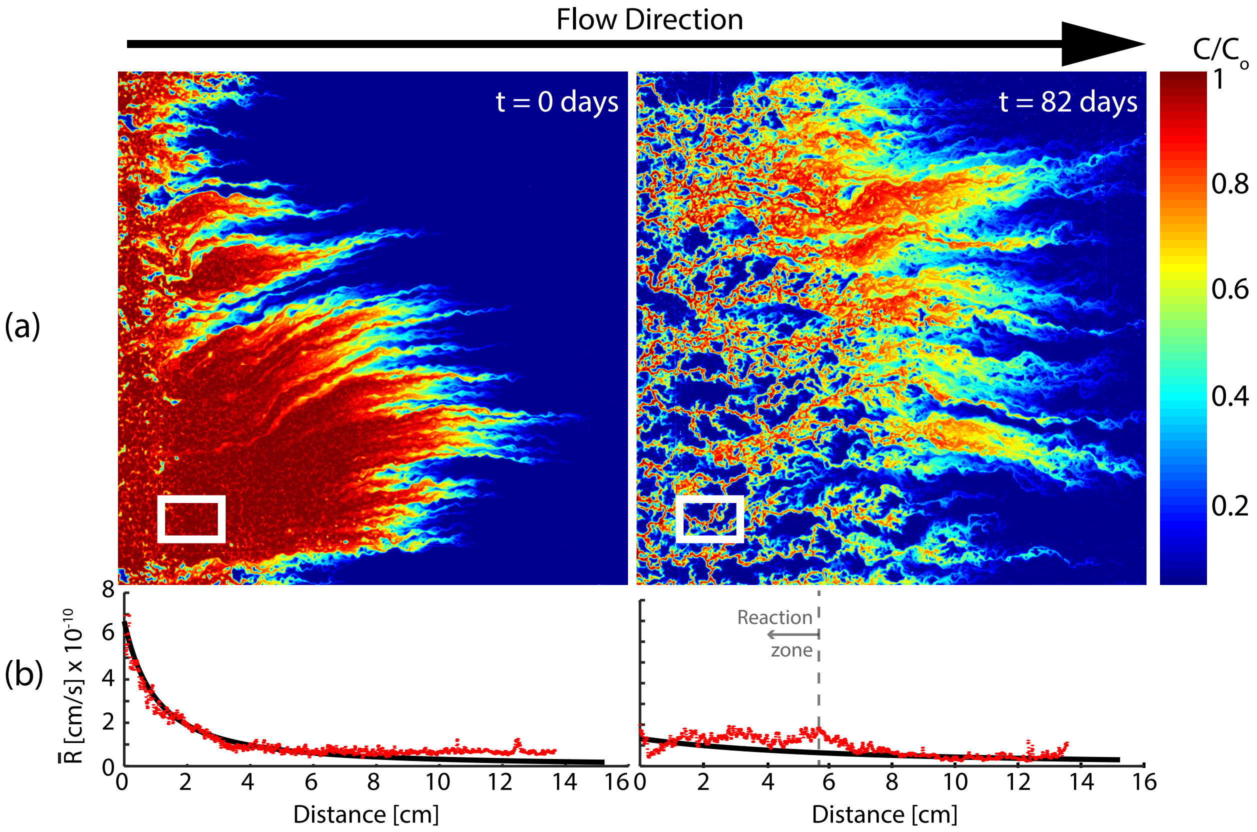

Figure 2.3: Normalized concentration measurements (C/C_o) during nonreactive tracer injection ($\log(\Omega_{CaCO_3})$=0) demonstrate how mineral precipitation altered flow. These C/C_o fields are frames taken from animations of the dye injection (Movie S1 and S2) after 0.3 injected pore volumes. C/C_o at $t = 0$ shows that initial aperture heterogeneity induced velocity variations across the flow field that were quickly dampened by mixing between fast and slow flow paths. At $t = 82$ days, mineral precipitation created thin preferential paths and low flow regions where the flux of dissolved species decreased. The small boxed region indicates a portion of the fracture that is analyzed at the local scale and discussed in detail in Figure 2.4. The bottom frames show the width-averaged precipitation rates ($\bar{R}$, $\frac{\text{cm}}{s}$) in the mean flow direction at $t = 0$ and 82 days. The red data points are measured $\bar{R}$ and the black curves are best-fit solutions to the steady-state 1D advection reaction equation. Precipitation-rate profiles demonstrate that flow channeling caused $\bar{R}$ to decrease by 72% at the fracture inlet.

became more interconnected, exposing a larger portion of the flow field to reactive fluid. This caused $\bar{R}$ to slightly increase near the inlet and remain relatively constant within the reaction zone (∼6 cm from the inlet). Beyond 6 cm, the lateral spreading of fluid induced precipitation across the flow field and a steady-decline in the width-averaged precipitation rate.

To better understand the effects of local heterogeneity on mineral precipitation, we modeled the observed precipitation rates using the steady-state 1D advection-reaction equation:

$$\frac{dc}{dx} = -\frac{k \cdot A_R}{v \cdot b}(\Omega_{CaCO_3} - 1)^3 \tag{2.1}$$

where k is the reaction rate constant ($\frac{\text{mol}}{\text{cm}^2 \cdot \text{s}}$), A_R is the reactive surface area per unit area of fracture surface ($\frac{\text{cm}^2}{\text{cm}^2}$), v is the mean velocity within the streamtube ($\frac{\text{cm}}{\text{s}}$), and b is the mean aperture (cm). Tang et al. (2008) observed similar third-order kinetics during their CaCO_3 precipitation experiments, and the higher-order kinetics are indicative of mineral growth at both screw and edge dislocations on the mineral surface (Blum and Lasaga, 1987). Our light transmission approach provides measurement of A_P, the projected area of CaCO_3 regions, which is likely proportional to A_R, but not a direct measure of A_R. Therefore, we fit modeled values of $\bar{R} = \frac{M_{CaCO_3}}{\rho_{CaCO_3}} \cdot k \cdot A_R(\Omega_{CaCO_3} - 1)^3$, where M_{CaCO_3} is the molar mass of CaCO_3 ($\frac{\text{g}}{\text{mol}}$), and ρ_{CaCO_3} is the density of calcite ($\frac{\text{g}}{\text{cm}^2}$), to measurements of $\bar{R}$ by adjusting $k \cdot A_R$ to minimize the sum of squared residuals between the observed and modeled values within the reaction zone.

At early time, the one-dimensional model agrees very well with the measured precipitation rates along the length of the fracture using a value of $k \cdot A_R = 10^{-14.46} \frac{\text{mol}}{\text{cm}^2 \cdot \text{s}}$ (Figure 2.3b). The agreement between predicted and measured $\bar{R}$ demonstrates that despite local aperture and mineral heterogeneity, a simple 1D model, that uses average aperture, reactive surface area, and velocity, effectively predicts mineral precipitation rates. This suggests that as precipitation increases A_R, local rates will increase, leading to rapid fracture sealing. However, the precipitation rates measured at late time in our experiment demonstrate the opposite.

The best fit between $\bar{R}$ derived from (2.1) and the measured precipitation rates at late time requires a 70% reduction in $k \cdot A_R$. In addition, because $\bar{R}$ no longer decreases monotonically along the length of the fracture, the solution to equation (2.1) deviates significantly from the relatively constant precipitation rates observed within the reaction zone. The largest difference between observed and predicted $\bar{R}$ occurs approximately 6 cm from the inlet, where (2.1) underestimates $\bar{R}$ by 65%. Beyond the reaction zone, the model predicts the precipitation rates quite well.

The discrepancy between observed and predicted precipitation rate at late time suggests that a single, volume-averaged value of $k \cdot A_R$ became less representative of the local precipitation kinetics as preferential flow paths developed. To better understand the mechanisms responsible for the deviation from modeled behavior, we explored the evolution of a local region (white box in Figure 2.3a) over the duration of the precipitation experiment. Figure 2.4 shows a series of measurements from this region at t=17, 38 and 82 days, with C/C_o in the top row, b/b_o in the middle row, and the projected $CaCO_3$ distribution (yellow) superimposed on a binarized representation of the developing preferential flow paths (red) in the bottom row. The C/C_o measurements show flow focused into thin preferential paths that extended progressively farther into the fracture over time. In the middle row, b/b_o values less than 1 show locations where mineral precipitation caused aperture to decrease. Aperture reduction is largest directly adjacent to the preferential flow paths, where dissolved mineral fluxes are highest, and smallest in slow-flow regions that are far from the primary flow paths. In the bottom row, we identified preferential flow paths as regions where $C/C_o > 0.5$ after 0.3 pore volumes of nonreactive tracer injection. These binarized fields show that flow became progressively more focused between regions of precipitated $CaCO_3$. This flow-focusing process limited exposure of the reactive fluid to a small subset of regions of precipitated $CaCO_3$, which explains the significant drop in measured precipitation rate observed within the first 6 cm of the fracture at later time (Figure 2.3b).

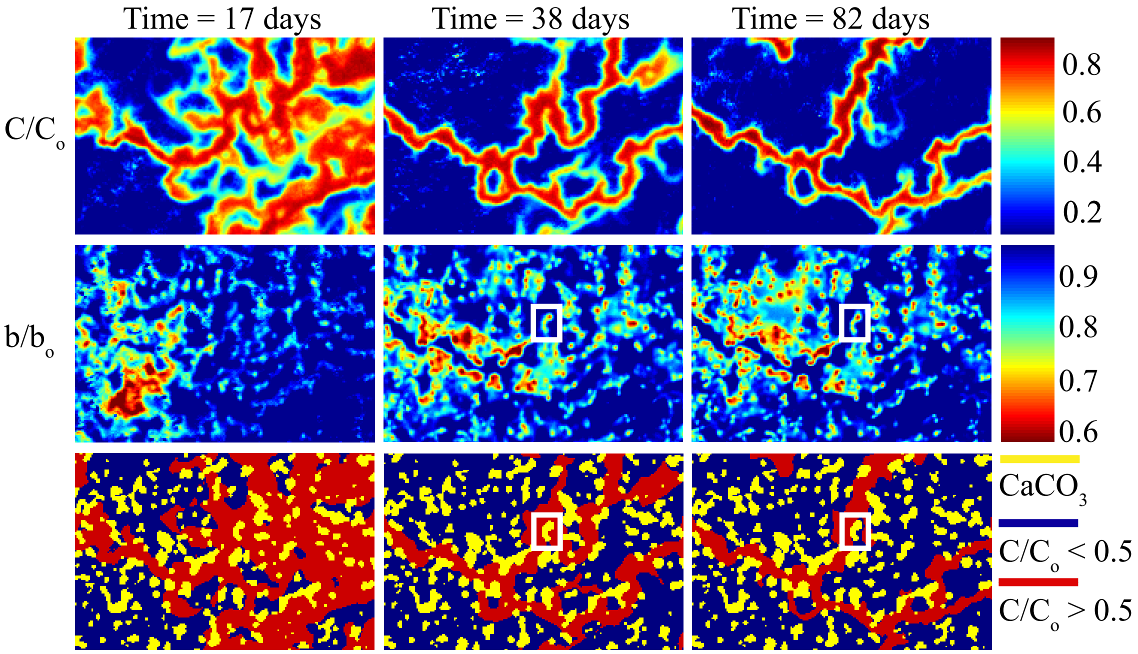

Figure 2.4: Measured flow paths (C/C_o), normalized aperture (b/b_o), and $CaCO_3$ distribution at t = 17, 38, and 82 days show how the feedback between precipitation and local aperture promotes preferential flow and reduces fracture-scale precipitation rates. The C/C_o measurements show preferential paths extending deeper into the fracture over time and changing orientation after the initial channel development. The b/b_o measurements demonstrate that preferential flow is driven by local precipitation-induced aperture reduction; small b/b_o values that border primary flow paths decrease transport into regions with small C/C_o values. The mineral distribution measurements show that flow becomes increasingly focused into regions with limited $CaCO_3$, which causes a sharp reduction in width-averaged precipitation rate within the reaction zone. Note, at t = 17 days, we did not inject enough dye to ensure that $C = 1/16$ g/L across the fracture, and as a result, underestimated local fracture aperture in the lower left corner of the region. The large region of small b/b_o disappears between t = 17 and 38 days because we increased the dye injection time scale and allowed C/C_o to reach 1 across the flow field prior to measuring aperture; the absence of the red region at t = 17 and 38 days is an artifact of the measurement process and does not indicate dissolution or mobilization of $CaCO_3$ during the experiment.

Local precipitation-induced aperture reduction promoted the development of preferential flow. At t = 17 days, Figure 2.4 shows smallest b/b_o (largest reductions) near the fracture inlet and a thin flow-path with large C/C_o in the zone of altered aperture. The relatively unaltered aperture on the right side of the domain allowed the tracer to spread, and the onset of this lateral spreading delineates the edge of the reaction zone. The gradual propagation of a clearly delineated reaction zone indicates that precipitation kinetics are sufficiently fast that excess Ca^{2+} is consumed within the fracture (i.e., precipitation is limited by transport of Ca^{2+} ions, not reaction kinetics). Within the reaction zone, at $t = 38$ days, areas of small b/b_o near the inlet focused flow into a thin preferential path, and at the center of the region, this primary flow path branched into two flow paths due to the small cluster in the middle of the region where $b/b_o \sim 0.6$.

As the preferential flow paths developed, precipitation at heterogeneous $CaCO_3$ reaction sites diverted flow into regions of lower reactivity. At $t = 38$ days, the mineral distribution measurement shows that flow was focused directly over the boxed $CaCO_3$ region and then diverted around the reaction site at $t = 82$ days. A pixel-to-pixel comparison of b/b_o at the boxed $CaCO_3$ site shows that mineral precipitation reduced the local aperture by approximately 10%, which caused the observed changes between intermediate and late time. At $t = 38$ and 82 days, the mineral distribution measurements show similar primary flow paths at the inlet and bottom portion of the region, which demonstrates that flow within the reaction zone focused the largest flux of dissolved ions into pathways with limited $CaCO_3$ and suggests that precipitation reactions in low-flow regions decrease throughout the experiment.

The local transport changes highlighted in Figure 2.4 altered fracture-scale precipitation rates. We used the binary preferential channel measurements as a mask to quantify aperture and mineral properties within the reaction zone that control flow and reactions. Figure 2.5 shows the aperture distribution within and outside of the preferential flow paths (PFPs) at $t = 82$ days. The aperture distribution within the PFPs is skewed to the right and the large peak at ~0.016 cm indicates that mineral precipitation focused flow into large apertures.

Flow focusing into large apertures was driven by mineral growth within the reaction zone. At the fracture inlet, $CaCO_3$ precipitation increased A_P from 13% to 22%. Despite the increase in surface coverage at this location, the width-averaged precipitation rate decreased by 72%. At $t = 82$ days, the mineral distribution shows that $CaCO_3$ only occupied 4% of the area within primary flow paths – an effective 70% reduction in $CaCO_3$ availability in flow paths that contain the largest flux of dissolved ions. The strong correlation between precipitation-rate reduction and an effective reduction in $CaCO_3$ availability supports the conclusion that fracture-scale precipitation rates decreased because mineral precipitation led to a decrease in dissolved ion transport into low permeability regions that contain a larger percentage of the $CaCO_3$ regions.

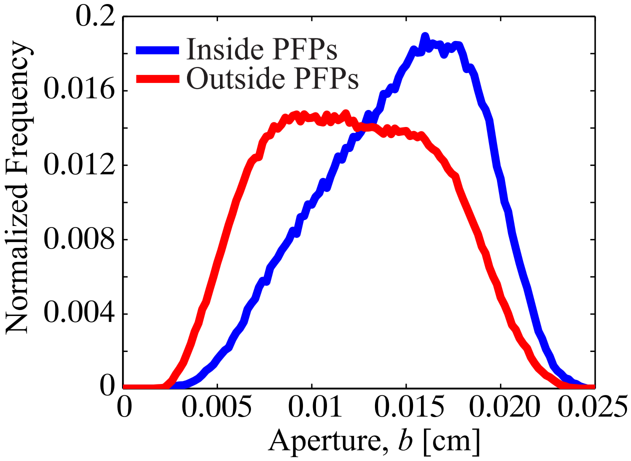

Figure 2.5: Histograms of the aperture distribution within, and outside, preferential flow paths (PFPs) in the first 6 cm of the fracture at $t = 82$ days. The long-tail in the aperture distribution within PFPs indicates that mineral precipitation focused flow into large-aperture pathways.

2.4 Discussion and Concluding Remarks

We have presented the first direct observations of mineral-precipitation-induced flow alteration in a 3D variable-aperture fracture with mineral heterogeneity. During the 82-day experiment, small-scale mineral heterogeneities led to regions of localized aperture reduction within the reaction zone and focused flow into thin preferential flow channels. Only 4% of the fracture surface along preferential flow paths was occupied by reactive $CaCO_3$ compared to 19% of the entire fracture surface. This resulted in a 72% reduction in width-averaged precipitation rate within the reaction zone.

Previous theoretical and numerical analyses of reactive transport in heterogeneous porous media (e.g., Seeboonruang and Ginn, 2006) suggest that precipitation is not sensitive to small-scale mineral heterogeneity (i.e, when the characteristic length-scale of mineral heterogeneity is smaller than the permeability-field correlation length). Thus, in a variable-aperture fracture, we would expect precipitation rates to be controlled by local aperture. Further, the results from these studies suggest that if the characteristic length scale of aperture variability is much smaller than the fracture, it may be reasonable to model the reactive transport using a simple 1D model.

At early time, the excellent agreement between our experimental results and the 1D advection-reaction model using fracture-scale measures of the relevant model inputs supports these expectations. However, the discrepancy between our predictions and observations at later time highlight the significant shortcomings of using a volume-averaged 1D model. Our results demonstrate that this simple conceptual model breaks down because the feedback between precipitation and local aperture focuses flow into low reactivity pathways. As flow is increasingly focused into regions with lower mineral abundance, fracture-scale reactivity becomes strongly dependent on local mineral and aperture properties that control the distribution of flow and dissolved mineral transport.

The results from our experiment demonstrate that mineral precipitation predictions can be easily misinformed by studies that either disregard mineral heterogeneity or examine the precipitation process over short time scales, and thus disregard the feedback between precipitation and aperture. If we assume uniform surface mineralogy within our fracture (e.g., Hilgers et al., 2003; Cuthbert et al., 2013) and model the precipitation process using the rate constant, k, derived from our early time measurements, we predict complete sealing of the largest apertures (0.028 cm) in approximately 2 months. Including the effect of the initial mineral heterogeneity increases this estimate to 16 months. These two fracture-sealing estimates might be considered conservative because mineral precipitation is expected to increase reactive surface area (Emmanuel and Berkowitz, 2005; Noiriel et al., 2012) and further precipitation-rate enhancement. However, using our late-time measured precipitation rates results in a timescale to fracture sealing of approximately 20 years. Further, we expect that this prediction underestimates the sealing timescale due to the continued diversion of flow into preferential paths with fewer $CaCO_3$ regions, resulting in further decreases in precipitation rates in the lengthening reaction zone.

Chapter 3

Model development: Using the level set method to quantify the role of mineral heterogeneity on transport properties

3.1 Introduction

Fractures provide dominant pathways for fluid flow in low-permeability rocks, which exist throughout the Earth's crust from near-surface bedrock outcrops to deep formations important to energy production and waste storage. The introduction of exogenous fluids that are in chemical disequilibrium with the host rock can lead to fluid-rock reactions that induce mineral precipitation and/or dissolution, altering the transmissivity of fractures. Such geochemically induced transmissivity alterations may seal leakage pathways in caprocks and limit the migration of sequestered CO_2 (Elkhoury et al., 2015), or may lead to development of localized regions of fast flow that enhance contaminant transport (Kang et al., 2003; Mountassir et al., 2014). Thus, predicting the the long-term evolution of fractures exposed to geochemical disequilibrium is important to a range of both engineered and natural environments.

During flow through fractures, reaction kinetics at the fracture surfaces and the transport of dissolved ions by advection and diffusion control reaction rates. Recent experimental and computational studies have led to significant insights into the importance of these mechanisms, particularly for rough-walled fractures with monomineralic surfaces. The relative timescales associated with each mechanism strongly influence the characteristics of the resulting reactions (e.g., Detwiler et al., 2003; Battiato and Tartakovsky, 2011; Osselin et al., 2016). Slow reaction kinetics (relative to rates of ion transport) lead to relatively uniform dissolved ion concentrations, and thus, uniform reaction rates throughout the fracture. However, when reaction kinetics are fast relative to ion transport, reactions deplete dissolved ions faster than they can be replenished, leading to the development of concentrations gradients throughout the fracture (Steefel and Lichtner, 1998).

Because local dissolution and precipitation reactions induce changes in surface topography (and fracture aperture), transport-limited conditions lead to feedbacks between reactions and transmissivity that alter reactive transport processes over time. In fractures with a uniform surface mineralogy, reactions causing fracture-surface dissolution result in a positive feedback and the formation of dissolution channels, or wormholes, that enhance transport variations across the fracture (Noiriel et al., 2013; Smith et al., 2013; Dávila et al., 2016). Conversely, reactions resulting in mineral precipitation lead to a negative feedback, such that the most rapid reduction in local transmissivity occurs along preferential flow paths; this results in decreased prevalence of preferential flow and the eventual closure of the fracture (Chaudhuri et al., 2008, 2012).

Real fracture surfaces typically exhibit some degree of mineral heterogeneity in addition to the aperture variability that induces preferential flow (Glassley et al., 2002; Marques et al., 2017). Mineral heterogeneity leads to additional perturbations of local reaction rates that have the potential to disrupt the feedback mechanisms observed in mineralogically homogeneous fractures. For dissolution reactions, preferential dissolution of more soluble minerals can lead to notably different behaviors depending on the characteristics of the mineral heterogeneity. For example, Garcia-Rios et al. (2017) showed that the presence of small-scale mineral heterogeneities increased the reaction potential of a sandstone core by limiting the development of wormholes. Similarly, when reactions lead to mineral precipitation, mineral heterogeneity can lead to variations in local reaction rates that enhance preferential flow (Mountassir et al., 2014; Jones and Detwiler, 2016), which does not occur in fractures with uniform surface mineralogy (Lee and Morse, 1999; Hilgers and Urai, 2002; Hilgers et al., 2003).

Efforts to predict the evolution of fracture transport properties resulting from reactive surface alteration employ different approaches for simulating reactive transport. Direct solution of the Navier-Stokes equations with boundary conditions defined along the fracture surfaces and fracture boundaries can provide a rigorous solution of the three-dimensional velocity field (e.g., Boutt et al., 2006; Lee et al., 2015). Using this velocity field, the three-dimensional advection-diffusion-reaction equation can be solved within the fracture leading to quantifiable dissolution or precipitation rates on the fracture surfaces (Szymczak and Ladd, 2009). This approach is computationally intensive; the need to discretize the domain across the fracture aperture, which is often O(100 μm) leads to very high-resolution computational grids. A more computationally efficient alternative is to depth-average the flow and transport equations across the fracture aperture. This results in two-dimensional equations that provide a reasonable representation of flow and reactive transport through variable aperture fractures (e.g., Detwiler and Rajaram, 2007; Szymczak and Ladd, 2011).

Different methods have been used to quantify the fracture-surface alterations that result from local dissolution/precipitation reactions. For uniform surface mineralogy, it is relatively straightforward to convert local reaction rates into changes in fracture aperture by applying a 1D alteration of the local domain (e.g., Cheung and Rajaram, 2002; Andre and Rajaram, 2005). However, when surface roughness increases, it is necessary to develop more rigorous approaches for tracking the fracture surface (Yu and Ladd, 2010; Starchenko et al., 2016) and account for evolving reactive surface area (Molins, 2015).

When fracture surfaces contain mineral heterogeneities, it becomes increasingly important to represent both the local reactive surface area and alteration in the direction normal to the surfaces. Because mineral reactions occur fastest along fluid-rock boundaries with the largest reactive surface area (Weeks and Gilmer, 2007), fluid-rock reactions can lead to heterogeneous surface alterations that are not captured using a 1D alteration approach. This is particularly important during mineral precipitation, where mineral deposition can lead to non-uniformly distributed, and arbitrarily oriented, cements that extend across the fracture aperture (Tokan-Lawal et al., 2015; Ankit et al., 2015; Kling et al., 2017). Recent numerical studies have employed different immersed boundary methods, such as the level set method, to represent surface alterations in the direction normal to the fracture surface (e.g., Yu and Ladd, 2010; Li et al., 2010; Soulaine et al., 2017). However, the simple geometry/mineralogy of the fractures examined in these studies limits our understanding of how mineral precipitation affects the transport properties of a heterogeneous fracture.

In this paper, we explore the impact of 3D mineral growth dynamics on precipitation-induced transmissivity alteration in a heterogeneous fracture. To do this, we simulate dissolved ion transport using a reactive transport model and model the precipitation process using: (1) a 1D vertical growth surface alteration method (e.g., Hanna and Rajaram, 1998; Detwiler and Rajaram, 2007; Szymczak and Ladd, 2012), and (2) a 3D level set surface alteration method. To better understand the effects of three-dimensional growth on reactive transport, we provide a qualitative comparison between the results from (1) and (2) to recent experiments of precipitation in a heterogeneous fracture (Jones and Detwiler, 2016). In addition, we quantify the influence of different transport conditions on the evolution of reactive transport in heterogeneous fractures and demonstrate the inherent scale dependence of the mineral precipitation process.

3.2 Model Development

We first discuss generalized flow and reactive transport equations (Section 4.2.1), then describe two different approaches for representing (Section 3.2.2) and advancing (Section 3.2.3) the fracture surfaces. Finally, we present simplified versions of these generalized equations for the case of a single reacting species using depth-averaged flow and transport (Section 3.2.4) and a description of the computational algorithm used to implement these models (Section 3.2.4).

3.2.1 Multi-species reactive transport equations

The Stokes equation and advection-diffusion-reaction equation describe flow and transport of dissolved ions through the three-dimensional void space between fracture surfaces. The general 3D formulation of the Stokes equation yields:

$$\nabla P = \mu \nabla \cdot (\nabla \vec{v}) \tag{3.1}$$

$$\nabla \cdot \vec{v} = 0 \tag{3.2}$$

where P is the local pressure, μ is the viscosity, and $\vec{v}$ is the velocity. Applying no-slip ($\vec{v} = 0$) and no-flux ($\nabla P = 0$) boundary conditions on the fracture surfaces and prescribed pressure conditions at the fracture inlet and outlet leads to solution of the 3D velocity and pressure distributions within the fracture (Brush and Thomson, 2003).

For the general case of multiple dissolved species, an advection-diffusion-reaction equation represents the influence of advection and diffusion on the concentrations of each species, i:

$$\frac{\partial c_i}{\partial t} + \nabla \cdot (v c_i) - \nabla \cdot (D_i \nabla c_i) = 0 \tag{3.3}$$

where c_i is the concentration of species i, D_i is the molecular diffusion coefficient, and the boundary condition on the fracture surfaces describe the resulting heterogeneous reactions:

$$D_i \nabla c_i \cdot \vec{n} = R_i^{min} \tag{3.4}$$

where R_i^{min} is the reaction rate and $\vec{n}$ is the outward unit-normal vector at the fracture surfaces. For the case of precipitation, R_i^{min} quantifies the flux of species i from solution onto the fracture surfaces caused by all precipitation reactions, such that:

$$R_i^{min} = \sum_{m=1}^{N_m} \alpha_{im} r_m \tag{3.5}$$

where N_m is the total number of precipitating minerals and α_{im} is the number of moles of species i in mineral m. r_m is the precipitation rate of mineral m:

$$r_m = k_m \left(1 - \left[\frac{IAP}{K_{sp}}\right]\right)^n \tag{3.6}$$

where k_m is the reaction rate constant describing the precipitation rate far from equilibrium, IAP is the ion activity product, K_{sp} is the solubility product for mineral m, and n is an empirically derived constant that accommodates nonlinear reaction processes (Steefel et al., 2015).

Under typical reactive transport conditions, the solubility concentration of dissolved minerals is much smaller than their corresponding solid-phase density (Ortoleva et al., 1987; Lichtner, 1988) such that changes in the dissolved ion concentrations occur much more quickly than changes to the flow geometry. Thus, for constant boundary conditions, it is reasonable to use quasi-steady solutions to the flow and reactive transport equations (Lichtner, 1988; Hanna and Rajaram, 1998; Szymczak and Ladd, 2009) such that in (3.3) $\frac{\partial c_i}{\partial t} \backsimeq 0$. Furthermore, it is common to assume that homogeneous reactions can be represented as equilibrium reactions such that (3.3) can be solved for a subset of primary species; secondary species concentrations can then be determined directly from the primary species concentrations and the stoichiometry of the associated reactions (Lichtner, 1985).

3.2.2 Fracture surface geometry and reactive surface area

Defining the flow and transport boundary conditions requires explicit representation of the fracture surface geometry and mineralogy. Figure 3.1 shows a schematic representation of a rough-walled fracture with heterogeneous surface mineralogy. This simplified case includes reactive regions (white) and non-reactive regions (grey), but the general approach we present here can be applied to any number of distinct surface minerals.

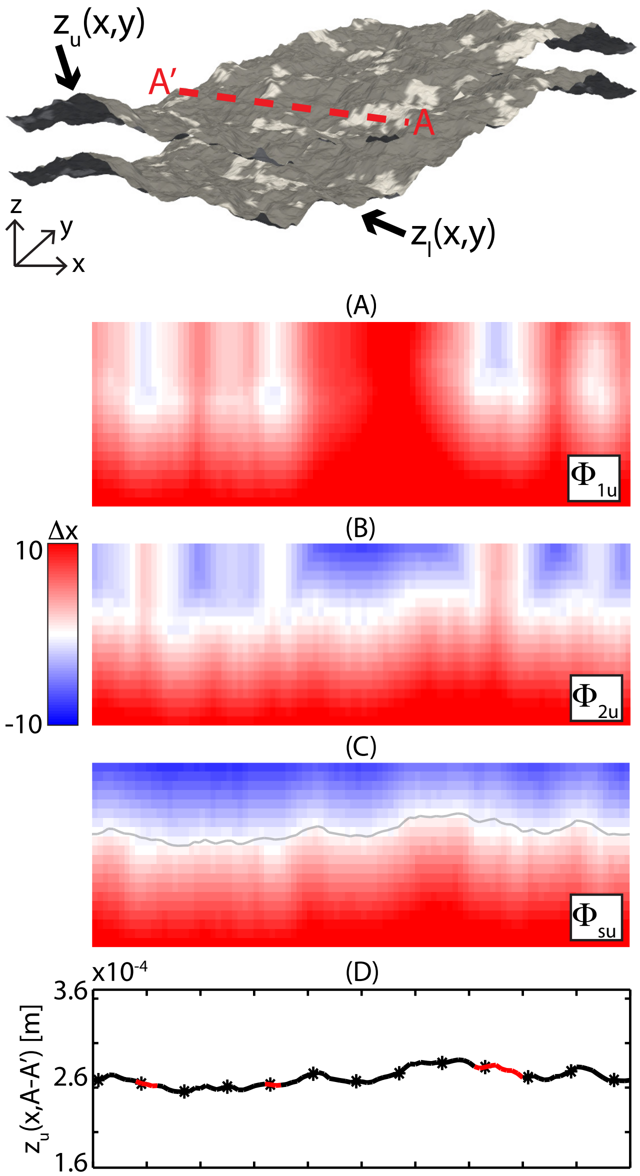

Figure 3.1: (Top) Schematic of a three-dimensional fracture that contains both surface roughness and mineral heterogeneity. Fast reacting minerals (white, m_1) and slowly reacting minerals (grey, m_2) are randomly distributed on the surfaces. The surfaces are represented using two level set functions ($\phi_{1u}(\vec{x})$ and $\phi_{2u}(\vec{x})$) that store the interface locations for (A) m_1 and (B) m_2. The three-dimensional fracture surface is reconstructed by combining $\phi_{1u}(\vec{x})$ and $\phi_{2u}(\vec{x})$ to generate (C) $\phi_{su}(\vec{x})$. The original surface on A-A' is represented with the grey line. (D) To convert $\phi_{su}(\vec{x})$ to a 2D array of surface elevations, we integrate (3.10) across the $\phi(\vec{x})$ domain. m_1 in the 1D surface elevation profile, $z_u(x, A\text{-}A')$, shown in the bottom frame is in red, and m_2 is shown in black.

To represent the fracture surfaces in a computational mesh, we define a cartesian coordinate system in which the x-y plane is oriented parallel to the mean fracture plane. The upper and lower fracture surfaces are then completely defined by their elevations, $z_u(x, y)$ and $z_l(x, y)$, respectively. Figure 3.1 shows the elevation of the upper fracture surface, $z_u(x, y)$, along cross-section, A-A'. Heterogeneous surface mineralogy can be represented by $k_s(x, y)$.

The level-set method is an alternative approach to representing the fracture surfaces wherein each fracture surface is defined as the zero-level-set of a 3D function:

$$\phi_s(\vec{x}) = \begin{cases} -d & \vec{x} \in \Omega^- \\ 0 & \vec{x} \in \Gamma \\ +d & \vec{x} \in \Omega^+ \end{cases} \tag{3.7}$$

where d is the minimum Euclidian distance to the interface at any $\vec{x}$, Γ represents the fracture surface and Ω^- and Ω^+ are the regions of the domain in the rock matrix and fluid, respectively. The distinct advantage of the level-set method is that it provides a means for defining and advancing the fracture surfaces that naturally accounts for both curvature of the surface and variable rates across each fracture surface (see details in Section 3.2.3). To define the surfaces using the level-set method, we initialize $\phi_s(\vec{x})$ on a 3D mesh with grid spacing Δx=Δy=Δz that encompasses the fracture and a portion of the bounding rock matrix. However, to represent different minerals that can advance at different rates and, thus, evolve to cover adjacent minerals, it is necessary to define a unique distance function, $\phi_m(\vec{x})$, for each mineral, m, of the total, N, minerals exposed on the fracture surface.

Figure 3.1A plots the distance function along cross-section A-A' for the white regions (i=1) on the upper surface in Figure 3.1. Red regions ($\phi_1(\vec{x}) > 0$) are located within the fracture, blue regions ($\phi_1(\vec{x}) < 0$) are located within the rock matrix, and white regions ($\phi_1(\vec{x}) = 0$) represent patches of mineral 1 on the upper fracture surface. Lightly colored regions (i.e., $\phi_1(\vec{x}) \sim 0$) interspersed throughout the cross-section that do not border regions of $\phi_1(\vec{x}) < 0$ indicate the presence of out-of-plane reaction sites whose interface is near the A-A' cross-section. For this example, combining a similar distance function (Figure 3.1B) for the grey regions (i=2), $\phi_2(\vec{x})$, and finding the local minimum of $\phi_1(\vec{x})$ and $\phi_2(\vec{x})$ leads to $\phi_s(\vec{x})$ for the surface. For the general case of a surface comprised of N minerals, the distance function defining the fracture surface is:

$$\phi_s(\vec{x}) = \min(\phi_m(\vec{x})\Big|_{m=1}^{N}) \tag{3.8}$$

The level-set method requires determining the elevations of the fracture surfaces in order to construct a corresponding computational mesh for flow and reactive transport simulations. We quantify surface elevations of each surface by calculating the solid volume associated with the upper and lower rock matrix. For one surface, we segregate the regions of the domain occupied by the rock matrix (Ω^-) and fluid-filled fracture (Ω^+) using a smoothed Heaviside function:

$$H(\phi_s(\vec{x})) = \begin{cases} 0 & \phi_s(\vec{x}) > \epsilon \\ \frac{1}{2} + \frac{\phi_s(\vec{x})}{2\epsilon} + \frac{1}{2\pi} sin(\frac{\pi\phi_s(\vec{x})}{\epsilon}) & |\phi_s(\vec{x})| < \epsilon \\ 1 & \phi_s(\vec{x}) < -\epsilon \end{cases} \tag{3.9}$$

where ϵ is 1.5Δx (Osher and Fedkiw, 2003). The total solid volume associated with one of the fracture surfaces is then given by the volume integral of $H(\phi(\vec{x}))$:

$$V(\vec{x})_{\Omega^-} = \int_\Omega H(\phi_s(\vec{x}))d\vec{x} \tag{3.10}$$

and the elevation of each surface can be determined at any location as:

$$\begin{aligned} z_u(x,y) = z_{max} - &\frac{1}{\Delta x \Delta y}\int_0^{z_{max}}\int_{y-\frac{\Delta y}{2}}^{y+\frac{\Delta y}{2}}\int_{x-\frac{\Delta x}{2}}^{x+\frac{\Delta x}{2}} H(\phi_{s_u}(\vec{x}))\,dx\,dy\,dz \\ z_l(x,y) = &\frac{1}{\Delta x \Delta y}\int_0^{z_{max}}\int_{y-\frac{\Delta y}{2}}^{y+\frac{\Delta y}{2}}\int_{x-\frac{\Delta x}{2}}^{x+\frac{\Delta x}{2}} H(\phi_{s_l}(\vec{x}))\,dx\,dy\,dz \end{aligned} \tag{3.11}$$

where z_{max} is the z-direction extent of the computational domain. Equation 3.11 provides elevations of the upper and lower fracture surface over the entire domain, which can then be used to construct (or deform) the corresponding computational mesh.

The local surface area of the zero-level-set can also be directly calculated for each surface by computing the surface integral of the corresponding distance function, $\phi_s(\vec{x})$:

$$A_s(x,y) = \int_0^{z_{max}} \int_{y-\frac{\Delta y}{2}}^{y+\frac{\Delta y}{2}} \int_{x-\frac{\Delta x}{2}}^{x+\frac{\Delta x}{2}} \delta(\phi_s(\vec{x}))|\nabla\phi_s(\vec{x})| \, dx \, dy \, dz \tag{3.12}$$

where the Dirac delta function, $\delta(\phi_s(\vec{x}))$, in equation (3.12) is given by the derivative of the smoothed Heaviside function presented in equation (3.9).

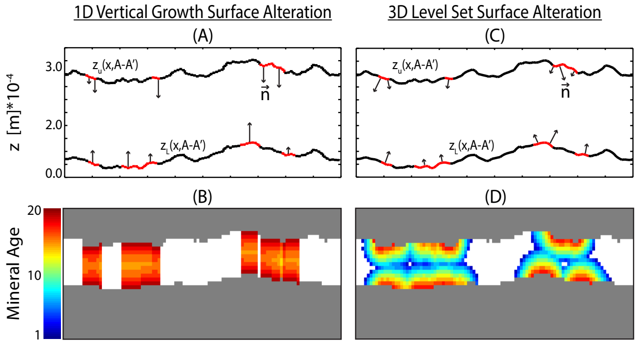

Figure 3.2: Surface elevations for A-A' when represented with the (A) 1D vertical growth and (C) 3D level set model. Mineral precipitation using the 1D vertical growth method (B) results in a vertical extension of reactive minerals across the fracture aperture. Alternatively, precipitation in the level set model (D) results in vertical and lateral propagation of reactive minerals. Mineral age is represented in number of time steps.

3.2.3 Fracture surface alteration

Reactive transport resulting in mineral precipitation on the fracture surfaces requires evolving the fracture surfaces accordingly. We use two different approaches for evolving the fracture surfaces: (1) a one-dimensional vertical growth model and (2) a three-dimensional surface evolution model. Solution of equation (3.3) provides estimates of local mineral precipitation rates, r_m, which lead directly to estimates of the rate of evolution, or the velocity, of the fracture surface:

$$v_n\big|_\Gamma = \frac{r_m}{\rho_m} \tag{3.13}$$

where v_n is the velocity normal to the fracture surface and ρ_m is the molar density of the precipitated mineral m.

The 1D model considers fracture surfaces represented as an assemblage of grid blocks each with a uniform surface elevation. The unit normal vector for the fracture surface within each grid block points in the z-direction such that:

$$\frac{dz_{u,l}}{dt} = v_n|_\Gamma \tag{3.14}$$

Figures 3.2A shows the initial surface structure for the 1D growth model.The black lines indicate non-reactive regions of the fracture surfaces and the red segments indicate regions along A-A' that contain reactive minerals. The black arrows indicate the corresponding local surface normals, $\vec{n}$. Figure 3.2B shows the resulting surface evolution after advecting the surface geometry through many time steps where the color scale represents mineral age, or the cumulative number of time steps each cell has been occupied by a precipitated mineral. The grey region indicates the initial geometry of the rock matrix. As previously noted, this 1D local surface alteration method has been used widely in reactive transport models to simulate surface dissolution (e.g. Detwiler and Rajaram, 2007; Szymczak and Ladd, 2009; Deng et al., 2016) and has been shown to work well, especially for problems with uniform surface mineralogy.

The 3D surface evolution model uses the level set method (Sethian, 1990) to evolve the distance functions representing the mineral assemblage of each fracture surface. The evolution of $\phi_m(\vec{x})$ is given by the time rate of change of $\phi_m(\vec{x})$:

$$\frac{d\phi_m}{dt} = \frac{\partial \phi_m}{\partial t} + \vec{v} \cdot \nabla \phi_m = 0 \tag{3.15}$$

By projecting the surface velocity components onto the local unit normal vectors, such that $v_n = \vec{v} \cdot \dfrac{\nabla \phi_m}{|\nabla \phi_m|}$, equation (3.15) simplifies to:

$$\frac{\partial \phi_m}{\partial t} + v_n |\nabla \phi_m| = 0 \tag{3.16}$$

which describes the evolution of $\phi_m(\vec{x})$ throughout the entire domain. Note, solution of the reactive transport equation only provides v_n at the fracture surface, Γ. To define v_n throughout the domain, a velocity extension step is necessary to project $v_n|_\Gamma$ along the normal vectors to each level set contour:

$$\frac{\partial v_n}{\partial t'} + \nabla v_n \cdot \nabla \phi_m = 0 \tag{3.17}$$

where v_n is a three-dimensional array that stores the surface normal velocity corresponding to all level sets in the domain, and t' is a temporary time variable.

Rather than update $\phi_m(\vec{x})$ over the entire domain it is more computationally efficient to localize solution of equation (3.17) to a small region surrounding the interface (Peng et al., 1999). However, this leads to large gradients in $\phi_m(\vec{x})$ at the boundaries of this interface region and the potential for numerical oscillations during the advection of $\phi_m(\vec{x})$ over time. The potential for non-physical oscillations in $\phi_m(\vec{x})$ can be prevented by periodically reinitializing $\phi_m(\vec{x})$ by solving:

$$\frac{\partial \phi_m}{\partial t'} + S(\phi_{m_o})(|\nabla \phi_m| - 1) = 0 \tag{3.18}$$

where $S(\phi_{m_o})$ is a smoothed sign function that is positive in the fluid domain, and negative in the solid domain:

$$S(\phi_m) = \frac{\phi_m(\vec{x})}{\sqrt{\phi_m(\vec{x})^2 + \delta(\vec{x})^2}} \tag{3.19}$$

and steady-state solution of equation (3.18) yields $|\nabla\phi_m| = 1$, which is, by definition, the signed distance function.

Figure 3.2C demonstrates application of the 3D level-set model to evolving the fracture surfaces to account for mineral precipitation. The vectors represent the local interface velocity, v_n, which is normal to the fracture surface at all reactive regions (red segments). Because the surface normals are no longer restricted to the z-direction, mineral precipitation at the fracture surface leads to three-dimensional alteration of the surface geometry. Figure 3.2D shows the resulting fracture surface geometries as the they evolve due to precipitation. Notably, unlike with the 1D vertical growth model, the 3D level-set method allows the precipitating minerals to spread across the fracture surface, which is qualitatively consistent with experimental observations.

3.2.4 Reactive alteration computational algorithm

Here we present an overview of the computational algorithm developed to incorporate and evaluate the 3D level-set method of tracking fracture surfaces subjected to mineral precipitation.

Depth-averaging for single-species reactive transport

To demonstrate and evaluate the 3D level-set method of tracking evolving fracture surfaces, we first simplified the flow and reactive transport equations presented in Section 4.2.1. This involved two steps: (1) depth-averaging the flow and reactive transport equations across the fracture aperture, and (2) reducing the set of multi-species reactive transport equations to consider a single equation representing a single reactive species.

Integrating equation (3.1) between z_u and z_l results in a depth-averaged flow equation:

$$\nabla \cdot \vec{q} = 0 \tag{3.20}$$

where $\vec{q}$, the fluid flux, is a two-dimensional vector that is described by the local cubic law:

$$\vec{q} = \frac{b^3 g}{12\nu} \nabla h \tag{3.21}$$

where b is the the fracture aperture, quantified at any location (x, y) as:

$$b(x, y) = z_u(x, y) - z_l(x, y) \tag{3.22}$$

g is the gravitational acceleration constant, ν is the kinematic viscosity, and h is the hydraulic head.

Depth-averaging the advection-diffusion-reaction equation for a precipitation reaction involving a single primary aqueous species and a single precipitating mineral leads to:

$$\nabla \cdot (\vec{q}\bar{c}) - \nabla \cdot (b\vec{\vec{D}} \cdot \nabla\bar{c}) = \bar{R} \tag{3.23}$$

where $\bar{c}$ is the depth-averaged concentration, $\vec{\vec{D}}$ is dispersion tensor and $\bar{R}$ is the local reaction rate, which must be quantified in terms of the depth-averaged concentration. The local dispersion tensor represents a combination of molecular diffusion and Taylor dispersion resulting from out-of-plane velocity variations. However, in regions where advection is the dominant transport mechanism, (Chaudhuri et al., 2008) demonstrated that advective fluxes are several orders of magnitude larger than dispersive fluxes. Thus, we use $\vec{\vec{D}} = D_m$ to include diffusion, which becomes important in low-velocity regions of the fracture.

The local reaction rate is potentially influenced by both reaction kinetics at the fracture surfaces and diffusive transport normal to the fracture plane (not directly represented in the depth-averaged formulation). When reaction kinetics at the fracture surface limit the precipitation rate, the local rate is governed by:

$$\bar{R}_r = k\left(1 - \frac{\bar{c}}{c_s}\right)^n \tag{3.24}$$

which, when combined with (3.23) to represent first-order surface reactions (n=1), can be nondimensionalized by rewriting in terms of a dimensionless concentration, $\bar{c}/c_s$, and a dimensionless distance, $x^* = \frac{x}{L}$, where L is the fracture length. This leads to two important dimensionless parameters:

$$Pe = \frac{\langle q \rangle}{D_m} \qquad \text{and} \qquad Da = \frac{kL}{\langle q \rangle} \tag{3.25}$$

where $\langle\rangle$ denotes averaging over the field. The Peclét number, Pe, relates diffusive to advective time scales, and the Damköhler number, Da, relates advection to reaction timescales. When $Pe < 1$, diffusion dominates the transport process and dampens the development of local perturbations in the reaction front. However, as Pe increases and advection becomes more important, instabilities in the reaction front may occur. Further, when reaction kinetics are sufficiently fast that $Da >> 1$, local reaction rates become sensitive to variability in the flow field and reaction rates become transport-limited.

When diffusion limits the precipitation rate the local reaction rate can be estimated using a mass transfer relationship of the form:

$$\bar{R}_d = \frac{Sh\, D_m}{2b}\, c_s\left(1 - \frac{\bar{c}}{c_s}\right) \tag{3.26}$$

where c_s is the solubility concentration of the precipitating mineral in terms of the primary dissolved species. The Sherwood number, Sh, depends on the geometry of the flow. For parallel-sided fracture, the asymptotic values of Sh are 4.86 and 7.56 for one and two reactive surfaces, respectively (Kays, 1966).

For cases where the reaction rate is influenced by both diffusive transport from the fracture surfaces and reaction kinetics at the surfaces, the effective reaction rate can be written such that the slowest rate controls the reaction:

$$\bar{R} = \frac{1}{\frac{1}{R_d} + \frac{1}{R_r}} \tag{3.27}$$

and, for the case of first-order reaction kinetics (n=1), this leads to an effective reaction rate coefficient:

$$k_{eff} = \frac{k}{1 + \frac{2k\,b}{Sh\,D_m\,c_s}} \tag{3.28}$$

Reactive transport and surface alteration algorithm

We developed a computational algorithm that integrates the depth-averaged representations of the flow and transport equations described above with the surface evolution models described in Section 3.2.3. This involved representing the fracture using a 3D domain to establish the distance function corresponding to the different minerals on the fracture surfaces, which allowed us to define and track the fracture surfaces using the 3D level-set method. Prior to each solution of the flow and reactive transport equations, we determined the local fracture aperture using (3.11) and (3.22). The block diagram in Figure 3.3 depicts the computational algorithms for the 1D growth model and the 3D level-set model. The source code, developed using Matlab, is also available at `https://github.com/spl-detwiler/LS_SFRT`.

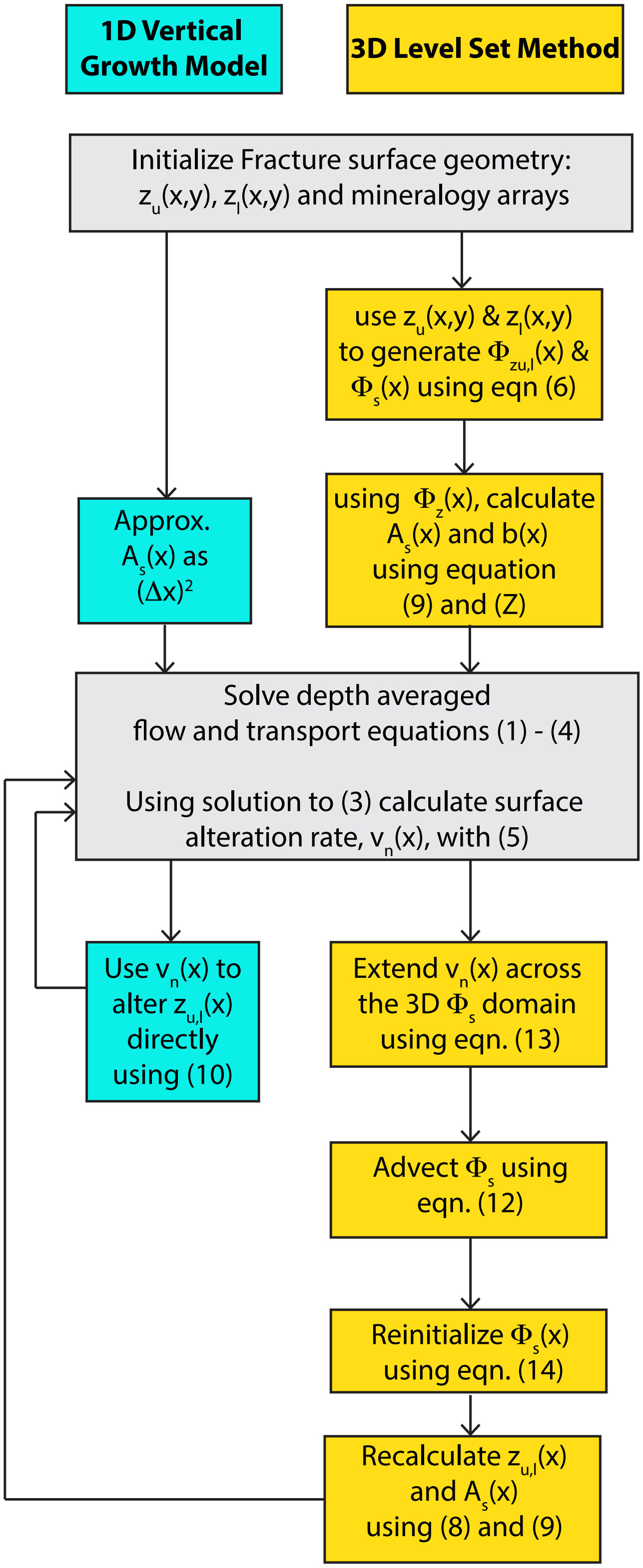

Figure 3.3: Algorithms for simulating precipitation-induced surface geometry alterations. The column on the left shows the algorithm used for the 1D vertical growth model, while the column on the right presents the algorithm for the 3D level set surface alteration model.

The level set equations were integrated in time using a first-order forward Euler method. In order to ensure that the Courant-Friedrichs-Lewy (CFL) conditions were met during integration of equation (3.17) and (3.18), we chose $\Delta t' = 0.5\Delta x$. Time integration of equation (3.16) was limited by both the CFL condition and by the physical representation of the reactive transport problem. In order to limit large variations in aperture between flow and transport solves and also accommodate the CFL condition, we chose Δt as the minimum of the 1D surface alteration time stepping criteria and the CFL criteria. In equations (3.16) - (3.18), we used a first-order upwinding method to approximate the local spatial derivative (Peng et al., 1999).

3.3 Results

Here we present results from simulations aimed at evaluating the computational algorithm presented in the previous section and demonstrating the influence of mineral heterogeneity on mineral precipitation and transmissivity alteration. We evaluate the model through comparison to an idealized analytical solution and then test the ability of the model to conserve precipitated mass in progressively more heterogeneous fractures. We then compare results from the 1D vertical growth model and the 3D level set model to results from a previously reported experiment. Finally, we present parametric simulations that demonstrate the impact of reaction kinetics (i.e., range of Da) on the mineral precipitation process in a heterogeneous fracture.

3.3.1 Evaluation of the 3D level-set model

To systematically evaluate the ability of the 3D level set model to predict surface evolution caused by mineral precipitation we considered an idealized 1D fracture with uniform aperture and mineralogy and then extended our analysis to a 2D fracture in which both aperture and mineral heterogeneity were added.

Comparison to analytical solution of 1D advection-reaction equation

To evaluate the ability of the the coupled reactive transport and level-set surface evolution model to predict fracture alteration, we compared simulations to a simple analytical solution for advective-reactive transport through a parallel plate fracture with uniform surface mineralogy. This analytical solution assumes c is fully mixed across the aperture, neglects longitudinal diffusion, and describes injection of a supersaturated solution at constant flow rate. Solving (3.23) for these conditions results in a 1D concentration profile:

$$c(x) = c_s + (c_o - c_s) exp(-\frac{k}{c_s q} x) \tag{3.29}$$

which can be combined with (B.7) and integrated with respect to time to obtain the time-dependent the aperture profile:

$$b(x,t) = b_o + \frac{t}{\alpha \rho}(c_o - c_s) exp(-\frac{k}{c_s q} x) \tag{3.30}$$

Results from the simulations demonstrate excellent agreement between the 3D level set model and this analytical solution (Figure S2). At the lowest Da, $Da = 0.014$, both the 3D level set and 1D vertical growth model produced a maximum error of approximately 0.012%. At higher Da, precipitation induced larger gradients in the aperture profile and the 3D level set method reproduced these gradients more accurately than the 1D vertical growth model. For the highest Da simulation, $Da = 14$, the 3D level set model overestimated the inlet aperture by only 3%, while the 1D vertical growth model overestimated the inlet aperture by 11%.

Mass conservation

Though the reactive transport equations are inherently mass conserving, the level set method is known to generate mass during the reinitialization process (Osher and Fedkiw, 2003; Sethian and Smereka, 2003). To assess the ability of the algorithm to conserve mass, we simulated precipitation over a 7 order-of-magnitude range of Da for fractures that contained: (1) no surface roughness with uniform mineralogy, (2) no surface roughness with mineral heterogeneity, and (3) surface roughness with mineral heterogeneity. To quantify mass conservation, we calculated the discrepancy between the mass of ions removed from solution due to precipitation and the mass of ions precipitated on the fracture surfaces (Figure S3). In all simulations, the level set method conserved mass well, producing a maximum cumulative mass error of 1% after the fracture transmissivity had been reduced by an order of magnitude.

3.3.2 Comparison of 1D growth model and 3D level-set model for precipitation in a heterogeneous fracture

To assess the potential importance of representing surface evolution as a 3D process we compared simulation results using the 1D vertical growth model and the 3D level-set method for the same initial fracture. To further assess the ability of the different modeling approaches to predict fracture alteration in heterogeneous fractures, we reproduced conditions from a mineral precipitation experiment in a transparent rough-walled fracture (Jones and Detwiler, 2016). During this experiment, a supersaturated $CaCO_3$ solution ($\frac{IAP}{K_{sp}}$=27.5) was injected into a 15 x 15 cm at 0.5 ml/min. The fracture consisted of a rough glass (non-reactive) surface mated with a smooth glass surface with localized regions of precipitated $CaCO_3$, which acted as preferential precipitation locations. We note that for the supersaturated $CaCO_3$ solution used in the experiments, $\frac{IAP}{K_{sp}} \sim \frac{c}{c_s}$ where c is the concentration of Ca^{++}

and c_s is the concentration of Ca^{++} at equilibrium (Figure S1), so we used the single-species reactive transport model presented in Section 3.2.4 to simulate transport of Ca^{++}. The experimental solution was similar to that used by Reddy and Nancollas (1971) who measured the reaction-rate constant, $k = 10^{-6.86}$ mol $\cdot$ m $^{-2} \cdot$ s^{-1}.

Due to the computational demands of the level set calculations, we simulated $CaCO_3$ precipitation in a 0.6 x 1.2 cm sub-section of the fracture. To minimize the influence of boundary effects in this sub-domain, we applied periodic boundary conditions on the boundaries parallel to the mean flow direction. Figure 3.4A and Figure 3.4B show the $CaCO_3$ and aperture distributions used to initialize both the 1D vertical growth and 3D level set models. The initial aperture distribution had a mean of 0.0135 cm with a standard deviation of 0.0045 cm. The amorphous $CaCO_3$ reaction sites were distributed heterogeneously across the fracture plane and covered 13% of the fracture surface. We used the measured aperture to provide discrete values of the interface location when defining $\phi_s(\vec{x})$, and represented the initial $CaCO_3$ reaction sites as flat regions with an initial height of 5 μm.

Figure 3.5 shows simulation results from the 1D vertical growth and 3D level set simulations at $t^* = 0.1, 1.0, \text{and } 3.5$. We define t^* as t/t_f, where t_f is the time required to fill a fracture with precipitating mineral when exposed to a constant inlet concentration, c_o:

$$t_f = \frac{\rho_m \langle b \rangle}{k(1 - \frac{c_o}{c_s})} \tag{3.31}$$

For the simulations, the supersaturated $CaCO_3$ solution was injected from left to right, and all reactions were limited to regions of the fracture that contained $CaCO_3$. Images in the first two columns on the left of Figure 3.5 show the depth-averaged steady state concentration fields, $\bar{c}$. The two columns on the right show the normalized aperture fields, b/b_o, where b_o is the initial aperture distribution; small b/b_o indicates regions where mineral precipitation reduced fracture aperture, and $b/b_o \sim 1$ indicates regions where mineral precipitation did not

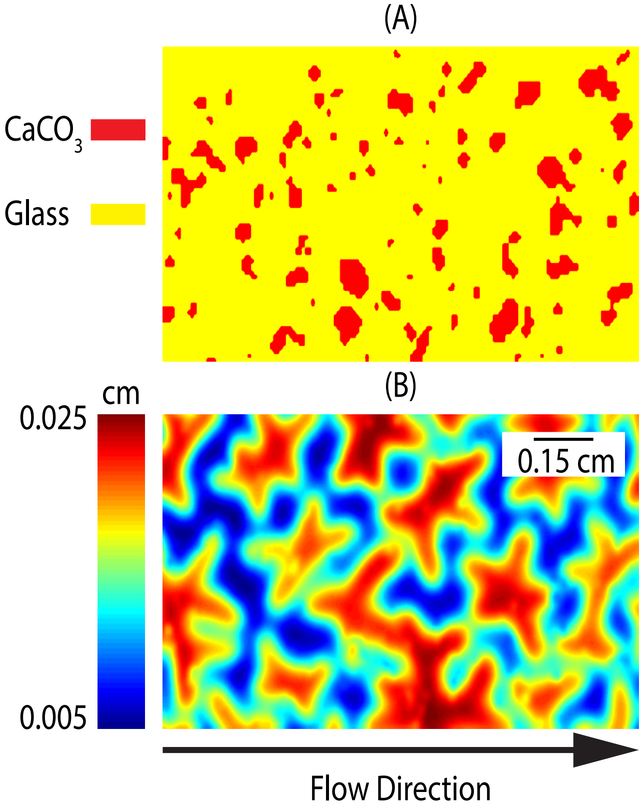

Figure 3.4: Experimental measurements used to initialize the reactive transport simulations. (A) The initial $CaCO_3$ distribution. Red regions indicate the location of reactive $CaCO_3$, and yellow indicates the location of non-reactive soda-ash glass. (B) The initial aperture distribution.

significantly alter fracture aperture; $b/b_o = 1$ is shown in white. Streamlines superimposed on the b/b_o fields provide a measure of tortuosity, τ, by normalizing the average length of the streamlines by the fracture length.

At the beginning of the reactive transport simulations, the 1D vertical growth and 3D level set model predicted very similar distributions of $\bar{c}$ and b/b_o. At $t^* = 0.1$, the $\bar{c}$ fields show that the initial surface roughness and mineral heterogeneity induced variations in the distribution of dissolved ions. Similar to the normalized concentration fields, the b/b_o fields show good agreement; both fields indicate $b/b_o \sim 1$ across the domain and $\tau = 1.07$.

At intermediate time, results from the 1D vertical growth and 3D level set models began to differ. At $t^* = 1.0$, the 3D level set model predicts some lateral propagation of $CaCO_3$ across the fracture plane, which is highlighted in the boxed region of the level set b/b_o field,

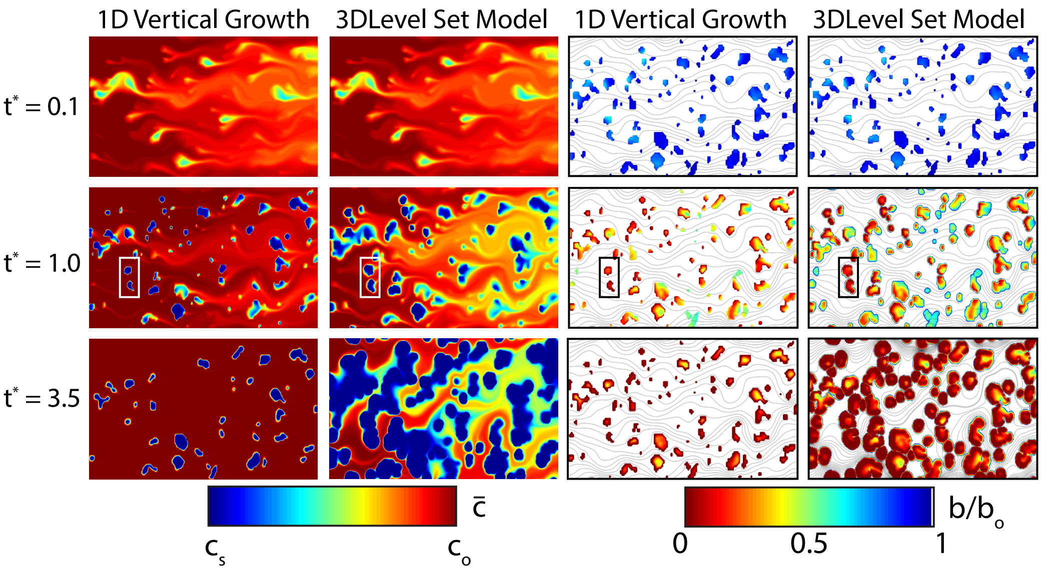

Figure 3.5: Simulation results from the 1D vertical growth and 3D level set surface alteration models at $t^* = 0.1$, 1.0, and 3.5. 3D mineral growth enhances variability in $\bar{c}$, which is not represented in reactive transport simulations that represent surface alterations as a 1D process. The normalized aperture fields, b/b_o, superimposed with the simulated streamlines (grey lines) show that lateral growth of $CaCO_3$ significantly impacts tortuosity. These frames are a subset of the results shown in Movie S1.

where two initially isolated $CaCO_3$ reaction sites merged to create a single, larger region of reactive $CaCO_3$. This growth process was not predicted by the 1D vertical growth model. However, at intermediate time, the lateral expansion of $CaCO_3$ did not significantly impact flow; the vertical growth and level set model predict $\tau = 1.12$ and 1.16, respectively.

At $t^* = 1.0$, 3D mineral growth increased the local reactive surface area, which led to notably different $\bar{c}$ distributions. The boxed zone of the vertical growth $\bar{c}$ field shows $\bar{c} = c_o$ except at the $CaCO_3$ reaction sites. Dissolved ion concentrations remained close to c_o across the fracture, which indicates that the fracture-scale precipitation rate has decreased. Alternatively, precipitation in the boxed region of the 3D level set model led to enhanced variability in $\bar{c}$, and at the fracture outlet, $\bar{c}$ was lower when compared to $t^* = 0.1$, which indicates that the increase in reactive surface area has slightly enhanced precipitation rates across the domain.

At late time, the differences between the 1D vertical growth and 3D level set models became more pronounced. The level set results at $t^* = 3.0$ show that small b/b_o values covered nearly the entire width of the fracture. Local sealing of the fracture aperture focused flow into progressively narrower flow paths, which focused large $\bar{c}$ into two dominant pathways that persisted the fracture length. In the 1D vertical growth model, $b/b_o = 0$ only around the edges of the initial $CaCO_3$ reaction sites and $\bar{c} \sim c_o$ across the entire domain indicating reactions have ceased.

Figure 3.6A shows the temporal evolution of τ for simulations with both models. For the 3D level set model (blue) τ increases monotonically with time to τ=1.52 at t^*=3.8, an increase of 42% from the initial value. Conversely, for the 1D vertical growth model (red) τ increases to τ=1.13 (an increase of 5%) at t^*=1.5 and then ceases to change. Figure 3.6B plots the corresponding decrease in predicted transmissivity, $T = \frac{\langle q \rangle}{\nabla h}$, for each model. As expected, at early time (e.g. $t^* < 0.5$), the transmissivities predicted by both models were similar. However, for $t^* > 0.5$, the fracture-scale transmissivity predictions diverge. For $t^* \gtrsim 1.5$ the 1D vertical growth model predicts the transmissivity reaches a constant value of about 76% of the initial transmissivity but for the 3D level set model, the transmissivity continues to decrease at an increasing rate.

The differences between the 3D level set simulation and 1D vertical growth simulation indicates that lateral growth may be an important mechanism in the evolution of transport properties caused by mineral precipitation. To examine whether the results from the 3D level set simulations are supported by experimental observations, we compare the experimentally observed distribution of precipitated CaCO3 to the results from the 3D level-set simulations (Figure 3.7). We note that because the simulations were carried out in a subset of the entire fracture, the boundary conditions are different between the simulation and experiment. In particular, we specify uniform head along the inlet and outlet for the simulations, but in

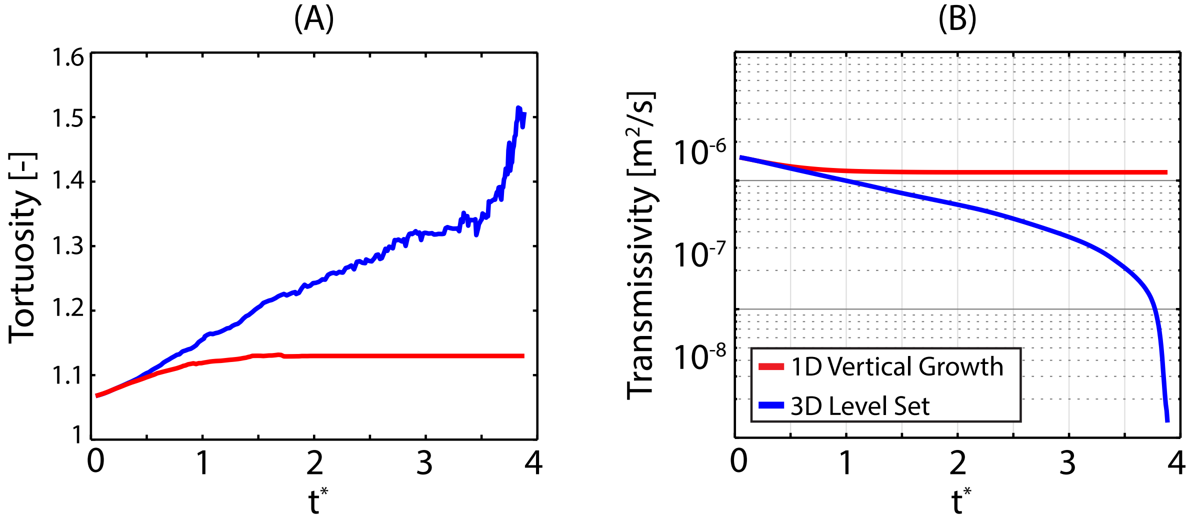

Figure 3.6: Tortuosity, τ (A), and transmissivity (B) evolution for the 1D vertical growth (red) and 3D level set (blue) reactive transport simulations. At $t^* = 1.5$, both the transmissivity and tortuosity stop changing in the 1D vertical growth model.

this region of the experiment, it is likely that the head varied along the inlet and outlet. However, the mean head gradient is consistent between experiment and simulation.

The upper frame of Figure 3.7 shows the locations of the precipitated regions of $CaCO_3$ at t^*=0.0 and 1.3 measured during the experiment. This binarized field shows that precipitation at the individual $CaCO_3$ regions led to lateral spreading of these regions, which caused some $CaCO_3$ regions to coalesce and form larger clusters of $CaCO_3$. The superimposed preferential flow path (PFP) highlights the region through which enhanced solute flux was observed during injection of a conservative dye tracer. Thicker dark blue regions in the vicinity of the PFP indicate enhanced growth of $CaCO_3$ associated with the preferential flux of dissolved ions. Figure 3.7 also shows that some isolated $CaCO_3$ regions developed in initially $CaCO_3$-free regions. The ability for new reaction sites to nucleate on the fracture surfaces is not included in the reactive transport model, but these 'new' reaction sites accounted for only $\sim 5\%$ of the minerals precipitated during the experiment.

The lower frame in Figure 3.7 shows the simulation results in the same region of the fracture with streamlines superimposed to highlight preferential flow paths. Despite the difference

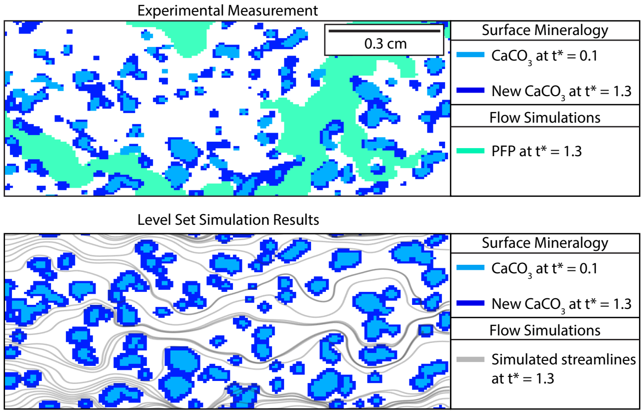

Figure 3.7: Frame A: Experimental measurement of the $CaCO_3$ distribution at early ($t^* = 0.1$) and late time ($t^* = 1.3$) from the experiment presented in Jones and Detwiler (2016). The measurement highlights the lateral growth of $CaCO_3$ throughout the experiment. Simulation results (Frame B) show a similar lateral propagation of $CaCO_3$ and demonstrate that precipitation promotes flow focusing between reaction sites.

between the experimental and simulated boundary conditions, the simulation results predict similar lateral spreading of the $CaCO_3$ regions. Simulated precipitation of $CaCO_3$ and the corresponding spreading and coalescence of $CaCO_3$ regions led to focusing of preferential flow along narrower paths as the simulation progressed. The existence and focusing of preferential flow led to more pronounced growth and spreading of $CaCO_3$ regions in the vicinity of preferential flow (as indicated by higher density of streamlines).

3.3.3 The influence of reaction kinetics on mineral precipitation

To explore the role of local reaction kinetics on precipitation in a heterogeneous fracture, we ran two additional simulations ($k = 10^{-5.6}$ and $10^{-8.7}$ $\text{mol} \cdot \text{m}^{-2} \cdot \text{s}^{-1}$) with the same conditions used in Section 3.3.2 ($k = 10^{-6.8}$ $\text{mol} \cdot \text{m}^{-2} \cdot \text{s}^{-1}$) and compared the results for these simulations, where $Da = 40$, 0.03, and 2.60, respectively.

For $Da = 0.03$, reaction kinetics were slow enough that $\bar{c} \sim c_o$ along the entire length of the fracture (Figure 3.8). As a result, precipitation rates were constant across each reactive mineral, which led to a uniform extension of the reaction sites across the fracture plane and

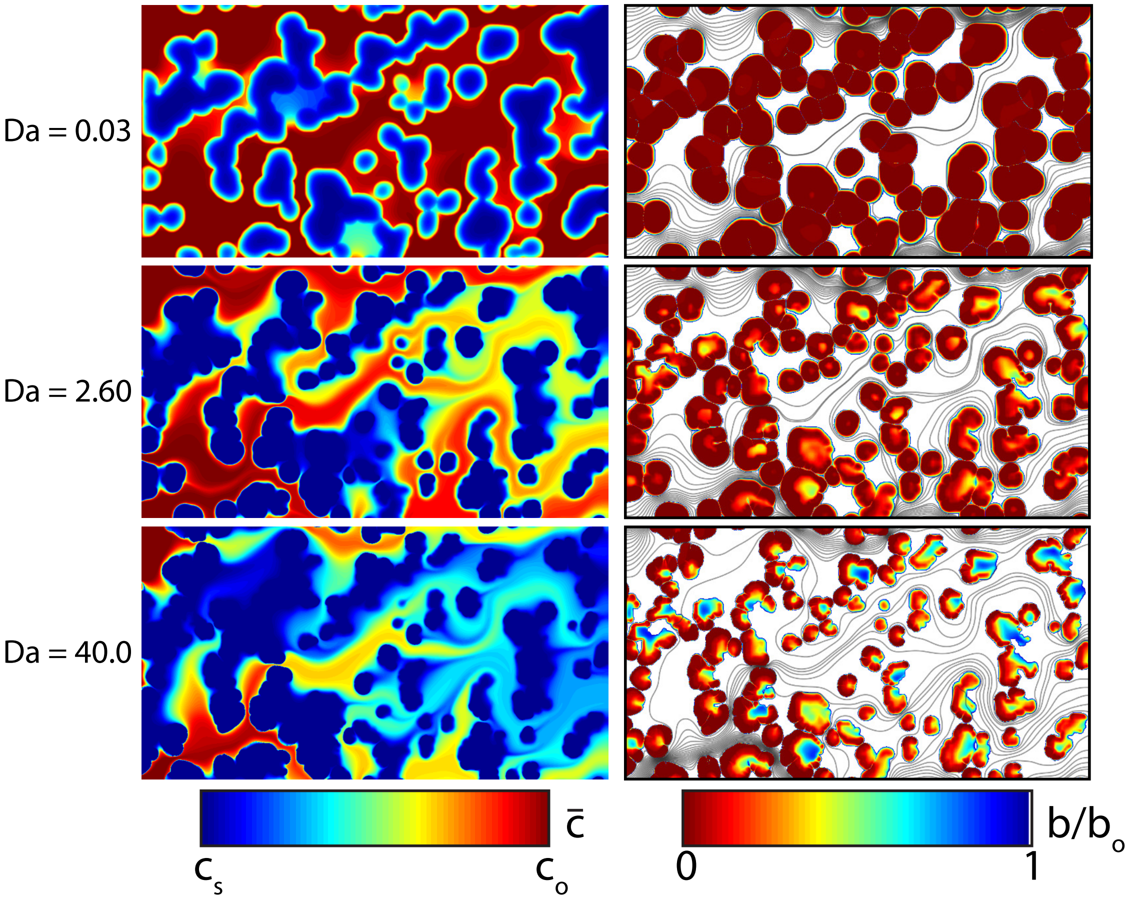

Figure 3.8: $\bar{c}$ and b/b_o superimposed with the simulated streamlines for $Da = 0.03$, 2.6, and 40. Simulation results are shown after precipitation has reduced transmissivity by an order-of-magnitude. Lateral growth of $CaCO_3$ is fastest at larger Da, which enhances variability in $\bar{c}$. Preferential flow is most pronounced at lower Da. These frames are a subset of the results shown in Movie S2, S1, and S3.

aperture that sealed large portions of the fracture. Because $b/b_o = 0$ across the majority of the fracture, flow was focused into a thin preferential path that extended the length of the domain. Figure 3.9A provides a quantitative measure of τ and shows that at the time of fracture sealing, $\tau = 1.41$, a 32% increase in tortuosity.

At $Da = 2.6$ and 40, reaction kinetics were fast enough that concentrations gradients developed along the mean flow direction. This is most notable at $Da = 40$, where precipitation was fastest along the periphery of the $CaCO_3$ regions, which led to $b/b_o = 0$ along the reactive mineral borders, and $b/b_o \sim 1$ near the center and trailing edges of the reaction sites. Fast precipitation rates along the periphery of the $CaCO_3$ regions enhanced lateral spreading across the fracture plane. At the fracture inlet, this focused flow into a thin preferential flow path. Because reaction rates decreased along the fracture length, this preferential flow path became less prominent, and flow became more uniformly distributed at the fracture outlet. This transition coincided with a 54% increase in tortuosity to $\tau = 1.64$ at the time of fracture sealing.

The relatively fast kinetics at $Da = 40$ also limited dissolved ion transport into slow-flow regions that developed throughout the precipitation process. This is most noticeable near the fracture inlet, where $\bar{c} \sim c_s$ in regions of the fracture where $b/b_o \sim 1$. This disparity in $\bar{c}$ across the width of the fracture indicates that precipitation reactions are limited to $CaCO_3$ regions that border to developing preferential flow paths. In the slow-flow regions far from the preferential flow paths, diffusive-transport does not replenish dissolved ion concentrations, and the local reaction rates approach zero.

Figure 3.9B shows the transmissivity evolution for the Da simulations. The transmissivity profiles demonstrate that the shortest normalized sealing time, occurred at low Da, and the largest normalized sealing time occurred at $Da = 40$. This relationship between sealing rates and Da indicates that, although slow kinetics enhanced preferential flow due to the prevalence of locally sealed aperture, the uniform growth of the reactive minerals led to

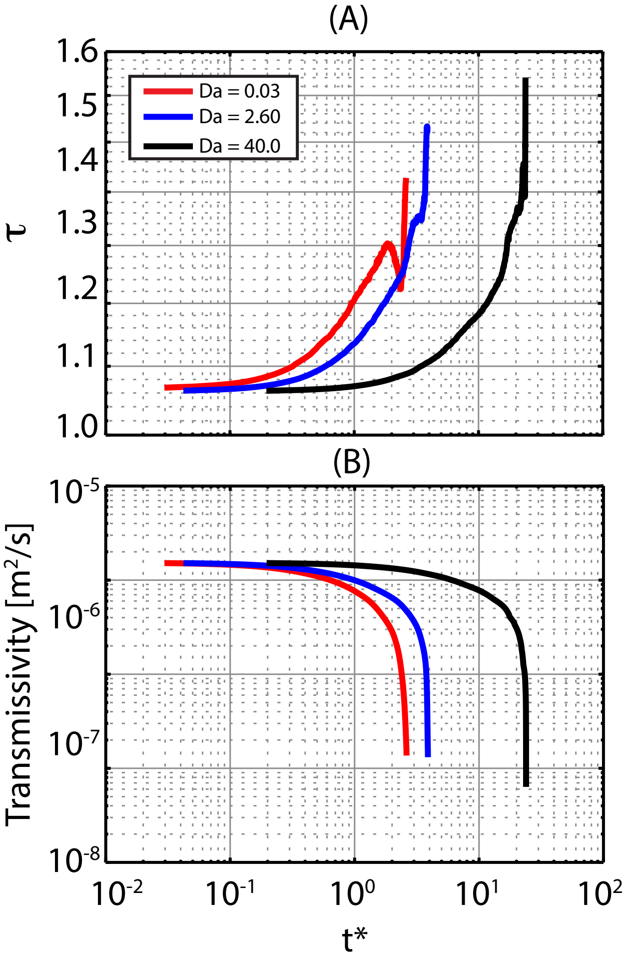

Figure 3.9: Simulated tortuosity (τ) and transmissivity (T) for Da = 0.03, 2.6, and 40. τ at the time of fracture sealing indicates that tortuosity is sensitive to precipitation induced fracture surface alterations. Fracture sealing timescales increase with Da. The flow and transport alterations that correspond with the τ and T profiles above are shown in Movie S2, S1, and S3, respectively.

rapid reduction in transmissivity. Conversely, enhanced lateral growth promoted by the fast kinetics limited reactions to $CaCO_3$ regions bordering the evolving preferential flow path, which increased the timescale required for fracture sealing.

3.4 Discussion

Here, we discuss the potential impact of ignoring small-scale mineral heterogeneity when predicting precipitation-induced flow and transport alterations in a fracture (Section 3.4.1) and the influence of different boundary conditions on the evolution of the precipitation process (Section 3.4.2). Lastly, we discuss the potential scale-dependence of precipitation-induced reactive alteration processes (Section 3.4.3).

3.4.1 The importance of small-scale heterogeneities

The results presented in Section 3.3.2 demonstrate that 3D surface alterations, which play an important role during precipitation in a fracture, are sensitive to both mineral distribution and Da. However, the computational demands of the level set approach and other immersed boundary models limit predictive simulations over large spatial scales (Yu and Ladd, 2010; Li et al., 2010; Kling et al., 2017) . An alternative approach to representing mineral heterogeneity is through the use of equivalent homogenous fracture-scale properties (Deng et al., 2016; Menefee et al., 2017). To examine the effects of upscaling small-scale mineral heterogeneity, we performed an additional simulation under the conditions described in Section 3.3.2. In this simulation the heterogeneous mineral distribution from Figure 3.4 was replaced with a uniform mineral surface with local effective reactive surface area equal to the total reactive surface area normalized by the area of the bottom fracture surface. We simulated precipitation using the 1D vertical growth model, which is reasonable because the two surface alteration methods produce similar results in uniform mineralogy fractures (see Section 3.3.1).

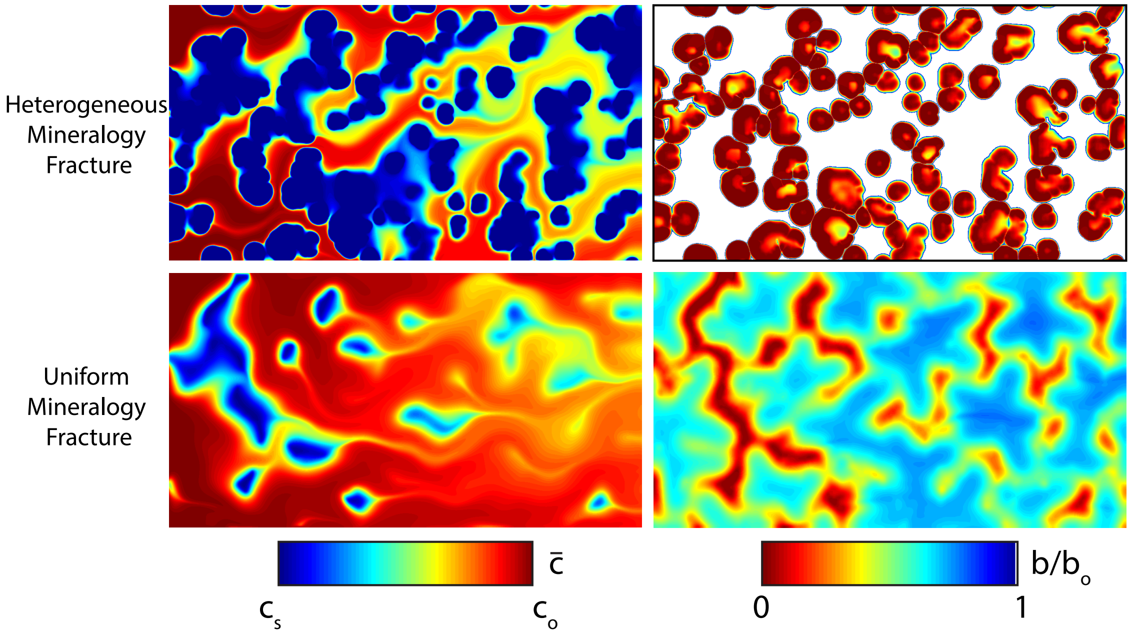

Figure 3.10: $\bar{c}$ and b/b_o from the heterogeneous mineralogy and uniform mineralogy fractures after precipitation reduced transmissivity by one order-of-magnitude. In the heterogeneous fracture, flow focusing between reactive minerals led to widespread precipitation and larger variability in $\bar{c}$. In the homogeneous mineralogy fracture, small b/b_o bands oriented perpendicular to flow led to more uniformly distributed $\bar{c}$ across the fracture.

Mineral precipitation in a uniform mineralogy fracture is expected to seal preferential flow paths and redistribute solute fluxes, which leads to the formation of precipitate bands oriented perpendicular to the mean flow direction that rapidly seal the fracture (Chaudhuri et al., 2008, 2012). The b/b_o field from the homogeneous mineralogy simulation (Figure 3.10) is consistent with these expectations. However, results from the heterogeneous mineralogy simulations demonstrate that precipitation sealed larger portions of the domain than in the uniform mineralogy fracture. Because large portions of the fracture were sealed, flow and $\bar{c}$ became highly localized, and precipitation was limited to $CaCO_3$ regions that bordered the developing preferential flow path.

The discrepancy in b/b_o and $\bar{c}$ indicates that the reactive transport is not only influenced by the initial aperture distribution, but can also be affected by the local mineralogy. This suggests that two competing length-scales control precipitation-induced alteration processes: (i) the correlation length of the aperture distribution, which controls the local flow field, and (ii) the separation length between reactive minerals which controls the local precipitation rate within the correlation length of the aperture distribution. When (ii) is much smaller than (i), averaging local mineralogy may lead to reasonable estimates of the precipitation process. However, when (i) and (ii) are similar in magnitude, as is the case in this simulation, small-scale variations in both distributions can effect the feedback between precipitation and fracture surface alterations.

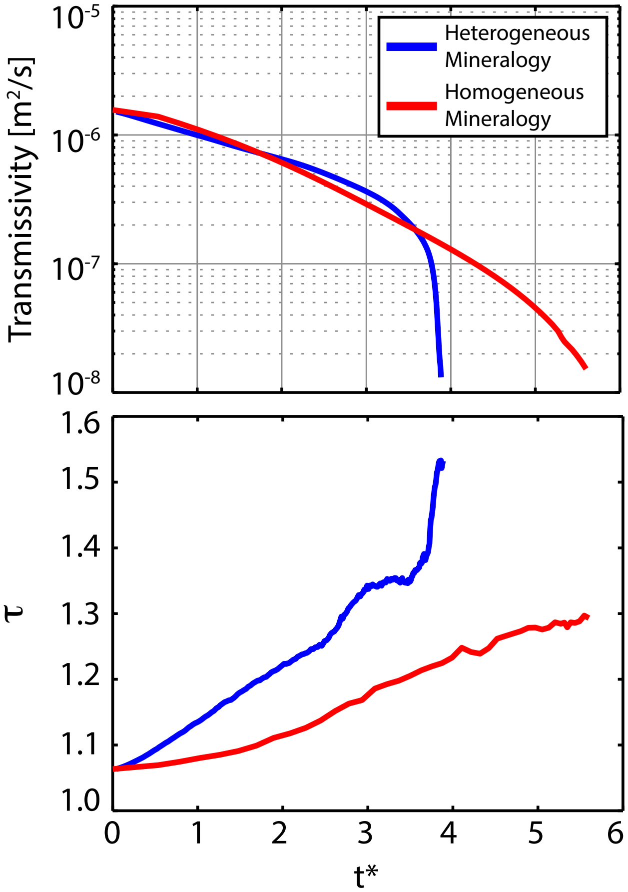

Figure 3.11: Simulated τ and transmissivity using a uniform mineralogy fracture (red) and heterogeneous mineralogy fracture (blue). Flow focusing between reactive minerals in the heterogeneous fracture resulted in 25% increase in τ compared to the homogeneous fracture. Despite this, the heterogeneous fracture sealed 30% faster than the homogeneous fracture.

Although precipitation formed a small-aperture band oriented perpendicular to flow in the uniform mineralogy fracture, Figure 3.11A shows that transmissivity was reduced at a faster rate in the heterogeneous mineralogy fracture. A significant cause of this discrepancy is a feedback between precipitation and local reactive surface area: as precipitation increases the solid-volume of $CaCO_3$, the reactive surface area also increases, which in turn enhances the local precipitation rate. In the heterogeneous fracture, this feedback is largely influenced by lateral growth of $CaCO_3$ across the fracture plane and is directly quantified using (12); in the uniform mineralogy fracture, this feedback is not accounted for because local reactive surface area is based on the measured initial surface area.

In porous media simulations, the feedback between precipitation and reactive surface area is often accounted for using constitutive relationships that decrease reactive surface area as the pore-space is reduced (Molins, 2015; Garcia-Rios et al., 2017). Our preliminary results suggest that the application of these relationships to fracture surfaces is not appropriate because precipitation increases the lateral extent, and surface area, of the reactive minerals. Reactive transport simulations that employ robust surface tracking methods may facilitate the development of similar constitutive relationships for fractures and provide the ability to quantitatively examine how heterogeneity length-scales and transport conditions affect the feedbacks between precipitation, transmissivity, and reactive surface area.

3.4.2 Precipitation under constant head boundary conditions

An important consideration when predicting the impact of reactive alteration is the influence of boundary conditions on the results. Laboratory experiments are often carried out under constant flow conditions for experimental expedience, but natural conditions may range from constant flow conditions (e.g., near an injection or extraction well) to constant head conditions. The simulations above show that there is a dynamic response between the development of preferential flow paths and the local velocity: as precipitation focused flow into smaller preferential flow paths, the local velocity increased, which drove larger solute concentrations further into the fracture. This increase in local velocity is a direct result of the constant flow boundary conditions imposed throughout the simulations.

Under constant head boundary conditions, feedback between preferential flow path generation and local velocity will be less pronounced. Reduction in fracture-scale transmissivity reduces the overall flow rate which alters the relative rates of advection, diffusion, and reaction kinetics. When Pe is initially much greater than 1, the precipitation process is strongly controlled by the relative rates of advection and reaction kinetics. Therefore, a reduction in local velocity will increase Da; as the simulation results in Section 3.3.3 show, this increase in Da can enhance lateral growth of the individual minerals and preferential flow across the domain. Further, under these conditions, precipitation rates will be fastest along the periphery of the reactive minerals and may be negligible far from the primary flow paths.

However, as precipitation continues to reduce flow, diffusion becomes the dominant transport process. As the reactive transport transitions to low-Pe conditions, diffusion will dampen variations in the precipitation rate that were driven by variations in the local velocity, leading to more uniform growth of the reactive minerals. Section 3.3.3 shows that uniform growth increases the rate of fracture-transmissivity reduction. This suggests that the gradual transition from advection- to diffusion-dominated transport under constant head boundary conditions will decrease the fracture sealing timescale compared to similar constant flow conditions.

3.4.3 Scale dependence and parallelization

Despite the qualitative agreement between the level set simulations and the experiments performed by Jones and Detwiler (2016), we expect that the feedback between precipitation and flow in our simulations is dampened by the small length-scale of the fractures. Previous numerical and analytical analyses of dissolution reactions demonstrate that the scale dependence results from the influence of the uniform head boundary condition at the fracture outlet on local flow rates within the fracture. Head perturbations within the fracture lead to larger local gradients; the relative magnitude of these head gradient perturbations are larger in a short fracture than a long fracture due to the proximity of the uniform-head boundary. In the case of dissolution, these perturbations lead to a positive feedback between local flow and reaction rates such that fracture alteration patterns are sensitive to fracture length. For the case of precipitation, the negative feedback between flow and reaction rates will also likely exhibit scale dependence (Cheung and Rajaram, 2002; Szymczak and Ladd, 2012).

The length scale of our simulations is limited by the computational costs of the level set surface alteration algorithm, which relies upon the built-in linear algebra optimization in MATLAB. More formal parallelization of the level set surface alteration algorithm using a high-level programming language will significantly reduce computation time and provide the ability to simulate precipitation at the meter scale and above.

3.5 Concluding Remarks

We developed a reactive transport model and applied it to quantify the role of mineral heterogeneity on precipitation-induced alteration of fracture transport properties. Testing the model against an idealized analytical solution for a fracture with uniform mineralogy revealed that a simple 1D surface evolution model reproduces results quite well. However, when heterogeneity was introduced, only the 3D level-set model of surface alteration produced results similar to previous experimental observations (Jones and Detwiler, 2016). This resulted from the importance of lateral, or in-plane, spreading of local reaction sites as precipitation progressed. The simulation results were consistent with the experimental observations, where lateral growth of precipitated minerals led to the development and enhancement of preferential flow paths, which further influenced local precipitation rates.

We used the model to investigate the importance of the relative magnitude of advection and reaction kinetics (as quantified by Da) on the precipitation process. For slow kinetics ($Da = 0.03$), uniform growth of individual reaction sites focused flow into a single, well-defined flow path. For faster kinetics (e.g. $Da = 2.6$ and 40), precipitation rates were fastest at the fracture inlet and preferential flow was not enhanced at the fracture outlet. Despite more uniform flow towards the outlet, the disparity in local velocity across the fracture induced large variations in the local precipitation rate, which increased the fracture-sealing timescale. These results suggest two important length scales that strongly influence the reactive alteration of the fracture: (i) the length-scale of aperture variability, which controls flow and transport, and (ii) the separation length between reactive minerals, which controls local reaction rates.

Our simulations demonstrate the importance of mineral heterogeneity on the evolution of transport processes in fractures, but the level-set method for representing the surface evolution is computationally intensive. However, results from a demonstration simulation where the heterogeneous mineralogy was represented by specifying a uniform mineralogy with reduced surface area to account for the influence of heterogeneity suggest that upscaling the reactive alteration process may be challenging. Precipitation enhanced transport limitations in the heterogeneous mineralogy fracture, but transmissivity was reduced at a slower rate in the homogeneous mineralogy fracture. A significant cause of this is the feedback between local mineral reactions and reactive surface area, which suggests that development of fracture-specific constitutive relationships quantifying the relationship between mineral precipitation and generation of reactive surface area may improve results from simplified models of mineral precipitation on heterogeneous surfaces.

Lastly, the results presented here demonstrate the need for further development of reactive transport models that capture three-dimensional surface geometry changes that result from precipitation/dissolution reactions in a heterogeneous fracture. While the role of surface roughness has been explored in much detail, the influence of mineral heterogeneity during reactive flows remains relatively elusive. Using continuum scale approaches to quantify the mechanisms that control the evolution of flow, transport, and reactions in these heterogeneous environments can mislead interpretations of the role that small-scale mineral heterogeneity plays during the evolution of a fractured rock.

Chapter 4

Mineral precipitation in fractures: When do surface heterogeneities matter?

4.1 Introduction

Fractures provide preferential paths for fluid flow through low-permeability crustal rocks. However, in many geologic environments, fluid-rock reactions can lead to mineral precipitation, which reduces fracture transmissivity (Henneberger and Browne, 1988; Boles et al., 2004; Verma and Pruess, 1988). Precipitation-induced transmissivity reduction enhances fracture cementation during natural vein filling processes (Lee and Morse, 1999; Kling et al., 2017) and also provides a promising mechanism to trap anthropogenic contaminants in the subsurface (Ryerson et al., 2013; Menefee et al., 2017). However, these transmissivity reductions may increase pore-pressures and lead to dynamics failure cycles that provide leakage pathways for natural and anthropogenic contaminants (Audet and Burgmann, 2014; Vass et al., 2014; Yarushina and Bercovici, 2013). Understanding the mechanisms that control precipitation-induced transport alterations, and the corresponding time-scales over which precipitation occurs, is an important step towards a quantitative understanding of both natural and engineered fracture alteration processes.

Mineral precipitation in fractures occurs when the local pore-fluids become oversaturated with dissolved ions that react and become incorporated onto the fracture surfaces. As precipitation depletes ions from the local pore-fluids, reactions become limited by transport processes that replenish dissolved ion concentrations at the fracture surfaces (Bons, 2001; Ankit et al., 2015). When this replenishment process is driven by advection of a supersaturated fluid, precipitation rates and the distribution of precipitated minerals are strongly influenced by the local magnitude of the advective flux of dissolved ions (Chaudhuri et al., 2008, 2012). Because fracture surface roughness, and thus fracture aperture, can vary over orders-of-magnitude (e.g., Hakami and Larsson, 1996; Oron and Berkowitz, 1998), mineral precipitation can lead to surface alterations that dynamically change the local advective fluxes that alter the reactive transport over time (Jones and Detwiler, 2018).

Precipitation-induced flow alterations are enhanced by variations in fracture surface mineralogy. For example, in a rough-walled fracture with uniform surface mineralogy, precipitation will initially be fastest in the large-aperture regions that carry the largest fluxes of dissolved ions (Chaudhuri et al., 2012). As a result, precipitation will fill large-aperture regions, which progressively smooths the two surfaces and dampens variations in the initial advective fluxes over time. Alternatively, when minerals are heterogeneously distributed on the fracture surface, local precipitation reactions become controlled not only by the local advective flux, but also by the availability of reactive minerals (Menefee et al., 2017). Under these conditions, precipitation will seal localized regions of the fracture, while interconnected regions of low-reactivity persist, providing dominant pathways for fluid flow (Jones and Detwiler, 2018; Mountassir et al., 2014). Flow focusing into regions with low-reactivity minerals further localizes reactions to progressively smaller subsets of the domain, reducing the overall reactivity of the fracture (Jones and Detwiler, 2016).

Although precipitation-induced flow-focusing induces a negative feedback between precipitation and fracture reactivity, local precipitation reactions can lead to an increase in the reactive surface area, which enhances precipitation rates (Emmanuel and Berkowitz, 2005; Noiriel et al., 2012). Experimental and numerical studies of precipitation in heterogeneous fractures show that reactive mineral growth occurs both across the fracture aperture, which progressively roughens the surface, and in the fracture-plane, which increases the projected area of the reactive minerals (Jones and Detwiler, 2016, 2018). This feedback between precipitation and reactive surface area is not well-constrained in fractures that contained varied degrees of heterogeneity.

Precipitation-induced reactive surface area enhancement may be limited by the characteristic length-scales of the mineral distribution and fracture aperture. Experimental measurements of mineral abundance in porous and fractured rocks provide qualitative estimates of mineral length-scales up to the cm-scale (Peters, 2009; Ellis and Peters, 2016; Coggan et al., 2013; Major et al., 2018; Espinoza et al., 2018). However, measurements directly aimed at characterizing the distributions of reactive minerals show length-scales on the order of 100 μm (Fauchille et al., 2018), showing that the spatial statistics of rock mineralogy are highly variable and sample dependent. A quantitative understanding of how mineralogy length-scales control the feedback between mineral precipitation, reactive surface area, and local transmissivity, is critical to predicting the response of low-permeability rocks to mineral precipitation.

In this paper we quantify the feedback between mineral precipitation, reactive surface area, and transmissivity in heterogeneous fractures. To do this, we first identify the length-scales that control the feedback between precipitation and reactive surface area through a comparison between a simple semi-analytical solution and simulations in flat-walled fractures with periodically distributed reactive minerals. To quantify the influence that surface area enhancement has on precipitation in fully heterogeneous fractures, we perform additional simulations in fractures that contain three-dimensional surface roughness and varied degrees of mineral heterogeneity. In addition, we examine the role of local kinetics and boundary conditions in determining the fracture-scale response to local precipitation-induced fracture surface alterations. These simulations provide a quantitative measure of the length- and time-scales over which reactive surface area enhancement, or transmissivity reduction, control precipitation-induced fracture alterations.

4.2 Analytical and Numerical Methods

4.2.1 Reactive Transport Modeling

We simulated precipitation in a heterogeneous fracture using the reactive transport model outlined in Jones and Detwiler (2018). This model simulates dissolved ion transport using finite-volume approximations to the quasi-steady-state depth-averaged Stokes and advection-diffusion-reaction equations. The flow and transport calculations are coupled to a three-dimensional surface alteration algorithm that models precipitation onto the fracture surfaces using the level set method. Below we provide a brief description of the governing equations for the reactive transport model and describe the level set approach to modeling local precipitation reactions.

The local fluid flux, q, was calculated by integrating the depth-averaged the Stokes equation across the fracture plane:

$$\nabla \cdot q = 0 \tag{4.1}$$

where q was approximated using the local cubic law:

$$q = \frac{b^3 g}{12\nu} \nabla h \tag{4.2}$$

Here b is the fracture aperture, g is the gravitational constant, ν is the kinematic viscosity, and h is the local hydraulic head. The depth-averaged advection-diffusion-reaction-equation provided quantitative estimates of the local dissolved ion concentration:

$$\nabla \cdot (qc) - \nabla \cdot (Db\nabla c) = R(c) \tag{4.3}$$

where D is the molecular diffusion coefficient, and c is the local depth-averaged dissolved ion concentration. The advective and diffusive flux of dissolved ions through the fracture is balanced by the flux of dissolved ions onto the fracture surface, which is quantified through the local reaction rate, $R(c)$:

$$R(c) = k_{eff}(1 - \frac{c}{c_s}) \tag{4.4}$$

Here c_s is the solubility concentration of the dissolved mineral and k_{eff} is the reaction rate constant which accounts for mass-transfer limitations due to diffusion across the fracture aperture (Detwiler and Rajaram, 2007):

$$k_{eff} = \frac{k}{1 + \frac{2kb}{ShDc_s}} \tag{4.5}$$

In equation (4.5), k is the empirically derived kinetic reaction rate constant and Sh is the Sherwood number. To simulate precipitation-induced surface alterations, we directly converted the local precipitation rates, $R(c)$, to a surface alteration rate:

$$v_n = \frac{R(c)}{\alpha\rho} \tag{4.6}$$

where α is the stoichiometric coefficient that relates the moles of c to moles of the produced mineral, and ρ is the density of the precipitated mineral. Equations (4.1) through (4.6) were solved across a two dimensional computational domain using uniform grid spacing (i.e. $\Delta x = \Delta y$).

We used the level set method to model mineral precipitation onto the fracture surfaces. This method simulates precipitation by advecting each surface in the local unit-normal direction using the surface velocity described by (4.6). This requires defining the elevation of each fracture surface in a three-dimensional domain with unit grid spacing (e.g. $\Delta x = \Delta y = \Delta z$). Allowing the fracture surfaces to change in the local normal direction provides the capacity to track three-dimensional fracture surface due to mineral growth across the fracture aperture and in the fracture-plane (Jones and Detwiler, 2018). In addition to this, the level set method allows us directly quantify changing reactive surface area due to precipitation-induced alterations of the fracture surfaces. For a more detailed discussion of this method, we refer the reader to Jones and Detwiler (2018).

4.2.2 Characteristic evolution of a reactive mineral

To better understand the length- and time-scales that control precipitation in heterogeneous fractures, we developed a simple mechanistic model that describes the geometric alterations of a reactive mineral due to the incorporation of dissolved ions onto the mineral surfaces.

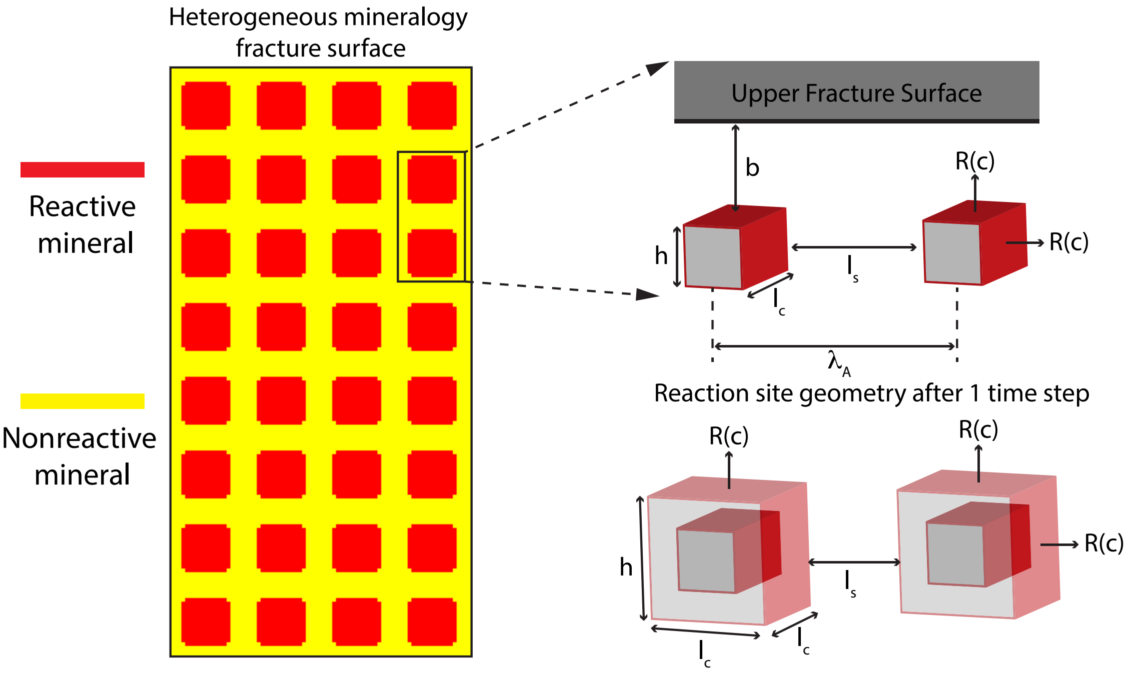

Figure 4.1: Schematic representation of a heterogeneous mineralogy fracture surface with periodically distributed reactive minerals (red) separated by inert minerals (yellow). The zoomed-in region shows the geometric characterization of a reactive mineral as a cuboid with characteristic length, l_c, and characteristic height, h. The mineral distribution has period, λ_A, which is directly related to the separation length, l_s. During the precipitation process, ion incorporation onto the mineral surface, which is quantified by the local precipitation rate, $R(c)$, will cause l_c, h, and l_s, to change over time.

Figure 4.1 shows a schematic representation of a fracture surface that contains heterogeneous surface mineralogy. In this schematic reactive minerals (red) are distributed periodically across the surface and are separated by non-reactive (yellow) minerals. The precipitation rate onto each individual mineral surface is controlled by the local chemical disequilibrium and by the local reactive surface area (Lasaga, 1984). Because precipitation alters the geometry of each reaction site, the reactive surface area will change over time.

To characterize the precipitation-induced mineral alterations, we approximate each mineral on the fracture surface as a cuboid. The characteristic length of the cuboid, l_c, is given by:

$$l_c = \sqrt{A_{proj}} \tag{4.7}$$

where A_{proj} is the projected surface area onto the 2D fracture plane. Based on this calculated characteristic length, the separation length, l_s, can be calculated using:

$$l_s = \lambda_A - lc \tag{4.8}$$

where λ_A is the correlation length of the mineral distribution (see Figure 4.1). These two characteristic length-scales, l_c and l_s, control the surface area of the faces that span across the fracture plane. The characteristic height of each mineral, h, is independent of these length-scales and constrains the surface area of the faces that span across the fracture aperture, b.

Based on this geometric characterization, the corresponding surface area of a single mineral is:

$$A_j = l_{c,j}^2 + 4l_{c,j}h_j \tag{4.9}$$

Here $l_{c,j}^2$ is the surface area of the top face of the reactive mineral, and $4l_{c,j}h_j$ is the surface area around the perimeter of mineral j. When the local reaction kinetics are slow enough that chemical disequilibrium is uniform along the length of the reactive mineral, dissolved minerals will be incorporated onto each face at a uniform rate, $R(c_j)$. As a result, the total mass precipitated onto the j^{th} reactive mineral is:

$$\frac{dm_j}{dt} = R(c_j) * A_j \tag{4.10}$$

where A_j is given by (4.9) and $R(c_j)$ is given by (4.4).

Precipitation onto the surface will increase the reactive surface area over time:

$$\frac{dA_j}{dt} = \frac{d}{dt}(l_{c,j}^2 + 4l_{c,j}h) = 2l_{c,j}\frac{dl_{c,j}}{dt} + 4\frac{dl_{c,j}}{dt}h + 4l_{c,j}\frac{dh_j}{dt} \tag{4.11}$$

Assuming $R(c)$ is uniform across the reactive mineral simplifies (4.11) such that:

$$\frac{dl_c}{dt} = \frac{dh}{dt} = \frac{R(c)}{\alpha\rho} \tag{4.12}$$

In an unbounded domain, mineral j will grow continuously throughout time and maintain self-similar geometric properties. However, the application of this simple mechanistic model to heterogeneous fracture surfaces is complicated by spatial features that limit the growth of a single mineral over time. This growth process is limited by two length scales: (1) the initial fracture aperture, b_o, which limits the vertical extent of mineral j, and (2) the separation length, l_s, between adjacent minerals which limits that lateral extent of mineral j.

When $l_s > b_o$, the reactive mineral will span across the aperture before contacting an adjacent mineral. As a result, the top surface of the cuboid will come into contact with the top fracture surface, and precipitation will be limited to the mineral faces that span across the fracture aperture. Accordingly, the reactive surface area follows the form:

$$\frac{dA_j}{dt} = \begin{cases} \frac{R(c_j)}{\alpha\rho}(2\lambda_{c,j} + 4h + 4\lambda_{c,j}) & h < b \\ \frac{R(c_j)}{\alpha\rho}(4\lambda_{c,j} + 4b_j) & h \geq b \end{cases} \tag{4.13}$$

When $b_o > \lambda_s$, the reactive mineral will be intercepted by adjacent reaction sites, which limits reactions to the mineral surface that spans across fracture plane. In a periodic domain, the mineral surface that spans across the fracture plane will stop growing once the mineral is intercepted by surrounding regions. To account for this case, we adopt a surface area function given by:

$$\frac{dA_j}{dt} = \begin{cases} \frac{R(c_j)}{\alpha\rho}(2\lambda_{c,j} + 4h + 4\lambda_{c,j}) & l_c < \lambda_s \\ 0 & l_c \geq \lambda_s \end{cases} \tag{4.14}$$

Integrating (4.13) and (4.14) in time provides quantitative estimates of precipitation-induced reactive surface area alterations at a single mineral throughout the reactive transport. This approach provides the flexibility for $R(c_j)$ and A_j to vary across the fracture plane which leads to nonuniform surface alterations across the fracture. To calculate the total mass precipitated, m_f, and fracture-scale reactive surface area, A_f, we integrate (4.10), (4.13), and (4.14) throughout time and across the fracture surface:

$$m_f = \oiint_S \int_0^t \frac{dm_j}{dt} dt \tag{4.15}$$

and

$$A_f = \oiint_S \int_0^t \frac{dA_j}{dt} dt \tag{4.16}$$

Figure 4.2 shows the characteristic curves resulting from the integration of (4.10), (4.13), and (4.14). In this simple example, we have assumed that that there are 10 reactive minerals across the surface, that $\frac{c_o}{c_s} = 10$, and that c_j decreases linearly to c_s from the first to last reaction site. For all cases, A_f vs m_f follows the same line until $l_c \geq \lambda_s$ and $h = b_o$. The nonlinear slope when $l_c < \lambda_s$ is due to nonuniform precipitation rates along the length of the fracture that cause A_f and m_f to increase locally at different rates. When mineral growth is limited by λ_s, A_f plateaus to λ_c^2 for $l_c \geq \lambda_s$ because the reactive minerals no longer grow across the fracture plane. However, when b is the limiting length-scale, A_f increases linearly after $h = b_o$ because the reactive mineral continues to grow across the fracture plane.

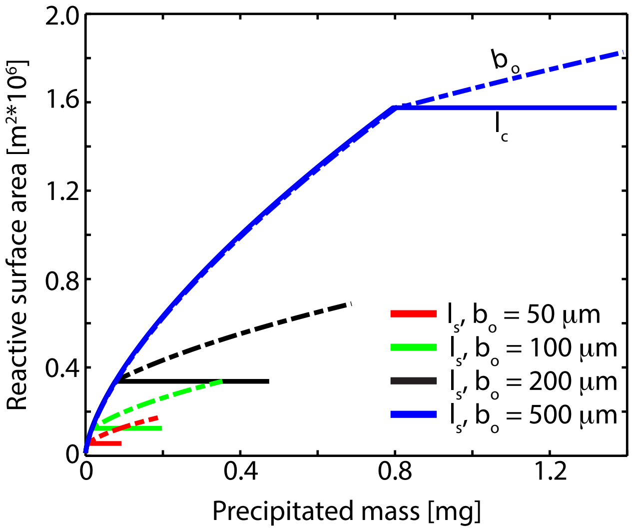

Figure 4.2: Characteristic feedback between mineral precipitation and reactive surface area. The solid lines show the feedback according to (4.14) and the dashed line follows the functional form of (4.13). As the initial separation length or fracture aperture (l_s or b_o) increases, reactive surface area generation increases correspondingly. Under all conditions, reactive surface area generation is limited by l_s.

Applicability regime of analytical model

Equations (4.15) and (4.16) were derived assuming that $R(c)$ is uniform across mineral j. However, this assumption may only be valid under conditions where the concentration does not vary significantly along the length of the mineral. To constrain the applicability of (4.15) and (4.16), we derive a local Damköhler, Da_l, number that describes the relative rates of advection across the length of a reactive mineral and precipitation onto the mineral surface.

Defining a control-volume that encompasses only one of the minerals shown in Figure4.1 allows us to define the following mass flow rates across and onto the mineral surfaces:

$$f_{q,j} = q\bar{c}_j l_{c,j} \tag{4.17}$$

and

$$f_{r,j} = R(\bar{c_j})A_j = k(\bar{c_j} - c_s) \tag{4.18}$$

where (4.17) describes the mass flow rate of dissolved ions across the surface of mineral j due to advection, (4.18) describes the mass flow rate onto the mineral surface due to precipitation. In these expressions, $\bar{q_j}$ and $\bar{c_j}$ are the average flux and concentration across the mineral surface,respectively. The time scales, τ_q and τ_r, that correspond with the removal of one mole from the control volume is given by $\frac{1}{f_{q,j}}$ and $\frac{1}{f_{r,j}}$. Therefore, Da_l can be defined as the relative timescales for advection across and precipitation onto the mineral:

$$Da_l = \frac{\tau_q}{\tau_r} = \frac{kA_j(\bar{c} - c_s)}{\bar{q}\bar{c}l_c} \tag{4.19}$$

For $Da_l \geq 1$, all dissolved ions will be precipitated out of solution during flow across a single reactive mineral. As a result, precipitation rates will be fastest at the leading edge of the reaction site and decrease along the length of the mineral, leading to non-uniform geometric alterations that may not be well-represented using the analytical approach described in (4.16). However, when $Da << 1$, precipitation will occur over much longer time-scales that the advective flux of dissolved ions across the mineral, which leads to a uniform concentration along the length of the mineral. Under these conditions, (4.16) should represent the growth dynamics well. In Section 4.3 we examine the applicability of (4.15) and (4.16), and use the analytical solution to quantitatively constrain the length-scales that control the feedback between precipitation and reactive surface area.

4.3 Feedback between precipitation and reactive surface area

We ran a series of parametric simulations in flat-walled fractures using the model described in Section 4.2.1 to quantify the feedback between precipitation and reactive surface area. We systematically vary the reaction kinetics, relative magnitude of advection and diffusion, and the characteristic length-scale of the reaction sites. Below we describe the conditions used in each simulation and provide a quantitative comparison between simulation results and the feedback predictions using (4.15) and (4.16).

4.3.1 The influence of reaction and transport conditions

Figure 4.3A shows the initial mineral distribution used in the parametric simulations. In this fracture, reactive (red) minerals were distributed periodically across the domain and covered 35% of the bottom fracture surface. The reactive minerals were equally spaced at $l_s = 6\Delta x$ and contained characteristic lengths, l_c, of $10\Delta x$. Each simulation was run until precipitation reduced fracture transmissivity, $T = \frac{\bar{q}}{\nabla h}$, by one order-of-magnitude.

A supersaturated fluid ($c_o = 10{*}c_s$) was injected into the fracture at a constant flow rate from left to right. Local chemical disequilibrium induced precipitation at nodes that contain reactive minerals, which caused $CaCO_3$ reaction sites to grow across the fracture aperture and in the fracture plane. This is illustrated in the cross-section A-A' shown in Figure 4.3B. In this frame, the initial mineral is shown in grey, and the advancement of the minerals across the fracture aperture and fracture plane is shown using the colormap that indicates mineral age (in terms of simulation time steps). These age maps show that initially separate reactive minerals grow vertically and laterally, until they eventually merge and transition to a smoother surface over time.

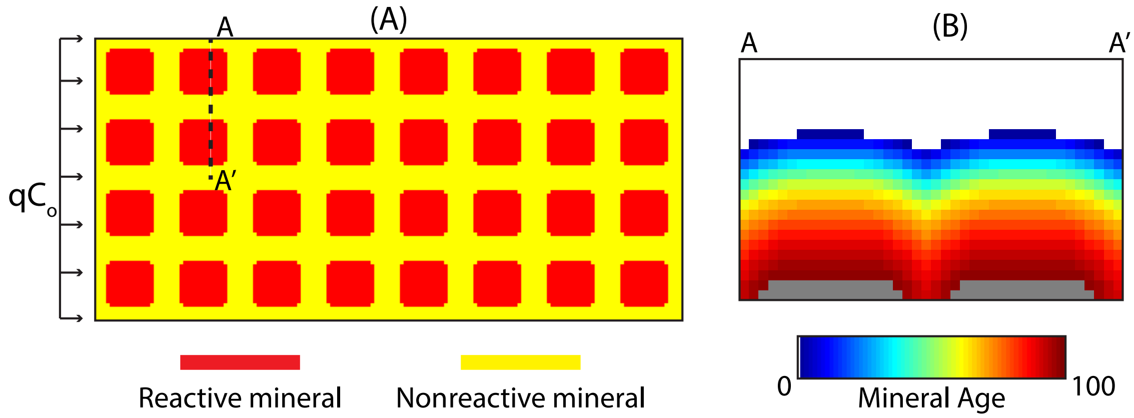

Figure 4.3: (A) Initial condition for parametric simulations. Reactive minerals (red) are periodically distributed across the fracture surface. (B) Characteristic evolution of minerals on the A-A' cross-section. The mineral age (in terms of simulation time steps) shows that minerals grow vertically across the fracture aperture and laterally across the fracture plane.

To explore the role of reaction kinetics and fluid transport on the feedback between precipitation and reactive surface area, we varied the reactive transport conditions by changing the fracture-scale Peclét (Pe) and Damköhler (Da) numbers between simulations. Here, we define Pe and Da as:

$$Pe = \frac{\bar{q}}{D} \qquad \& \qquad Da = \frac{kL}{\bar{q}} \tag{4.20}$$

where $\bar{q}$ is the fluid flux across the fracture, L is the length of the fracture, and k and D are the reaction rate constant and molecular diffusion coefficient, respectively. These dimensionless parameters provide a measure of the relative roles of advection, diffusion, and reaction kinetics throughout the precipitation process. For $Pe >> 1$, advection is the dominant transport mechanisms across the fracture plane. For $Da > 1$, reaction kinetics are fast enough that dissolved ions are depleted along the length of the fracture, leading large concentration gradients in the mean flow direction. We note that this definition of Pe and Da defines fracture-scale processes, such as the development of concentration gradients along the length of the fracture, and does not describe the local conditions that are constrained by (4.19). We vary Pe between 0.0625 and 62.5 to quantify precipitation under diffusion- and advection-dominated regimes, and vary Da between 2.56 and 2560 to quantify the precipitation process under fast and slow kinetic conditions.

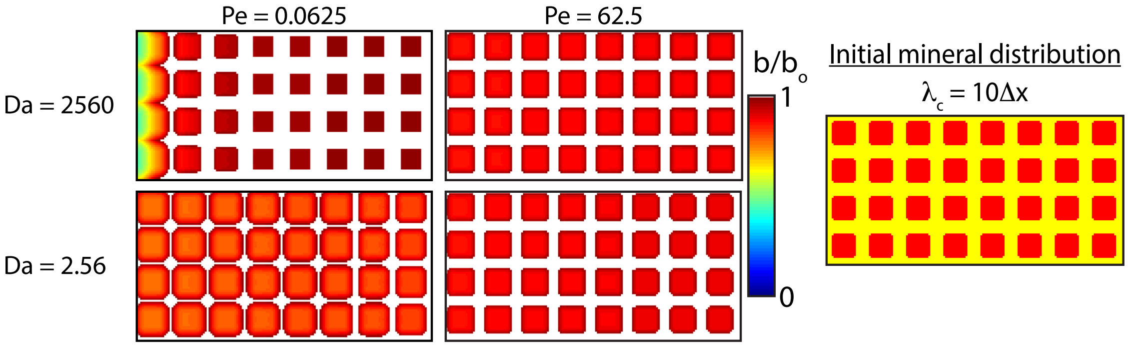

Figure 4.4: Normalized aperture fields (b/b_o) for Da = 2560 and 2.56, and Pe = 0.0625 and 62.5 after 0.3 mg of mass had precipitated onto the fracture surface. At larger Da, precipitation remained focused towards the fracture inlet. At lower Da and higher Pe, reactions are distributed more uniformly across the fracture surface.

Figure 4.4 shows normalized aperture fields (b/b_o) for a subset of the parametric simulations after 0.3 mg of mass had precipitated onto the fracture surface. For $Da = 2560$, precipitation rates were fastest at the fracture inlet and $b/b_o \sim 0.9$ at the fracture outlet. Alternatively, for $Da = 2.56$, precipitation kinetics were slow enough that reactions were more uniformly distributed across the fracture surface, leading to wide-spread $b/b_o < 1$ values across the domain. When Pe increased from 0.0625 to 62.5, local precipitation became limited by mass-transfer across the fracture aperture, and k_{eff} reduced by two orders-of-magnitude. The decrease in precipitation rate caused uniform precipitation throughout the fracture.

The local flow, transport, and kinetic conditions play an important role in the geometric evolution of the individual reaction sites. This is most notable at low Pe. For the Da = 2560 simulation, $Da_l = 185$ which suggests that precipitation will occur non-uniformly across the length of a single mineral. The b/b_o fields are in good agreement with this, showing that mineral precipitation at the inlet created a band of $b/b_o < 0.5$ that spanned the entire width of the fracture, however, at the trailing edge of the first row of reaction sites, $b/b_o \sim 0.9$.

Alternatively, for the $Da = 2.56$, $Da_l < 0.2$; under these local conditions, the b/b_o fields show that precipitation led to a uniform geometric evolution of the individual reaction sites.

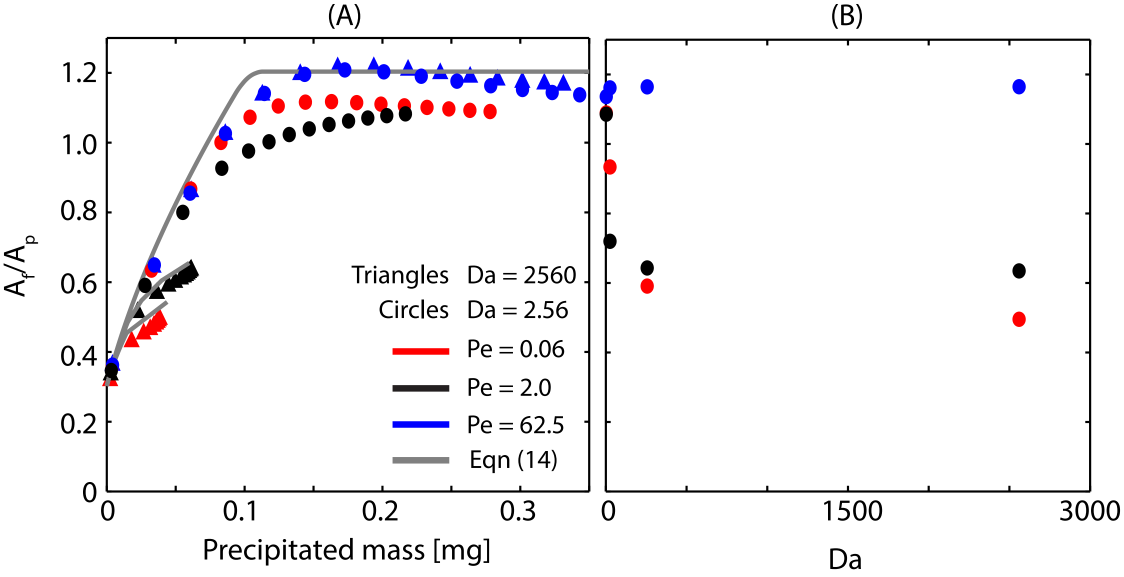

Figure 4.5: (A) Reactive surface area, A_f, normalized by the area of the fracture plane A_p, plotted against the total precipitated mass for a wide range of Pe and Da numbers. Total precipitated mass and reactive surface area predicted with (4.15) and (4.16) is shown with the grey lines. Reactive surface area enhancement is largest at small Da and large Pe. (B) total reactive surface area after precipitation has reduced fracture transmissivity by one order-of-magnitude. Results show that the total precipitated mass is most sensitive to Da.

Geometric alterations at the local scale affect the feedback between precipitation and reactive surface area at the fracture-scale. Figure 4.5 plots the fracture scale surface area, A_f, normalized by the area of the fracture plane, $A_p = n_x * n_y * \Delta x^2$, versus the total mass precipitated onto the fracture surface. The simulation results are shown for $Da = 2560$ (triangles) and 2.56 (circles) at $Pe = 0.06$ (red), 2.0 (black), and 62.5 (blue). To quantify the characteristic length-scales that control the surface evolution, we compare the simulation results to predictions using (4.16) and (4.15) (grey lines); for simplicity we only present the analytical solution for $Da = 2560$ case. For these simulations, the fracture-aperture is large enough that $l_s < b_o$; therefore A_j follows the form of (4.14).

Uniform surface alterations at $Pe = 62.5$ caused A_f to increase at the same rate across Da conditions. At the onset of the reactive transport, growth of the individual reaction sites led to a rapid increase in A_f. As the reactive transport progressed, the slope decreased until A_f eventually plateaued to $A_f/A_p \sim 1.15$. At $Pe = 0.06$ and $Da = 2.56$, the slope changed rapidly because precipitation remained focused towards the fracture inlet, which limited the total precipitated mass at the time of fracture sealing. The good agreement between simulation results and (4.16) provides two key insights: (1) Da_l may only loosely constrain the geometric characterization as a cubic rectangle, and (2) that the gradual transition to constant A_f is caused by interception of individual reaction sites to form larger conglomerates.

Figure 4.5B plots the total reactive surface area at the time of fracture sealing and provides a measure of the sensitivity of feedback between precipitation and reactive surface area to different kinetic and transport conditions. At intermediate and low Pe (e.g. $Pe = 0.06$ and 2.0), the feedback is very sensitive to the local kinetic conditions; under both Pe conditions, A_f decreased by over 50% between $Da = 2.56$ and 2560. At larger Pe, the total reactive surface area is not sensitive to Da because the local rate is controlled by diffusion of dissolved minerals across the fracture.

4.3.2 Influence of l_c

The results from Section 4.3.1 indicate that geometric alterations at the local scale control the feedback between precipitation and reactive surface area at the fracture scale. Changes to the local surface geometry are controlled by the rate of precipitation onto the mineral surface and the rate of dissolved ion transport across the surface; therefore, as the characteristic length-scale, l_c, of the reactive minerals change, local alterations may change accordingly.

To quantify the impact of l_c on the feedback between precipitation and reactive surface area, we ran additional simulations under the same reactive transport conditions described in Section 4.3.1. In these simulation, we reduced l_c by a factor of 2 while keeping the initial surface area similar (7% larger than the field shown in Figure 4.3). Because the size of the computational domain was held constant between different l_c simulations, changing the characteristic length of the reactive minerals caused l_s to reduce from $6\Delta x$ to $4\Delta x$.

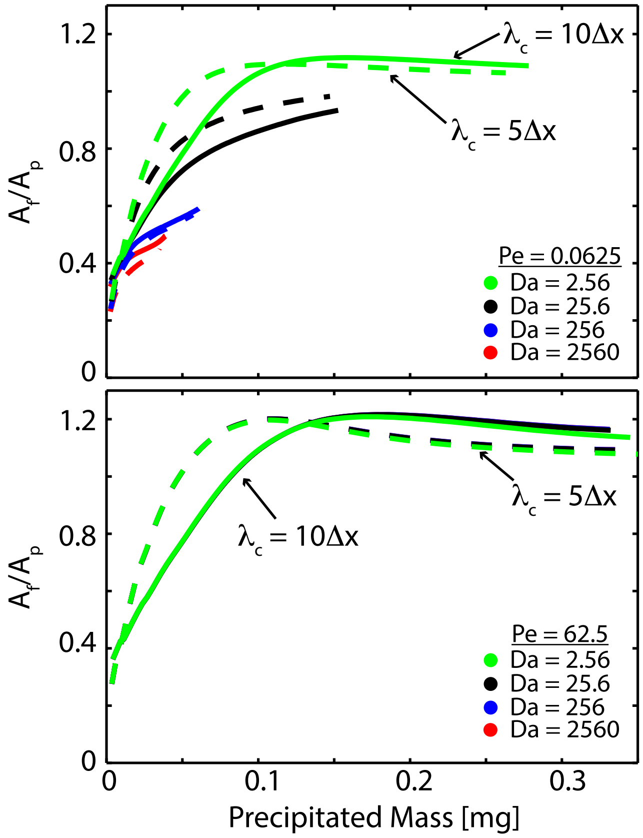

Figure 4.6: Normalized reactive surface area generation, A_f/A_p, versus precipitated mass over a wide range of Da numbers and $Pe = 0.0625$ (upper frame) and 62.5 (lower frame). $l_c = 10\Delta x$ simulations are shown with solid lines, and $l_c = 5\Delta x$ simulations are shown with dashed lines. Results show that decreasing l_c reduces Da_l and induces more rapid generation of reactive surface area.

Decreasing l_c led to a corresponding reduction in Da_l across simulations. Figure 4.6 provides a direct comparison between Da_l states identical fracture-scale Pe and Da conditions. For $Pe = 0.0625$ and $Da = 2.56$, the average Da_l was 0.19 and 0.07 for the $\lambda_c = 10\Delta x$ and $5\Delta x$ simulations, respectively. This reduction in Da_l corresponded to approximately twice the rate of increase in A_f when $l_c < l_s$, and also caused the interception timescale to decrease by a factor of 2. For simulations in which the mean $Da_l >> 1$, the slope of A_f was not significantly impacted by decreasing l_c.

4.3.3 Aperture dependence

The good agreement between the simulation results presented in 4.3.1 and (4.14) show that merging, or interception, of reactive minerals plays an important role in the evolution of fracture-scale reactive surface area. In addition to merging, reaction site geometry is limited by the local fracture-aperture. To examine the role of aperture on the feedback between precipitation and reactive surface area, we perform additional simulations under the same initial conditions described in Section 4.3.1, but with initial fracture apertures of 50, 100, and 150 μm. In these simulations, $Pe = 0.0625$ and $Da = 2.56$.

Figure 4.7A shows that the feedback between precipitation and reactive surface produces self-similar curves when the aperture is varied. When $b_o = 50$ μm, A_f increased by only 20% and for $b_o = 150\mu$m, A_f increase by ~70%. The good agreement between the simulated feedback and the predicted feedback using (4.13) (black lines in Figure 4.7) indicates that the gradual decrease in slope is due to reaction sites spanning the fracture aperture. After a reactive minerals span the aperture, A_f increases linearly with λ_c (e.g. see (4.13)). Accordingly, figure 4.7B shows that A_f increases linearly with b.

4.4 Mineral precipitation in heterogeneous fractures

The results presented in Section 4.3 demonstrate that the feedback between precipitation and reactive surface area is sensitive to Da and λ. In natural fractures, the positive feedback between precipitation and surface area is countered by the negative feedback between precipitation and local transmissivity, which alters the local flux of dissolved ions, and thus the local precipitation rate, over time. To quantify the competition between these two feedbacks during precipitation in a heterogeneous fracture, we performed a series of reactive transport simulations under constant flow boundary conditions at $Pe = 44$ and $Da = 1.7$ ($k = 10^{-6.86}$

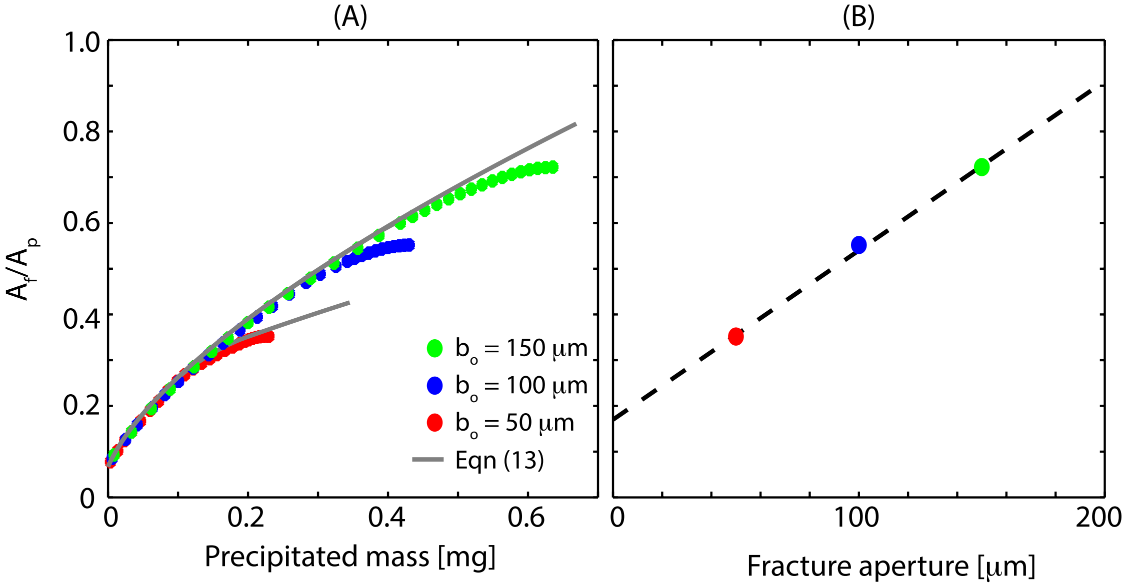

Figure 4.7: (A) Normalized reactive surface area generation, A_f/A_p, versus precipitated mass for $Pe = 0.0625$ and $Da = 2.56$. Predictions based on (4.13) shown in grey. (B) Total reactive surface area (dots) increases linearly as b increases.

mol $\cdot$ m$^{-2}\cdot$ s^{-1}) and 0.02 ($k = 10^{-8.7}$ mol $\cdot$ m$^{-2}\cdot$ s^{-1}) using the reactive transport model described in Section 4.2.1. Due to the computational demands of the level-set method, we perform simulations on a 0.5 x 1.0 cm computation domain with uniform grid spacing of 10 μm. Flow and transport is solved across the 2D fracture plane and the level set surface alteration method is computed on a 3D domain that encompasses the fracture surfaces and bounding matrix. To limit boundary effects in the small computational domain, we apply periodic boundary conditions on the boundaries parallel to the mean flow direction.

Figure 4.8 shows initial conditions for the heterogeneous fracture simulations. Both the fracture aperture and mineral distributions were generated using a Gaussian distribution with the following power spectrum:

$$G_{b,A}(\kappa) \propto \frac{1}{(1+\lambda_{b,A}^2\kappa^2)^{1+H}} \tag{4.21}$$

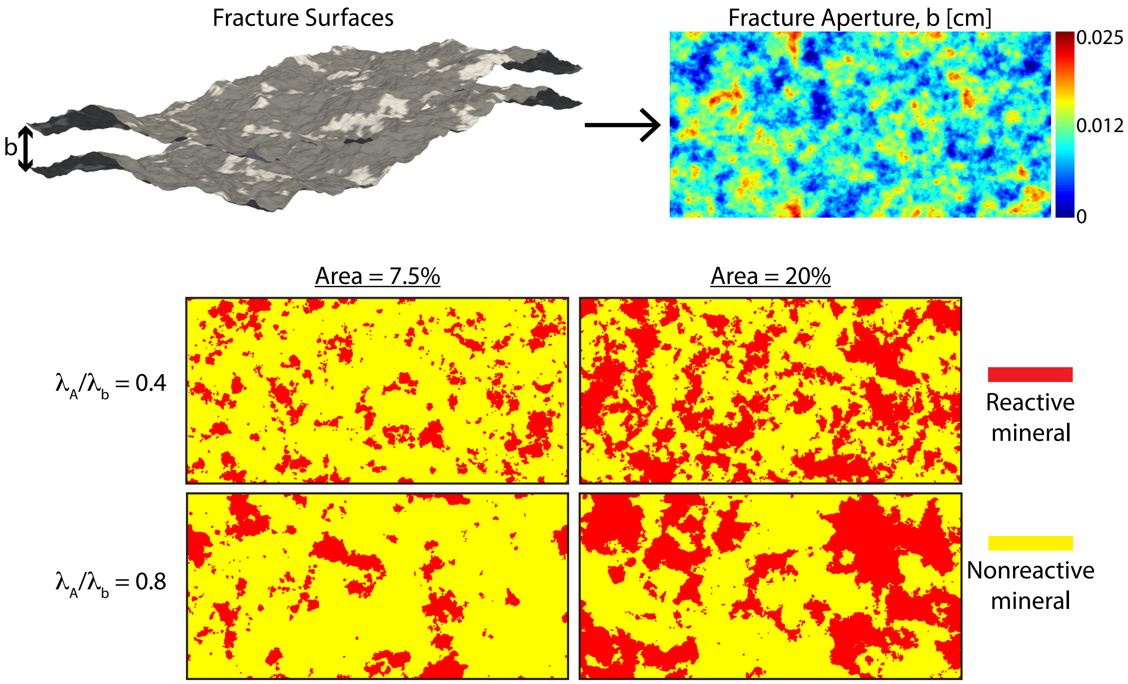

Figure 4.8: Initial conditions for heterogeneous fracture simulations. In these simulations, fracture surfaces contain three-dimensional surface roughness and mineral heterogeneity. The fracture aperture distribution, b, is kept constant between simulations. The mineral distributions projected onto the fracture plane are shown in the bottom frames.

Here κ is the wavenumber vector, H is the Hurst roughness exponent, and λ_b and λ_A are the cutoff length-scales for the roughness and mineral distributions, respectively. Multiplying the Gaussian distribution by the power spectrum in the frequency domain, and then taking the real components of the inverted field, results in a 2D array of apertures, or mineral phases, that contain the specified λ, mean (μ_b), and standard deviation (σ_b). Both the fracture surface roughness and random mineral distributions were generated using $H = 0.8$ (Brown, 1995).

We kept the initial fracture surface geometry constant between simulations. The initial surface roughness was generated using $\lambda_b = 100\Delta\text{x}$. On the 500 x 1000 grid used for the simulations, this corresponds to a correlation length that is $1/5^{\text{th}}$ and $1/10^{\text{th}}$ of the fracture width and length, respectively. The top frame of Figure 4.8 shows a schematic representation of the fracture surfaces generated prior to the reactive transport simulations. The fracture aperture field, b, which is shown to the right of the schematic, had a mean of 160 μm and standard deviation 50 μm.

To accommodate the varying degrees of mineral heterogeneity observed in fractured rocks, we examined the effects of both initial mineral abundance, $A_{f,o}/A_p$, and mineral spatial distribution on precipitation. To do this, we generated random distributions using (4.21) for both the upper and lower fracture surface and binarized the fields by choosing a threshold that omitted values greater than a fixed percentage of the prescribed standard deviation. We considered two initial mineral abundances: (1) $A_{f,o}/A_p = 7.5\%$ and (2) $A_{f,o}/A_p = 20\%$. To assess the impacts of the spatial distribution of reactive minerals, we vary λ_A for (1) and (2) such that $\lambda^* = \lambda_A/\lambda_b = 0.4$, and 0.8. For $A_{f,o}/A_p = 7.5\%$ and $A_{f,o}/A_p = 20\%$ we chose threshold values of $0.85\sigma_b$ and $1.45\sigma_b$, respectively. Figure 4.8 shows the resulting mineral distributions superimposed and projected onto the fracture plane. For $\lambda^* = 0.4$, the reactive minerals are smaller and more uniformly distributed across each surface, while for $\lambda^* = 0.8$, the reactive minerals form fewer, but larger patches of fracture surface.

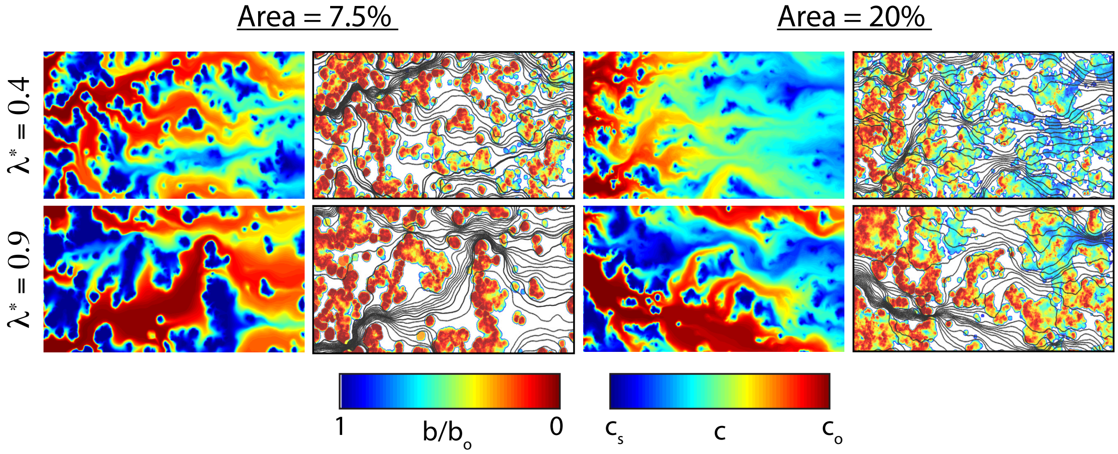

Figure 4.9: Steady-state concentration fields, c, and normalized aperture fields, b/b_o, superimposed with simulated streamlines for the $Da = 1.7$ simulations after precipitation had reduced fracture transmissivity by one order-of-magnitude. Simulated streamlines show that precipitation enhanced preferential flow in all simulations, and c fields show that increasing λ^* focused larger solute fluxes into regions of limited reactive surface area.

Figure 4.9 shows the steady-state concentration fields, c, and normalized aperture fields, b/b_o, superimposed with the simulated streamlines for the $Da = 1.7$ simulations after precipitation had reduced fracture transmissivity by one order-of-magnitude. In these frames, $b/b_o < 1$ indicates regions where precipitation reduced fracture aperture, and $b/b_o = 1$ indicates regions where the fracture surfaces were unaltered. The simulated streamlines provide a quantitative measure of fracture tortuosity, τ, by normalizing the average path-length of the streamlines by the fracture length.

The b/b_o fields in Figure 4.9 show that precipitation reactions persist nearly the entire length of the fracture when $A_{f,o}/A_p = 7.5\%$. In both fields, precipitation at the inlet focused flow into a thin preferential flow path and increased τ from 1.03 to 1.40 and 1.37 for $\lambda^* = 0.4$ and 0.8, respectively. For $\lambda^* = 0.8$, the larger interconnected regions void of reactive minerals resulted in a larger flow path that carried $c = c_o$ deeper into the fracture compared to $\lambda^* = 0.4$. For the $Da = 0.02$ simulations (not shown), the relatively slow reaction kinetics led to uniform precipitation across the fracture that focused flow into a single flow path for both λ^* simulations. These flow alterations corresponded to a 38% and 36% increase in τ for $\lambda^* = 0.4$ and 0.8, respectively.

When $A_{f,o}/A_p = 20\%$, precipitation remained more focused towards the fracture inlet, and the c distributions show more pronounced differences between λ^* fields. At $\lambda^* = 0.8$, the b/b_o field shows that fast precipitation at the inlet focused flow into a small portion of the fracture void of reactive minerals. Approximately 1/3rd the length of the fracture, this preferential flow path expanded and flow became more uniformly distributed across the domain; this corresponded to a 25% increase in τ. At lower λ^*, precipitation reduced the aperture across the majority of the fracture inlet and flow occurred more uniformly across the domain; as a result, c remained relatively uniform across the width of the fracture. For the $Da = 0.02$ simulations, precipitation-induced aperture sealing perturbed flow to the largest extent for the $\lambda^* = 0.4$ simulation, where τ increased by approximately 50%. For all simulations, flow-focusing in the $\lambda^* = 0.8$ fractures led to larger variations in c across the fracture width when compared to the $\lambda^* = 0.4$ simulations.

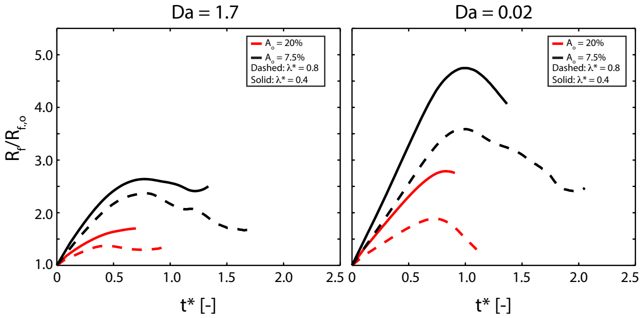

Figure 4.10: Fracture-scale precipitation rate, R_f, versus time for all $A_{f,o}/A_p$ and λ^* simulations at $Da = 1.7$ and 0.02. Results show that R_f increases over time, however the slope of R_f decreases over time for all simulations. Prior to sealing, R_f decreases for all simulations except for the $A_{f,o}/A_p = 20\%$ and $\lambda^* = 0.4$ simulation at $Da = 1.7$.

To quantify the evolution of the precipitation process, we computed the fracture-scale precipitation rate, R_f:

$$R_f = \sum_{i=1}^{i=nx} (qc)_{in} - \sum_{i=1}^{i=nx} (qc)_{out} \tag{4.22}$$

which provides a direct measure of how the reactive transport evolves due to the feedback between precipitation, reactive surface area, and local transmissivity. Figure 4.10 shows R_f normalized by the initial rate, R_o, versus time, where the simulation time has been normalized by the sealing timescale, τ_f:

$$\tau_f = \bar{b}\left(\frac{R_{f,o}}{\alpha\rho A_{f,o}}\right)^{-1} \tag{4.23}$$

For all simulations, Figure 4.10 shows that R_f increased throughout the precipitation process. This increase was largest in the $A_{f,o}/A_p = 7.5\%$ and $\lambda^* = 0.4$ fractures, where R_f increased by 4x and 2.5x the initial rate for $Da = 0.02$ and 1.7, respectively. Figure 4.10 also shows that precipitation rate enhancement decreased with increasing λ^*. This is most notable for the $A_{f,o}/A_p = 20\%$ fractures; for $Da = 1.7$, the spatial distribution of reactive minerals led to a 22% difference in the final precipitation rate, and for $Da = 0.02$, the final precipitation rate for the $\lambda^* = 0.4$ fracture was 2x larger than that of the $\lambda^* = 0.8$ fracture.

Despite the overall increase in R_f throughout the precipitation process, the profiles in Figure 4.10 show that rate of change in R_f decreased over time. In addition, for almost all the simulations, R_f decreased prior to fracture sealing. For both Da simulations, this is most notable for the $A_{f,o}/A_p = 7.5\%$ and $\lambda^* = 0.8$ fractures; in these fractures, R_f decreased by 26% and 38% from the max precipitation rate prior to fracture sealing for $Da = 1.7$ and 0.02, respectively. Because the rate of R_f increase progressively slowed throughout the reactive transport, fracture-transmissivity remained preserved over longer time-scales than expected if R_f was assumed constant throughout the precipitation process. This discrepancy was largest in the $A_{f,o}/A_p = 7.5\%$ and $\lambda^* = 0.8$ fracture when $Da = 0.02$, where sealing took twice as long as the prediction based on τ_f.

The decreasing rate-of-change of R_f may be caused by two different mechanisms: (1) decreasing rate of A_f increase as reactive minerals merge or seal the local aperture (see Section 4.3.1), or (2) focusing of reactive fluids into regions of decreasing surface area. To assess whether (1) is controlling the rate of change of R_f in Figure 4.10, we calculated the fracture-scale reactive surface area, A_f, by integrating the level-set functions across the computation domain (see Jones and Detwiler, 2018), and plotted the measurements versus normalized time (Figure 4.11). When calculating A_f, we removed the reactive surface area in grids that are locally sealed (e.g. $b = 0$).

Figure 4.11 shows that surface area is enhanced to the largest extent at low λ^* and that A_f increases linearly with time early in the precipitation process. At late time, precipitation-induced surface area enhancement is strongly influenced by Da. At $Da = 1.7$ and $A_{f,o}/A_p$

= 20%, surface area continued to increase linearly until the fracture has sealed. However, at lower initial mineral abundance, A_f increased at a slower rate after $t^* = 1.0$ until fracture sealing. Alternatively, the late-time evolution of A_f for the $Da = 0.02$ simulations shows that A_f remained constant after $t^* = 1.0$ for all simulations. Because the fracture-scale precipitation rate is linearly dependent on reactive surface area (e.g., Lasaga, 1984), the effective retardation in precipitation-induced surface area generation caused R_f to slow throughout the precipitation process. However, the markedly different trend in A_f compared to the temporal evolution of R_f for $Da = 0.02$ suggests that the reduction in precipitation rate after $t^* = 1.0$ is not only controlled by the decrease in surface area production.

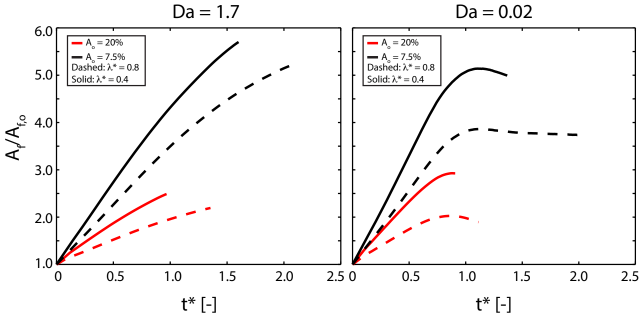

Figure 4.11: Normalized fracture-scale reactive surface area, $A_f/A_{f,o}$, for all simulations. At $Da = 1.7$, A_f increases ∼linearly throughout the precipitation process. However, at $Da = 0.02$, A_f increases linearly until $t^* = 0.5$, and then remains constant for the remainder of the reactive transport.

The c and A_f measurements from the reactive transport simulations provide the capacity to quantify the spatial distribution of precipitation rates throughout the reactive transport. Figure 4.12 shows the distribution of local precipitation rates, $R(c)$, normalized by the max initial precipitation rate, $\max(R_o)$, superimposed with the simulated streamlines for the two limiting simulations: (i) $A_{f,o}/A_p = 20\%$ and $\lambda^* = 0.8$ for $Da = 1.7$, and (ii) $A_{f,o}/A_p = 7.5\%$ and $\lambda^* = 0.4$ for $Da = 0.02$. At early time for both simulations, the $R(c)$ fields show that flow occurred uniformly across the fracture which led to a relatively uniform distribution of precipitation rates across the domain. For $Da = 1.71$, precipitation rates were largest at the fracture inlet, and for $Da = 0.02$, these fast rates persist nearly the entire length of the fracture.

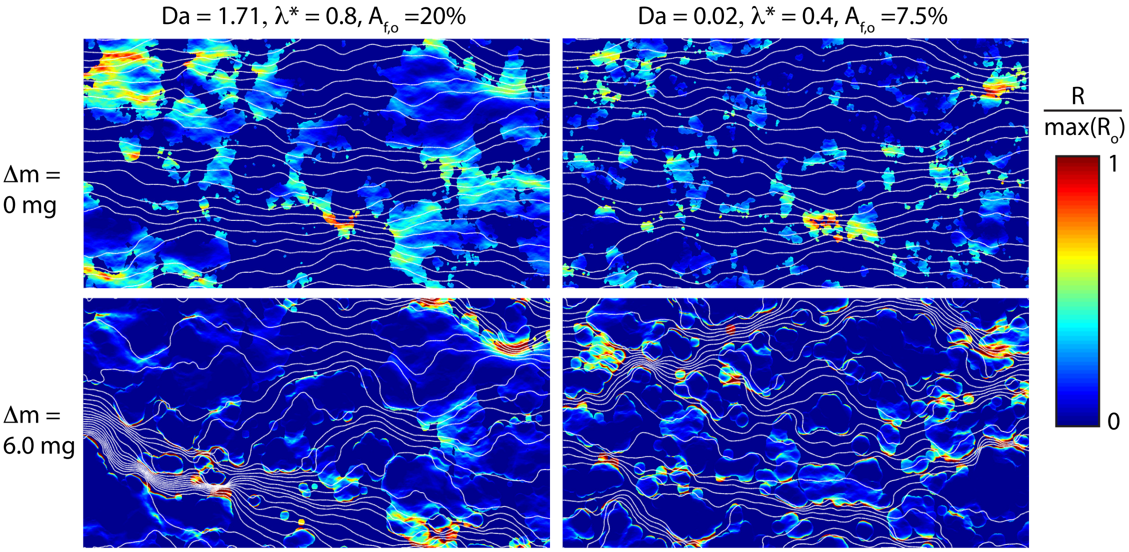

Figure 4.12: Spatial distribution of precipitation rates, $R(c)$, (i) for $\lambda^* = 0.8$ and $A_{f,o} = 20\%$, $\lambda^* = 0.8$, and $Da = 1.7$ and (ii) $A_{f,o} = 7.5\%$, $\lambda^* = 0.4$, and $Da = 0.02$. The results are shown at the onset of the reactive transport ($\Delta m = 0$ mg) and 6.0 mg of mass had precipitated onto the fracture surface.

At later time, the streamlines superimposed on the $R(c)$ fields show that precipitation-induced flow-focusing perturbed the distribution of precipitation rates. For the $Da = 1.7$ simulation, flow was focused into an interconnected region of low-mineral abundance near the inlet. As a result, precipitation rates were fastest at the reactive minerals that bordered the flow path. At the fracture outlet, $R(c)$ increased in localized regions of fast-flow, which indicates that the reaction front extended deeper into the fracture over time. Far from the preferential flow path, $R(c) \sim 0$, even in regions where $b > 0$, which indicates that precipitation became limited by the local advective flux of dissolved ions.

Precipitation-induced aperture reduction in the $Da = 0.02$ simulation focused flow into multiple thin flow paths that extended the length of the fracture. Similar to the $Da = 1.7$ simulation, Figure 4.12 shows that precipitation rates were fastest along the periphery of the reactive minerals that bordered that preferential flow paths. However, because precipitation sealed large portions of the fracture when $Da = 0.02$, relatively fast rates occurred along the entire width of the fracture. Towards the center of each reaction site, $R(c) \sim 0$ because $b \sim$

0 at these location.

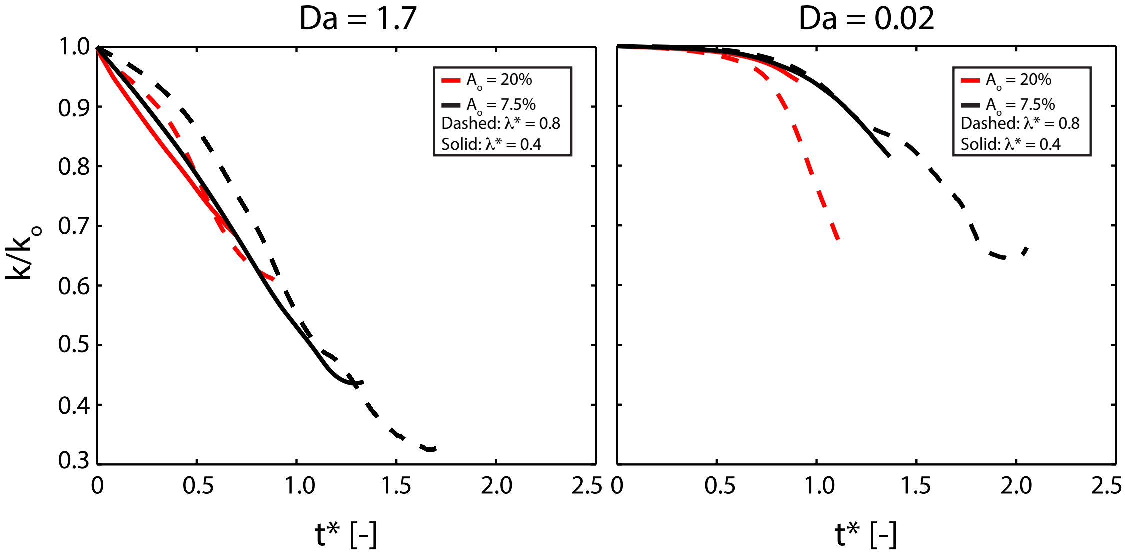

Figure 4.13: Normalized effective rate constant, k, calculated using (4.24). At $Da = 1.7$, k decreased monotonically throughout the reactive transport. At $Da = 0.02$, k was approximately constant for $t^* < 0.5$, and then decreased prior to sealing. k reduction was largest at $\lambda^* = 0.8$.

To quantify the impact of the progressive localization of precipitation reactions on R_f, we plotted the effective rate constant k:

$$k = \frac{R_f}{A_f(\frac{c_o}{c_s} - 1)} \tag{4.24}$$

versus normalized simulation time (Figure 4.13). Normalizing R_f with the time-dependent reactive surface area, A_f, removes the dependence of k on precipitation-induced reactive surface area enhancement and provides a direct measure of how flow-focusing affects the fracture-scale rate constant.

Figure 4.13 shows that the feedback between precipitation and transmissivity led to a reduction in k for all simulations. For $Da = 1.7$, flow-focusing caused an immediate reduction in the effective rate constant. For both initial mineral abundances, k reduces to the largest extent for the $\lambda^* = 0.8$ fields (~40% and 70% reduction for $A_{f,o}/A_p = 20\%$ and 7.5%, respectively). This reduction in k prolonged the sealing time for the $A_{f,o}/A_p = 7.5\%$ simulation by over 50% what was expected based on τ_f.

For $Da = 0.02$, the profiles in Figure 4.13 show that k evolved more dynamically throughout the reactive transport. At the onset of the precipitation process, k remained constant until $t^* \sim 0.5$, which indicates that the reactive transport was controlled by the feedback between precipitation and reactive surface area. This is in good agreement with the rapid increase in R_f for the $Da = 0.02$ simulations shown in Figure 4.10. However, at later time, flow focusing into well-defined flow paths caused k to decrease for all simulations. Because A_f remained constant after $t^* \sim 1$ in the $Da = 0.02$ simulations, this reduction in k led to the reduction in R_f shown in Figure 4.10. Similar to the $Da = 1.7$ simulations, the largest reduction in k occurred in the $\lambda^* = 0.8$ simulations.

4.4.1 Effect of boundary conditions

Laboratory experiments that constrain feedbacks between reactions, surface area, and local transmissivity often rely on constant flow boundary conditions that provide reproducible flow and transport conditions (Noiriel et al., 2012; Elkhoury et al., 2015; Jones and Detwiler, 2016). However, reactive transport processes in natural and engineered environments may also be driven by a constant head gradient, which can lead to changes in the relative rates of advection, diffusion, and reactions as reactive alterations change fracture transmissivity. To quantify the effect that constant heady boundary conditions have on the feedback between precipitation, transmissivity, and reactive surface area, we performed an additional simulation using the $A_{f,o}/A_p = 20\%$ and $\lambda^* = 0.8$ fracture at $Da = 1.7$. In this simulation, we used the same initial conditions from Section 4.4, but changed the inlet boundary conditions from constant flow to constant head.

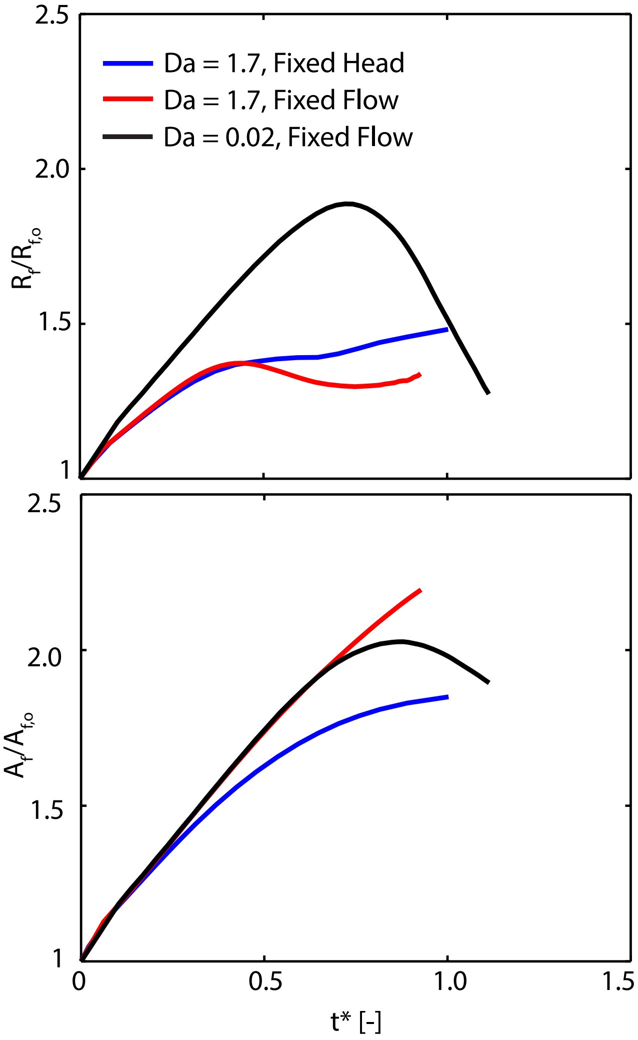

Figure 4.14: Normalized precipitation rate, $R_f/R_{f,o}$, and reactive surface area, $A_f/A_{f,o}$, plotted against time for constant head ($Da = 1.7$ (blue)) and constant flow boundary conditions ($Da = 1.7$ (red) and 0.02 (black)). Early-time rate enhancement for the constant head simulation follows the constant flow boundary conditions despite a lesser increase in A_f. At later time, R_f increased under the constant head conditions, eventually surpassing the precipitation rate produced under lower Da conditions.

Figure 4.14 shows R_f and A_f for both boundary and Da conditions. Early in the precipitation process ($t^* < 0.5$), R_f follows the same trend regardless of the inlet boundary conditions. However, the A_f profile shows that precipitation increased reactive surface area to a lesser extent under constant head boundary conditions due to a decreasing mass flux into the fracture as transmissivity was reduced. At later time, $t^* > 0.5$, R_f continues to increase under the constant head conditions, while R_f decreases under constant flow conditions.

This is particularly interesting because the slope of A_f continues to decrease under constant head conditions, which should lead to a corresponding reduction in in the slope of R_f.

The contrast between rate evolutions at late time indicate that local velocity plays an important role in the fracture-scale response to precipitation. Under constant flow boundary conditions, local aperture sealing increased the velocity through preferential flow paths that contained limited reactive surface area. These enhanced velocity variations localized precipitation reactions to a small sub-set of the domain, which led to a reduction in the effective rate constant throughout the reactive transport.

Under constant head boundary conditions, the local velocity decreased because transmissivity reduction led to slower flow-rates through the fracture over time. At early-time k decreased similarly to the constant flow boundary condition simulations. However, as flow into the fracture reduced, and the reactive transport transitioned to diffusion-dominated transport conditions, k/k_o reached a constant value of 0.8. As the surface area profile in Figure 4.14 shows, the constant k and increasing A_f led to an increase in R_f at late time.

4.5 Concluding Remarks

We have presented simulation results that quantify the role of reactive surface area generation and local transmissivity reduction due to mineral precipitation in a heterogeneous fracture. Results from these simulations show that the positive feedback between precipitation and reactive surface area increased the fracture-scale precipitation rate over time. However, the progressive focusing of flow into regions of limited reactive surface area caused the precipitation rate to decrease throughout the reactive transport. This progressively decreasing rate was most notable for the $A_{f,o}/A_p = 7.5\%$ and $\lambda^* = 0.8$ simulation at $Da = 1.7$, where the reactive surface area increased by more than 5x the initial condition while the precipitation rate only increased by $\sim 70\%$. This flow-focusing process caused the effective rate constant, k, to decrease by $\sim 70\%$ prior to fracture-sealing. Further, at low Da, this flow-focusing process prolonged the sealing process by 2x what would be expected if the sealing timescale was predicted using the initial fracture-scale precipitation rate.

Mineral heterogeneity and fracture surface roughness can vary over orders-of-magnitude (Brown, 1995; Bons, 2001; Garcia-Rios et al., 2017; Ellis and Peters, 2016), which can perturb the relative influence of precipitation-induced reactive surface area enhancement and local transmissivity reduction. However, because precipitation leads to the progressive closure of fracture apertures, the influence of spatially heterogeneous mineralogy is expected to be less significant than mineral abundance (Menefee et al., 2017) and fracture surface roughness (Chaudhuri et al., 2012). The predicted sealing rates, t^*, from our simulations support the conclusion that mineral abundance strongly affects sealing rates. However, our results also show that fracture sealing rates are strongly controlled by flow-focusing into pathways of low-reactivity, which is directly related to the spatial distribution of minerals. The effect of spatial heterogeneity on the precipitation rate was most pronounced for the $A_{f,o}/A_p = 20\%$ and $Da = 0.02$ simulation, where λ^* led to more than a factor of 2 discrepancy in the terminal R_f.

Differences in precipitation rates at later time led to fracture sealing time-scales that were dependent on the initial spatial distribution of reactive minerals as well. For all simulations, the $\lambda^* = 0.8$ simulations took at least 30% longer to seal than the fractures that contained mineral distributions that were correlated over shorter length-scales. This prolonged sealing process was most pronounced in the $A_{f,o}/A_p = 7.5\%$ and $Da = 0.02$ simulations, where λ^* led to a 80% difference in the final sealing timescale. This prolonged sealing time-scale is in good-agreement with the experiments performed by Okamoto and Sekine (2011), in which they observed that variations in the local sealing rate, which led to large disparities in aperture, preserved transmissivity in fractures that were exposed to hydrothermal fluids that induced quartz cementation. Furthermore, our results demonstrate that neglecting the dynamic feedbacks between precipitation, reactive surface area, and transmissivity may impact predictions of mineral precipitation in low-permeability rocks.

Chapter 5

Summary and Concluding Remarks

Fractures act as primary conduits for fluid flow through low-permeability crustal rocks (Zimmerman and Bodvarsson, 1996; Berkowitz, 2002). However, fluid-rock reactions can lead to mineral precipitation, which reduces fracture permeability (Anders et al., 2014; Ankit et al., 2015). This feedback between mineral precipitation and fracture permeability is complicated by fracture surface roughness and mineral heterogeneity (Glassley et al., 2002; Brown, 1995). While the role of surface roughness has been explored in detail (Chaudhuri et al., 2008, 2012), our understanding of the feedback between precipitation and permeability in mineralogically heterogeneous fractures is limited.

In this dissertation, I used a combination of laboratory and numerical experiments to quantify the effect of mineral heterogeneity on the feedback between precipitation and fracture transport properties. Direct transmitted light measurements of mineral precipitation-induced fracture aperture reduction and conservative tracer transport from an experiment conducted in a transparent analog fracture (15 x 15 cm) demonstrated that mineral heterogeneity localizes precipitation reactions to a smaller subset of the domain than would be expected if surface mineralogy is neglected. Preferential sealing of the local fracture-aperture at sites that initially contained reactive minerals focused flow into thin preferential flow paths with limited reactive surface area. Flow focusing led to a 72% reduction in the maximum precipitation rate along the length of the fracture, which corresponded with a 70% reduction in the effective reactive surface area within preferential flow paths that carried the largest flux of dissolved ions.

To further quantify the mechanisms leading to precipitation-induced transport perturbations and corresponding precipitation rate alterations, I developed a numerical model that simulates reactive transport in single fractures that contain varied degrees of surface heterogeneities. Fluid flow across the 2D fracture plane was approximated using a finite-volume integration of the Stokes equation. The depth-averaged advection-diffusion-reaction equation provided quantitative estimates of the local precipitation rates, which were then directly coupled to a three-dimensional fracture surface alteration algorithm that modeled precipitation onto the fracture surface using the level set method. Comparison of these simulation results with a reactive transport model that neglects 3D fracture surface alterations (e.g., Detwiler and Rajaram, 2007; Szymczak and Ladd, 2011) showed that in-plane growth of reactive minerals in mineralogically heterogeneous fractures is a first-order mechanism that controls the evolution of fracture transport properties. Further, simulations using the 3D surface alteration method provided good qualitative agreement between the experimentally observed flow-focusing and the simulated conditions.

To quantify the relative influence of reaction kinetics and fluid transport on the precipitation process, I ran a series of parametric simulations in which the reaction kinetics were systematically varied over a three order-of-magnitude range of kinetic conditions. Results from these parametric simulations show that transport variations were enhanced when the precipitation kinetics were faster than the fluid flux through the fracture. Under these fast-kinetic conditions, precipitation occurred fastest along the periphery of the reactive mineral, which led to rapid sealing along the boundary of the mineral. Enhanced transmissivity variations across the fracture plane led to the generation of fast- and slow-flow regions that progressively localized precipitation reactions to smaller subsets of the domain over time.

Comparison between simulation results where heterogeneous surface mineralogy is (1) explicitly represented, and (2) homogenized across the fracture surface, suggested that the feedback between mineral precipitation and reactive surface area may play an important role in the evolution of the reactive transport. While this mechanism has been recognized in previous studies (Emmanuel and Berkowitz, 2005; Noiriel et al., 2012), the inability to measure geometric reactive surface areas throughout the precipitation process has limited the development of mechanistic tools that constrain the feedback between mineral precipitation and reactive surface area in fractured rocks.

I derived a simple mechanistic model using on a single ODE that describes the geometric evolution of mineral due to the incorporation of dissolved ions onto the mineral surface. Applying this ODE at each reactive mineral in a periodically heterogeneous fracture showed good agreement between simulation results using the level set reactive transport model. These results indicated that, at early time, precipitation led to a linear increase in the fracture-scale reactive surface area. However, as reactive minerals were intercepted by adjacent minerals, the surface area stopped increasing; this suggests that the most important length-scale that constrains the feedback between precipitation and reactive surface area is the characteristic separation length. In smooth-walled fractures, this feedback led to an increase in the fracture-scale precipitation rate that corresponded with the temporal evolution of the reactive surface area.

In natural fractures, precipitation rate enhancement due to the feedback between precipitation and reactive surface area is complicated by transport variations that are induced by fracture surface roughness. To quantify the competition between these two mechanisms, I simulated precipitation in three-dimensional fractures that contained varying degrees of heterogeneity. Results from these small-scale simulations (0.5 x 1.0 cm) demonstrated that precipitation rates increased at a slower rate over time. This progressive slowing suggests can be driven by two mechanisms: (1) a decreasing rate of surface area production, or (2) an increasing localization of flow which reduces the effective reactive surface area. Direct measurements of reactive surface during the precipitation process showed that the reactive surface area increased linearly with time; therefore this mechanism cannot be responsible for slowing precipitation rates. Alternatively, measurements of local precipitation rates across the fracture aperture showed that precipitation was increasingly localized throughout the reactive transport. When the correlation length of the mineral distribution increased, flow became focused into well-defined flow paths that contained limited surface area. These simulation results show that the feedback between precipitation and local transmissivity can lead to a reduction in the effective surface area, which is in good agreement with the experimental observations of precipitation-induced rate reductions in large-scale fractures.

5.0.1 Environmental implications and insight into future research needs

Previous studies of reactive transport in porous media (e.g., Seeboonruang and Ginn, 2006) suggest that precipitation is not sensitive to mineral heterogeneities when the characteristic length-scales of the mineral distribution are smaller than correlation length of the permeability field. Measurements of surface mineralogy show that this is often the case in fractured rocks (e.g., Ellis and Peters, 2016; Garcia-Rios et al., 2017). As a result, predictions of mineral precipitation in fractures often use simplified conceptual models that ignore surface mineralogy (Mitchell et al., 2010), and show that precipitation leads to rapid fracture sealing (Chaudhuri et al., 2008, 2012). However, the time-scales associated with these predictions are often faster than those inferred from field measurements (White and Brantley, 2003) and cannot explain observations of fully-mineralized veins that contain signatures of source-fluids that originate far from the precipitated minerals (Lee and Morse, 1999).

The results presented in this dissertation show that small-scale mineral heterogeneities disrupt the sealing process by focusing flow into preferential paths with limited reactive surface area. When the reaction kinetics are fast enough that concentration gradients develop along the length of the fracture, this flow-focusing process can lead to a reduction in fracture-scale precipitation rate that preserves permeability and prolongs the sealing process. Simulations of mineral precipitation in fractures with the same mineral abundance showed that the spatial distribution of reactive minerals impacted both the sealing time-scale and total mass precipitated onto the fracture surface at the time of fracture sealing, which may have implications for the strength of the cemented fracture (Major et al., 2018). These fracture-scale responses to mineral precipitation are not captured in reactive transport models that either ignore small-scale mineral heterogeneity (Mitchell et al., 2010; Lee and Morse, 1999) or neglect three-dimensional precipitation-induced fracture surface alterations (Menefee et al., 2017).

The experimental and numerical results from this study suggest that there are two length-scales that control the sealing process: (i) fracture aperture, and (ii) the separation length between reactive minerals. When (ii) is greater than (i), the simulation results indicate that aperture reduction enhances transport variations, but sealing is controlled by lateral growth across the surface. Evidence of partially cemented fractures (Lander and Laubach, 2015b; Tsenn, 2015; Tokan-Lawal et al., 2015, 2017) show that these conditions persist throughout nature, however, quantitative measurements of the spatial distribution of reactive minerals are limited. In a recent characterization of a shale sampled from the Lower Bowland formation in the UK, Fauchille et al. (2018) used scattered electron microscopy images to show mineralogy correlation lengths up to 300 μm. However, these length-scales fall within the observed length-scale of single reactive mineral in porous and fractured rocks (e.g., Peters, 2009; Ellis and Peters, 2016; Coggan et al., 2013; Major et al., 2018; Espinoza et al., 2018), which indicates that mineralogy may vary significantly across samples. The results from this dissertation indicate the importance of constraining these length-scales during predictive simulations, and point to the need for more quantitative measurements of the spatial statistics of mineral heterogeneity in fractured rocks.

Lastly, the numerical studies performed here are limited by the computational demands of the level-set surface alteration algorithm. Uniform-grid discretization of relatively small physical domains (e.g. 0.5 x 1.0cm fractures) leads to computational domains that are O(10^7) nodes. Because level sets must be defined for each reactive mineral phase on the upper and lower surface, and then evolved using forward-Euler approximations to the transient PDEs, simulation length-scales become limited by computation time. An alternative method for simulating precipitation in heterogeneous fractures is through the use of volume-averaged mineral abundance properties that are applied uniformly across the fracture surface (Deng et al., 2016, 2018). Further, because mineralogy is represented as a uniform property, precipitation-induced surface alterations are represented a 1D changes across the fracture aperture. While this approach provides the capacity to simulate precipitation over larger spatial scales, our results show that averaging mineralogy across the fracture scale can significantly underestimate transport variations, and corresponding changes in the fracture-scale precipitation rate, that develop throughout the precipitation process.This highlights the need for additional research aimed at developing upscaled methods that represents mineralogy variations across the fracture plane while accurately capturing the dynamic feedbacks between precipitation, reactive surface area, and local transmissivity in heterogeneous fractures.

Bibliography

Pasha Ameli, Jean E. Elkhoury, Joseph P. Morris, and Russell L. Detwiler. Fracture permeability alteration due to chemical and mechanical processes: A coupled high-resolution model. *Rock Mechanics and Rock Engineering*, 47(5):1563–1573, 2014. doi: 10.1007/s00603-014-0575-z. URL `https://doi.org/10.1007/s00603-014-0575-z`.

Mark H. Anders, Stephen E. Laubach, and Christopher H. Scholz. Microfractures: A review. *Journal of Structural Geology*, 69, Part B:377 – 394, 2014. ISSN 0191-8141. doi: http://dx.doi.org/10.1016/j.jsg.2014.05.011. URL `http://www.sciencedirect.com/science/article/pii/S0191814114001151`. Fluids and Structures in Fold and Thrust Belts with Recognition of the Work of David V. Wiltschko.

Benjamin J. Andre and Harihar Rajaram. Dissolution of limestone fractures by cooling waters: Early development of hypogene karst systems. *Water Resources Research*, 41(1), 2005. doi: 10.1029/2004WR003331. URL `https://agupubs.onlinelibrary.wiley.com/doi/abs/10.1029/2004WR003331`.

Kumar Ankit, Janos L. Urai, and Britta Nestler. Microstructural evolution in bitaxial crack-seal veins: A phase-field study. *Journal of Geophysical Research: Solid Earth*, 120 (5):3096–3118, 2015. ISSN 2169-9356. doi: 10.1002/2015JB011934. URL `http://dx.doi.org/10.1002/2015JB011934`. 2015JB011934.

Masoud Arshadi, Harihar Rajaram, Russell L. Detwiler, and Trevor Jones. High-resolution experiments on chemical oxidation of dnapl in variable-aperture fractures. *Water Resources Research*, 51(4):2317–2335, 2015. ISSN 1944-7973. doi: 10.1002/2014WR016159. URL `http://dx.doi.org/10.1002/2014WR016159`.

Pascal Audet and Roland Burgmann. Possible control of subduction zone slow-earthquake periodicity by silica enrichment. *Nature*, 510(7505):389–392, 06 2014. URL `http://dx.doi.org/10.1038/nature13391`.

I. Battiato and D.M. Tartakovsky. Applicability regimes for macroscopic models of reactive transport in porous media. *Journal of Contaminant Hydrology*, 120–121(0):18 – 26, 2011. ISSN 0169-7722. doi: http://dx.doi.org/10.1016/j.jconhyd.2010.05.005. URL `http://www.sciencedirect.com/science/article/pii/S0169772210000525`. Reactive Transport in the Subsurface: Mixing, Spreading and Reaction in Heterogeneous Media.

Lauren E. Beckingham, Elizabeth H. Mitnick, Carl I. Steefel, Shuo Zhang, Marco Voltolini, Alexander M. Swift, Li Yang, David R. Cole, Julia M. Sheets, Jonathan B. Ajo-Franklin, Donald J. DePaolo, Saeko Mito, and Ziqiu Xue. Evaluation of mineral reactive surface area estimates for prediction of reactivity of a multi-mineral sediment. *Geochimica et Cosmochimica Acta*, 188:310–329, 2016. doi: https://doi.org/10.1016/j.gca.2016.05.040. URL `http://www.sciencedirect.com/science/article/pii/S0016703716303003`.

Lauren E. Beckingham, Carl I. Steefel, Alexander M. Swift, Marco Voltolini, Li Yang, Lawrence M. Anovitz, Julia M. Sheets, David R. Cole, Timothy J. Kneafsey, Elizabeth H. Mitnick, Shuo Zhang, Gautier Landrot, Jonathan B. Ajo-Franklin, Donald J. DePaolo, Saeko Mito, and Ziqiu Xue. Evaluation of accessible mineral surface areas for improved prediction of mineral reaction rates in porous media. *Geochimica et Cosmochimica Acta*, 205:31–49, 2017. doi: https://doi.org/10.1016/j.gca.2017.02.006. URL `http://www.sciencedirect.com/science/article/pii/S0016703717300832`.

Brian Berkowitz. Characterizing flow and transport in fractured geological media: A review. *Advances in Water Resources*, 25(8–12):861 – 884, 2002. ISSN 0309-1708. doi: http://dx.doi.org/10.1016/S0309-1708(02)00042-8. URL `http://www.sciencedirect.com/science/article/pii/S0309170802000428`.

A. Blum and Antonio C. Lasaga. *Aquatic Surface Chemistry: Chemical Processes at the Particle-Water Interface*, chapter Monte Carlo simulations of surface reaction rate laws, pages 255–292. John Wiley & Sons, New York, 1987.

F. Boano, J. W. Harvey, A. Marion, A. I. Packman, R. Revelli, L. Ridolfi, and A. Wörman. Hyporheic flow and transport processes: Mechanisms, models, and biogeochemical implications. *Reviews of Geophysics*, 52(4):603–679, 2018/11/16 2014. doi: 10.1002/2012RG000417. URL `https://doi.org/10.1002/2012RG000417`.

James R. Boles, Peter Eichhubl, Grant Garven, and Jim Chen. Evolution of a hydrocarbon migration pathway along basin-bounding faults: Evidence from fault cement. *AAPG Bulletin*, 88(7):947–970, July 2004.

P. D Bons. Development of crystal morphology during unitaxial growth in a progressively widening vein: I. the numerical model. *Journal of Structural Geology*, 23(6):865–872, 2001. doi: https://doi.org/10.1016/S0191-8141(00)00159-0. URL `http://www.sciencedirect.com/science/article/pii/S0191814100001590`.

David F. Boutt, Giovanni Grasselli, Joanne T. Fredrich, Benjamin K. Cook, and John R. Williams. Trapping zones: The effect of fracture roughness on the directional anisotropy of fluid flow and colloid transport in a single fracture. *Geophysical Research Letters*, 33 (21), 2018/08/07 2006. doi: 10.1029/2006GL027275. URL `https://doi.org/10.1029/2006GL027275`.

Stephen R. Brown. Simple mathematical model of a rough fracture. *J. Geophys. Res.-Sol. Ea.*, 100(B4):5941–5952, April 1995.

David J. Brush and Neil R. Thomson. Fluid flow in synthetic rough-walled fractures: Navier-stokes, stokes, and local cubic law simulations. *Water Resources Research*, 39 (4), 2018/10/17 2003. doi: 10.1029/2002WR001346. URL `https://doi.org/10.1029/2002WR001346`.

A. Chaudhuri, H. Rajaram, and H. Viswanathan. Alteration of fractures by precipitation and dissolution in gradient reaction environments: Computational results and stochastic analysis. *Water Resources Research*, 44(10):W10410, 2008. doi: 10.1029/2008WR006982. URL `http://dx.doi.org/10.1029/2008WR006982`.

A. Chaudhuri, H. Rajaram, and H. Viswanathan. Fracture alteration by precipitation resulting from thermal gradients: Upscaled mean aperture-effective transmissivity relationship. *Water Resources Research*, 48(1):n/a–n/a, 2012. ISSN 1944-7973. doi: 10.1029/2011WR010983. URL `http://dx.doi.org/10.1029/2011WR010983`.

Wendy Cheung and Harihar Rajaram. Dissolution finger growth in variable aperture fractures: Role of the tip-region flow field. *Geophysical Research Letters*, 29(22):32–1–32–4, 2002. doi: doi:10.1029/2002GL015196. URL `https://doi.org/10.1029/2002GL015196`.

J. S. Coggan, D. Stead, J. H. Howe, and C. I. Faulks. Mineralogical controls on the engineering behavior of hydrothermally altered granites under uniaxial compression. *Engineering Geology*, 160:89–102, 2013. doi: https://doi.org/10.1016/j.enggeo.2013.04.001. URL `http://www.sciencedirect.com/science/article/pii/S0013795213001105`.

N. G. W. Cook. Natural joints in rock: Mechanical, hydraulic and seismic behaviour and properties under normal stress. *International Journal of Rock Mechanics and Mining Sciences & Geomechanics Abstracts*, 29(3):198–223, 1992. doi: https://doi.org/10.1016/0148-9062(92)93656-5. URL `http://www.sciencedirect.com/science/article/pii/0148906292936565`.

Emilio Custodio. Aquifer overexploitation: what does it mean? *Hydrogeology Journal*, 10 (2):254–277, 2002. doi: 10.1007/s10040-002-0188-6. URL `https://doi.org/10.1007/s10040-002-0188-6`.

Mark O. Cuthbert, Lindsay A. McMillan, Stephanie Handley-Sidhu, Michael. S. Riley, Dominique J. Tobler, and Vernon. R. Phoenix. A field and modeling study of fractured rock permeability reduction using microbially induced calcite precipitation. *Environmental Science & Technology*, 47(23):13637–13643, 2015/02/17 2013. doi: 10.1021/es402601g. URL `http://pubs.acs.org/doi/abs/10.1021/es402601g`.

Gabriela Dávila, Linda Luquot, Josep M. Soler, and Jordi Cama. Interaction between a fractured marl caprock and co2-rich sulfate solution under supercritical co2 conditions. *International Journal of Greenhouse Gas Control*, 48:105–119, 2016. doi: https://doi.org/10.1016/j.ijggc.2015.11.005. URL `http://www.sciencedirect.com/science/article/pii/S1750583615301201`.

Jason T. DeJong, Michael B. Fritzges, and Klaus Nüsslein. Microbially induced cementation to control sand response to undrained shear. *Journal of Geotechnical & Geoenvironmental*

Engineering, 132(11):1381–1392, 11 2006. URL `http://search.ebscohost.com/login.aspx?direct=true&db=a2h&AN=29382685&site=ehost-live`.

D. E. Dempsey, J. V. Rowland, G. A. Zyvoloski, and R. A. Archer. Modeling the effects of silica deposition and fault rupture on natural geothermal systems. *Journal of Geophysical Research: Solid Earth*, 117(B5), 2012. doi: 10.1029/2012JB009218. URL `https://agupubs.onlinelibrary.wiley.com/doi/abs/10.1029/2012JB009218`.

Hang Deng, Sergi Molins, Carl Steefel, Donald DePaolo, Marco Voltolini, Li Yang, and Jonathan Ajo-Franklin. A 2.5d reactive transport model for fracture alteration simulation. *Environmental Science & Technology*, 50(14):7564–7571, 2016. doi: 10.1021/acs.est.6b02184. URL `https://doi.org/10.1021/acs.est.6b02184`. PMID: 27357572.

Hang Deng, Carl Steefel, Sergi Molins, and Donald DePaolo. Fracture evolution in multimineral systems: The role of mineral composition, flow rate, and fracture aperture heterogeneity. *ACS Earth and Space Chemistry*, 2(2):112–124, 02 2018. doi: 10.1021/acsearthspacechem.7b00130. URL `https://doi.org/10.1021/acsearthspacechem.7b00130`.

Russell L. Detwiler and Harihar Rajaram. Predicting dissolution patterns in variable aperture fractures: Evaluation of an enhanced depth-averaged computational model. *Water Resources Research*, 43(4):W04403, 2007. doi: 10.1029/2006WR005147. URL `http://dx.doi.org/10.1029/2006WR005147`.

Russell L. Detwiler, Scott E. Pringle, and Robert J. Glass. Measurement of fracture aperture fields using transmitted light: An evaluation of measurement errors and their influence on simulations of flow and transport through a single fracture. *Water Resources Research*, 35 (9):2605–2617, September 1999.

Russell L. Detwiler, Harihar Rajaram, and Robert J. Glass. Solute transport in variable-aperture fractures: An investigation of the relative importance of taylor dispersion and macrodispersion. *Water Resources Research*, 36(7):1611–1625, 2000. ISSN 1944-7973. doi: 10.1029/2000WR900036. URL `http://dx.doi.org/10.1029/2000WR900036`.

Russell L. Detwiler, Robert J. Glass, and William L. Bourcier. Experimental observations of fracture dissolution: The role of peclet number on evolving aperture variability. *Geophysical Research Letters*, 30(12), 2018/08/06 2003. doi: 10.1029/2003GL017396. URL `https://doi.org/10.1029/2003GL017396`.

A. Ebigbo, A. Phillips, R. Gerlach, R. Helmig, A. B. Cunningham, H. Class, and L. H. Spangler. Darcy-scale modeling of microbially induced carbonate mineral precipitation in sand columns. *Water Resources Research*, 48(7):n/a–n/a, 2012. doi: 10.1029/2011WR011714. URL `http://dx.doi.org/10.1029/2011WR011714`.

Jean E. Elkhoury, Russell L. Detwiler, and Pasha Ameli. Can a fractured caprock self-heal? *Earth and Planetary Science Letters*, 417:99–106, 2015. doi: https://doi.org/10.1016/j.epsl.2015.02.010. URL `http://www.sciencedirect.com/science/article/pii/S0012821X15000886`.

Brian R. Ellis and Catherine A. Peters. 3d mapping of calcite and a demonstration of its relevance to permeability evolution in reactive fractures. *Advances in Water Resources*, 95:246–253, 2016. doi: https://doi.org/10.1016/j.advwatres.2015.07.023. URL `http://www.sciencedirect.com/science/article/pii/S0309170815001724`.

Simon Emmanuel and Brian Berkowitz. Mixing-induced precipitation and porosity evolution in porous media. *Adv. Water. Resour.*, 28(4):337 – 344, 2005. ISSN 0309-1708. doi: http://dx.doi.org/10.1016/j.advwatres.2004.11.010. URL `http://www.sciencedirect.com/science/article/pii/S030917080400212X`.

D. Nicolas Espinoza, Hojung Jung, Jonathan R. Major, Zhuang Sun, Matthew J. Ramos, Peter Eichhubl, Matthew T. Balhoff, R. Charles Choens, and Thomas A. Dewers. Co2 charged brines changed rock strength and stiffness at crystal geyser, utah: Implications for leaking subsurface co2 storage reservoirs. *International Journal of Greenhouse Gas Control*, 73:16–28, 2018. doi: https://doi.org/10.1016/j.ijggc.2018.03.017. URL `http://www.sciencedirect.com/science/article/pii/S1750583617304383`.

A. L. Fauchille, A. P. van den Eijnden, L. Ma, M. Chandler, K. G. Taylor, K. Madi, P. D. Lee, and E. Rutter. Variability in spatial distribution of mineral phases in the lower bowland shale, uk, from the mm- to m-scale: Quantitative characterization and modelling. *Marine and Petroleum Geology*, 92:109–127, 2018. doi: https://doi.org/10.1016/j.marpetgeo.2018.02.029. URL `http://www.sciencedirect.com/science/article/pii/S0264817218300758`.

Donald M. Fisher and Susan L. Brantley. Models of quartz overgrowth and vein formation: Deformation and episodic fluid flow in an ancient subduction zone. *Journal of Geophysical Research: Solid Earth*, 97(B13):20043–20061, 1992. ISSN 2156-2202. doi: 10.1029/92JB01582. URL `http://dx.doi.org/10.1029/92JB01582`.

Donald M. Fisher and Susan L. Brantley. The role of silica redistribution in the evolution of slip instabilities along subduction interfaces: Constraints from the kodiak accretionary complex, alaska. *Journal of Structural Geology*, 69, Part B:395–414, 12 2014. doi: http://dx.doi.org/10.1016/j.jsg.2014.03.010. URL `http://www.sciencedirect.com/science/article/pii/S0191814114000674`.

Yoshiko Fujita, Joanna L. Taylor, Tina L. T. Gresham, Mark E. Delwiche, Frederick S. Colwell, Travis L. McLing, Lynn M. Petzke, and Robert W. Smith. Stimulation of microbial urea hydrolysis in groundwater to enhance calcite precipitation. *Environmental Science & Technology*, 42(8):3025–3032, 04 2008. doi: 10.1021/es702643g. URL `http://dx.doi.org/10.1021/es702643g`.

Maria Garcia-Rios, Linda Luquot, Josep M. Soler, and Jordi Cama. The role of mineral heterogeneity on the hydrogeochemical response of two fractured reservoir rocks in contact with dissolved co2. *Applied Geochemistry*, 84:202–217, 2017. doi: https://doi.org/10.1016/j.apgeochem.2017.06.008. URL `http://www.sciencedirect.com/science/article/pii/S0883292717300069`.

William E. Glassley, Ardyth M. Simmons, and James R. Kercher. Mineralogical heterogeneity in fractured, porous media and its representation in reactive transport models. *Appl. Geochem.*, 17(6):699 – 708, 2002. ISSN 0883-2927. doi: http://dx.doi.org/10.1016/S0883-2927(02)00031-8. URL `http://www.sciencedirect.com/science/article/pii/S0883292702000318`.

Eva Hakami and Erik Larsson. Aperture measurements and flow experiments on a single natural fracture. *International Journal of Rock Mechanics and Mining Sciences & Geomechanics Abstracts*, 33(4):395–404, 1996. doi: https://doi.org/10.1016/0148-9062(95)00070-4. URL `http://www.sciencedirect.com/science/article/pii/0148906295000704`.

R. Blair Hanna and Harihar Rajaram. Influence of aperture variability on dissolutional growth of fissures in karst formations. *Water Resources Research*, 34(11):2843–2853, 1998. doi: 10.1029/98WR01528. URL `http://dx.doi.org/10.1029/98WR01528`.

Judson W. Harvey and Kenneth E. Bencala. The effect of streambed topography on surface-subsurface water exchange in mountain catchments. *Water Resources Research*, 29(1): 89–98, 2010. doi: doi:10.1029/92WR01960. URL `https://doi.org/10.1029/92WR01960`.

R. C. Henneberger and P. R. L. Browne. Hydrothermal alteration and evolution of the ohakuri hydrothermal system, taupo volcanic zone, new zealand. *Journal of Volcanology and Geothermal Research*, 34(3):211–231, 1988. doi: https://doi.org/10.1016/0377-0273(88)90034-0. URL `http://www.sciencedirect.com/science/article/pii/0377027388900340`.

Christoph Hilgers and Janos L. Urai. Experimental study of syntaxial vein growth during lateral fluid flow in transmitted light: first results. *Journal of Structural Geology*, 24(6–7): 1029–1043, 2002/7// 2002. doi: http://dx.doi.org/10.1016/S0191-8141(01)00089-X. URL `http://www.sciencedirect.com/science/article/pii/S019181410100089X`.

Christoph Hilgers, Karin Dilg-Gruschinski, and Janos L. Urai. Microstructural evolution of syntaxial veins formed by advective flow. *Geology*, 32(3):261–264, 2003.

Nicolas J. Huerta, Marc A. Hesse, Steven L. Bryant, Brian R. Strazisar, and Christina L. Lopano. Experimental evidence for self-limiting reactive flow through a fractured cement core: Implications for time-dependent wellbore leakage. *Environmental Science & Technology*, 47(1):269–275, 2013. doi: 10.1021/es3013003. URL `http://pubs.acs.org/doi/abs/10.1021/es3013003`.

Trevor A. Jones and Russell L. Detwiler. Fracture sealing by mineral precipitation: The role of smallscale mineral heterogeneity. *Geophysical Research Letters*, 43(14):7564–7571, 2018/06/25 2016. doi: 10.1002/2016GL069598. URL `https://doi.org/10.1002/2016GL069598`.

Trevor A. Jones and Russell L. Detwiler. Mineral precipitation in fractures: Using the level set method to quantify the role of mineral heterogeneity on transport properties. *In preparation*, 2018.

Qinjun Kang, Dongxiao Zhang, and Shiyi Chen. Simulation of dissolution and precipitation in porous media. *Journal of Geophysical Research: Solid Earth*, 108(B10), 2018/06/28 2003. doi: 10.1029/2003JB002504. URL `https://doi.org/10.1029/2003JB002504`.

W. M. Kays. *Convective Heat and Mass Transfer*. McGraw-Hill, New York., 1966.

Tobias Kling, Jens-Oliver Schwarz, Frank Wendler, Frieder Enzmann, and Philipp Blum. Fracture flow due to hydrothermally induced quartz growth. *Advances in Water Resources*, 107:93 – 107, 2017. ISSN 0309-1708. doi: https://doi.org/10.1016/j.advwatres.2017.06.011. URL `http://www.sciencedirect.com/science/article/pii/S0309170816304705`.

Andrew H. Knoll, Brad L. Jolliff, William H. Farrand, James F. Bell, Clark Benton C., Gellert Ralf, Golombek M. P., Grotzinger John P., Herkenhoff Kenneth E., Johnson Jeffrey R., McLennan Scott M., Morris Richard, Squyres Steven W., Sullivan Robert, Tosca Nicholas J., Yen Albert, and Learner Zoe. Veneers, rinds, and fracture fills: Relatively late alteration of sedimentary rocks at meridiani planum, mars. *Journal of Geophysical Research: Planets*, 113(E6), 2018/07/17 2008. doi: 10.1029/2007JE002949. URL `https://doi.org/10.1029/2007JE002949`.

Patrick Lachassagne, R. Wyns, Pierre Bérard, Thierry Bruel, Laurence Chéry, Thierry Coutand, Jean-François Desprats, and Paul Strat. Exploitation of high-yields in hard-rock aquifers: Downscaling methodology combining gis and multicriteria analysis to delineate field prospecting zones. *Groundwater*, 39(4):568–581, 2018/11/16 2005. doi: 10.1111/j.1745-6584.2001.tb02345.x. URL `https://doi.org/10.1111/j.1745-6584.2001.tb02345.x`.

R.H. Lander and S.E. Laubach. Insights into rates of fracture growth and sealing from a model for quartz cementation in fractured sandstones. *Geological Society of America Bulletin*, 127(3-4):516–538, 2015a.

R.H. Lander and S.E. Laubach. Insights into rates of fracture growth and sealing from a model for quartz cementation in fractured sandstones. *GSA Bulletin*, 127(3-4):516, 2015b. doi: 10.1130/B31092.1. URL `http://dx.doi.org/10.1130/B31092.1`.

Gautier Landrot, Jonathan B. Ajo-Franklin, Li Yang, Stefano Cabrini, and Carl I. Steefel. Measurement of accessible reactive surface area in a sandstone, with application to co2 mineralization. *Chem. Geol.*, 318–319:113–125, 7 2012. doi: http://dx.doi.org/10.1016/j.chemgeo.2012.05.010. URL `http://www.sciencedirect.com/science/article/pii/S000925411200229X`.

Antonio C. Lasaga. Chemical kinetics of water-rock interactions. *Journal of Geophysical Research: Solid Earth*, 89(B6):4009–4025, 1984. ISSN 2156-2202. doi: 10.1029/JB089iB06p04009. URL `http://dx.doi.org/10.1029/JB089iB06p04009`.

Seung Hyun Lee, In Wook Yeo, Kang-Kun Lee, and Russell L. Detwiler. Tail shortening with developing eddies in a rough-walled rock fracture. *Geophysical Research Letters*, 42

(15):6340–6347, 2018/08/07 2015. doi: 10.1002/2015GL065116. URL `https://doi.org/10.1002/2015GL065116`.

Young-Joon Lee and John W Morse. Calcite precipitation in synthetic veins: implications for the time and fluid volume necessary for vein filling. *Chemical Geology*, 156(1–4):151 – 170, 1999. ISSN 0009-2541. doi: http://dx.doi.org/10.1016/S0009-2541(98)00183-1. URL `http://www.sciencedirect.com/science/article/pii/S0009254198001831`.

L. Li, C. A. Peters, and M. A. Celia. Effects of mineral spatial distribution on reaction rates in porous media. *Water Resources Research*, 43(1):n/a–n/a, 2007. ISSN 1944-7973. doi: 10.1029/2005WR004848. URL `http://dx.doi.org/10.1029/2005WR004848`. W01419.

Xiaoyi Li, Hai Huang, and Paul Meakin. A three-dimensional level set simulation of coupled reactive transport and precipitation/dissolution. *International Journal of Heat and Mass Transfer*, 53(13):2908–2923, 2010. doi: https://doi.org/10.1016/j.ijheatmasstransfer.2010.01.044. URL `http://www.sciencedirect.com/science/article/pii/S0017931010000566`.

Peter C. Lichtner. Continuum model for simultaneous chemical reactions and mass transport in hydrothermal systems. *Geochimica et Cosmochimica Acta*, 49(3):779 – 800, 1985. ISSN 0016-7037. doi: http://dx.doi.org/10.1016/0016-7037(85)90172-3. URL `http://www.sciencedirect.com/science/article/pii/0016703785901723`.

Peter C. Lichtner. The quasi-stationary state approximation to coupled mass transport and fluid-rock interaction in a porous medium. *Geochimica et Cosmochimica Acta*, 52(1):143 – 165, 1988. ISSN 0016-7037. doi: http://dx.doi.org/10.1016/0016-7037(88)90063-4. URL `http://www.sciencedirect.com/science/article/pii/0016703788900634`.

Jonathan R. Major, Peter Eichhubl, Thomas A. Dewers, and Jon E. Olson. Effect of co2–brine–rock interaction on fracture mechanical properties of co2 reservoirs and seals. *Earth and Planetary Science Letters*, 499:37–47, 2018. doi: https://doi.org/10.1016/j.epsl.2018.07.013. URL `http://www.sciencedirect.com/science/article/pii/S0012821X18304199`.

E. A. G. Marques, D. J. Williams, I. R. Assis, and M. F. Leão. Effects of weathering on characteristics of rocks in a subtropical climate: weathering morphology, in situ, laboratory and mineralogical characterization. *Environmental Earth Sciences*, 76 (17):602, Aug 2017. ISSN 1866-6299. doi: 10.1007/s12665-017-6936-7. URL `https://doi.org/10.1007/s12665-017-6936-7`.

Juerg M. Matter, Martin Stute, Sandra Ó. Snæbjörnsdottir, Eric H. Oelkers, Sigurdur R. Gislason, Edda S. Aradottir, Bergur Sigfusson, Ingvi Gunnarsson, Holmfridur Sigurdardottir, Einar Gunnlaugsson, Gudni Axelsson, Helgi A. Alfredsson, Domenik Wolff-Boenisch, Kiflom Mesfin, Diana Fernandez de la Reguera Taya, Jennifer Hall, Knud Dideriksen, and Wallace S. Broecker. Rapid carbon mineralization for permanent disposal of anthropogenic carbon dioxide emissions. *Science*, 352(6291):1312–1314, 2016. ISSN 0036-8075. doi: 10.1126/science.aad8132. URL `http://science.sciencemag.org/content/352/6291/1312`.

Anne H. Menefee, Peiyuan Li, Daniel E. Giammar, and Brian R. Ellis. Roles of transport limitations and mineral heterogeneity in carbonation of fractured basalts. *Environmental Science & Technology*, 51(16):9352–9362, 08 2017. doi: 10.1021/acs.est.7b00326. URL `https://doi.org/10.1021/acs.est.7b00326`.

Anne H. Menefee, Daniel E. Giammar, and Brian R. Ellis. Permanent co2 trapping through localized and chemical gradient-driven basalt carbonation. *Environmental Science & Technology*, 52(15):8954–8964, 08 2018. doi: 10.1021/acs.est.8b01814. URL `https://doi.org/10.1021/acs.est.8b01814`.

Andrew C. Mitchell, Adrienne J. Phillips, Randy Hiebert, Robin Gerlach, Lee H. Spangler, and Alfred B. Cunningham. Biofilm enhanced geologic sequestration of supercritical co2. *International Journal of Greenhouse Gas Control*, 3(1):90–99, 1 2009. doi: http://dx.doi.org/10.1016/j.ijggc.2008.05.002. URL `http://www.sciencedirect.com/science/article/pii/S1750583608000406`.

Andrew C. Mitchell, Knud Dideriksen, Lee H. Spangler, Alfred B. Cunningham, and Robin Gerlach. Microbially enhanced carbon capture and storage by mineral-trapping and solubility-trapping. *Environmental Science & Technology*, 44(13):5270–5276, 2015/02/17 2010. doi: 10.1021/es903270w. URL `http://dx.doi.org/10.1021/es903270w`.

Sergi Molins. Reactive interfaces in direct numerical simulation of pore-scale processes. *Pore Scale Geochemical Processes*, pages 461–481, 2015.

Gráinne El Mountassir, Rebecca J. Lunn, Heather Moir, and Erica MacLachlan. Hydrodynamic coupling in microbially mediated fracture mineralization: Formation of self-organized groundwater flow channels. *Water Resources Research*, 50(1):1–16, 2014. ISSN 1944-7973. doi: 10.1002/2013WR013578. URL `http://dx.doi.org/10.1002/2013WR013578`.

G.H Nancollas and M.M Reddy. The crystallization of calcium carbonate. ii. calcite growth mechanism. *Journal of Colloid and Interface Science*, 37(4):824 – 830, 1971. ISSN 0021-9797. doi: http://dx.doi.org/10.1016/0021-9797(71)90363-8. URL `http://www.sciencedirect.com/science/article/pii/0021979771903638`.

Catherine Noiriel, Carl I. Steefel, Li Yang, and Jonathan Ajo-Franklin. Upscaling calcium carbonate precipitation rates from pore to continuum scale. *Chemical Geology*, 318–319 (0):60 – 74, 2012. ISSN 0009-2541. doi: http://dx.doi.org/10.1016/j.chemgeo.2012.05.014. URL `http://www.sciencedirect.com/science/article/pii/S0009254112002331`.

Catherine Noiriel, Philippe Gouze, and Benoît Madé. 3d analysis of geometry and flow changes in a limestone fracture during dissolution. *Journal of Hydrology*, 486(0):211 – 223, 2013. ISSN 0022-1694. doi: http://dx.doi.org/10.1016/j.jhydrol.2013.01.035. URL `http://www.sciencedirect.com/science/article/pii/S0022169413000814`.

Atsushi Okamoto and Kotaro Sekine. Textures of syntaxial quartz veins synthesized by hydrothermal experiments. *Journal of Structural Geology*, 33(12):1764–1775, 2011.

doi: https://doi.org/10.1016/j.jsg.2011.10.004. URL `http://www.sciencedirect.com/science/article/pii/S0191814111001660`.

Assaf P. Oron and Brian Berkowitz. Flow in rock fractures: The local cubic law assumption reexamined. *Water Resources Research*, 34(11):2811–2825, 2018/11/21 1998. doi: 10.1029/98WR02285. URL `https://doi.org/10.1029/98WR02285`.

P. Ortoleva, E. Merino, C. Moore, and J. Chadam. Geochemical self-organization i; reaction-transport feedbacks and modeling approach. *American Journal of Science*, 287:979–1007, December 1987.

Stanley Osher and Ronald Fedkiw. *Level Set Methods and Dynamic Implicit Surfaces*, volume 153. Springer, 2003.

F. Osselin, P. Kondratiuk, A. Budek, O. Cybulski, P. Garstecki, and P. Szymczak. Microfluidic observation of the onset of reactive-infitration instability in an analog fracture. *Geophysical Research Letters*, 43(13):6907–6915, 2016. doi: 10.1002/2016GL069261. URL `https://agupubs.onlinelibrary.wiley.com/doi/abs/10.1002/2016GL069261`.

S. N. Pandey, A. Chaudhuri, S. Kelkar, V. R. Sandeep, and H. Rajaram. Investigation of permeability alteration of fractured limestone reservoir due to geothermal heat extraction using three-dimensional thermo-hydro-chemical (thc) model. *Geothermics*, 51(0):46–62, 7 2014. doi: http://dx.doi.org/10.1016/j.geothermics.2013.11.004. URL `http://www.sciencedirect.com/science/article/pii/S0375650513001156`.

S. N. Pandey, Vikram Vishal, and A. Chaudhuri. Geothermal reservoir modeling in a coupled thermo-hydro-mechanical-chemical approach: A review. *Earth-Science Reviews*, 185:1157–1169, 2018. doi: https://doi.org/10.1016/j.earscirev.2018.09.004. URL `http://www.sciencedirect.com/science/article/pii/S0012825218303301`.

D. L. Parkhurst and C. A. J. Appelo. *Description of Input and examples for Phreeqc version 3 – A computer program for speciation, batch-reaction, one-dimensional transport, and inverse geochemical calculations*, 2013.

Danping Peng, Barry Merriman, Stanley Osher, Hongkai Zhao, and Myungjoo Kang. A pde-based fast local level set method. *Journal of Computational Physics*, 155(2):410–438, 1999. doi: https://doi.org/10.1006/jcph.1999.6345. URL `http://www.sciencedirect.com/science/article/pii/S0021999199963453`.

Catherine A. Peters. Accessibilities of reactive minerals in consolidated sedimentary rock: An imaging study of three sandstones. *Chem. Geol.*, 265(1–2):198 – 208, 2009. ISSN 0009-2541. doi: http://dx.doi.org/10.1016/j.chemgeo.2008.11.014.

Adrienne J. Phillips, Alfred B. Cunningham, Robin Gerlach, Randy Hiebert, Chiachi Hwang, Bartholomeus P. Lomans, Joseph Westrich, Cesar Mantilla, Jim Kirksey, Richard Esposito, and Lee Spangler. Fracture sealing with microbially-induced calcium carbonate precipitation: A field study. *Environmental Science & Technology*, 50(7):4111–4117, 2016. doi: 10.1021/acs.est.5b05559. URL `http://dx.doi.org/10.1021/acs.est.5b05559`. PMID: 26911511.

Roger Powell and Tim Holland. Using equilibrium thermodynamics to understand metamorphism and metamorphic rocks. *Elements*, 6(5):309–314, 10 2010. URL `http://dx.doi.org/10.2113/gselements.6.5.309`.

A. Putnis. Mineral replacement reactions: from macroscopic observations to microscopic mechanisms. *Mineralogical Magazine*, 66(5):689–708, 10 2002. URL `http://dx.doi.org/10.1180/0026461026650056`.

Michael M Reddy and George H Nancollas. The crystallization of calcium carbonate: I. isotopic exchange and kinetics. *Journal of Colloid and Interface Science*, 36(2):166 – 172, 1971. ISSN 0021-9797. doi: http://dx.doi.org/10.1016/0021-9797(71)90161-5. URL `http://www.sciencedirect.com/science/article/pii/0021979771901615`.

J. V. Rowland and R. H. Sibson. Structural controls on hydrothermal flow in a segmented rift system, taupo volcanic zone, new zealand. *Geofluids*, 4(4):259–283, 2018/11/15 2004. doi: 10.1111/j.1468-8123.2004.00091.x. URL `https://doi.org/10.1111/j.1468-8123.2004.00091.x`.

F.J. Ryerson, John Lake, Steven Whittaker, and James W. Johnson. Natural {CO2} accumulations in the western williston basin: A mineralogical analog for {CO2} injection at the weyburn site. *International Journal of Greenhouse Gas Control*, 16, Supplement 1:S25 – S34, 2013. ISSN 1750-5836. doi: http://dx.doi.org/10.1016/j.ijggc.2012.12.015. URL `http://www.sciencedirect.com/science/article/pii/S1750583612003271`. The {IEAGHG} Weyburn-Midale {CO2} Monitoring and Storage Project.

Uma Seeboonruang and Timothy R. Ginn. Upscaling heterogeneity in aquifer reactivity via exposure-time concept: Forward model. *Journal of Contaminant Hydrology*, 84(3–4):127 – 154, 2006. ISSN 0169-7722. doi: http://dx.doi.org/10.1016/j.jconhyd.2005.12.011. URL `http://www.sciencedirect.com/science/article/pii/S0169772205002494`.

J. A. Sethian. Numerical algorithms for propagating interfaces: Hamilton-jacobi equations and conservation laws. *J. Differential Geom.*, 31(1):131–161, 1990. doi: 10.4310/jdg/1214444092. URL `http://dx.doi.org/10.4310/jdg/1214444092`.

J.A. Sethian and Peter Smereka. Level set methods for fluid interfaces. *Ann. Rev. Fluid Mechanics*, 35:341–372, 2003.

Olga Singurindy and Brian Berkowitz. The role of fractures on coupled dissolution and precipitation patterns in carbonate rocks. *Advances in Water Resources*, 28(5):507–521, 2005. doi: https://doi.org/10.1016/j.advwatres.2005.01.002. URL `http://www.sciencedirect.com/science/article/pii/S0309170805000187`.

Megan M. Smith, Yelena Sholokhova, Yue Hao, and Susan A. Carroll. Evaporite caprock integrity: An experimental study of reactive mineralogy and pore-scale heterogeneity during brine-co2 exposure. *Environmental Science & Technology*, 47(1):262–268, 01 2013. doi: 10.1021/es3012723. URL `https://doi.org/10.1021/es3012723`.

Cyprien Soulaine, Sophie Roman, Anthony Kovscek, and Hamdi A. Tchelepi. Mineral dissolution and wormholing from a pore-scale perspective. *Journal of Fluid Mechanics*, 827:457–483, 2017. doi: DOI:10.1017/jfm.2017.499. URL `https://www.cambridge.org/core/article/mineral-dissolution-and-wormholing-from-a-porescale-perspective/82CE22EF080CA51DF1C2BEECA4C582DD`.

Vitaliy Starchenko, Cameron J. Marra, and Anthony J. C. Ladd. Threedimensional simulations of fracture dissolution. *Journal of Geophysical Research: Solid Earth*, 121(9):6421–6444, 2016. doi: 10.1002/2016JB013321. URL `https://agupubs.onlinelibrary.wiley.com/doi/abs/10.1002/2016JB013321`.

C. I. Steefel, C. A. J. Appelo, B. Arora, D. Jacques, T. Kalbacher, O. Kolditz, V. Lagneau, P. C. Lichtner, K. U. Mayer, J. C. L. Meeussen, S. Molins, D. Moulton, H. Shao, J. Šimůnek, N. Spycher, S. B. Yabusaki, and G. T. Yeh. Reactive transport codes for subsurface environmental simulation. *Computational Geosciences*, 19(3):445–478, 2015. doi: 10.1007/s10596-014-9443-x. URL `https://doi.org/10.1007/s10596-014-9443-x`.

Carl I. Steefel and Peter C. Lichtner. Multicomponent reactive transport in discrete fractures: I. controls on reaction front geometry. *Journal of Hydrology*, 209(1–4):186 – 199, 1998. ISSN 0022-1694. doi: http://dx.doi.org/10.1016/S0022-1694(98)00146-2. URL `http://www.sciencedirect.com/science/article/pii/S0022169498001462`.

P. Szymczak and A. J. C. Ladd. Wormhole formation in dissolving fractures. *Journal of Geophysical Research: Solid Earth*, 114(B6):B06203, 2009. doi: 10.1029/2008JB006122. URL `http://dx.doi.org/10.1029/2008JB006122`.

Piotr Szymczak and Anthony J. C. Ladd. Reactive-infiltration instabilities in rocks. fracture dissolution. *Journal of Fluid Mechanics*, 702:239–264, 7 2012. ISSN 1469-7645. doi: 10.1017/jfm.2012.174. URL `http://journals.cambridge.org/article_S0022112012001747`.

Piotr Szymczak and Anthony J.C. Ladd. The initial stages of cave formation: Beyond the one-dimensional paradigm. *Earth and Planetary Science Letters*, 301(3–4):424 – 432, 2011. ISSN 0012-821X. doi: http://dx.doi.org/10.1016/j.epsl.2010.10.026. URL `http://www.sciencedirect.com/science/article/pii/S0012821X10006692`.

Jianwu Tang, Stephan J. Köhler, and Martin Dietzel. Sr2+/ca2+ and 44ca/40ca fractionation during inorganic calcite formation: I. sr incorporation. *Geochimica et Cosmochimica Acta*, 72(15):3718 – 3732, 2008. ISSN 0016-7037. doi: http://dx.doi.org/10.1016/j.gca.2008.05.031. URL `http://www.sciencedirect.com/science/article/pii/S0016703708002895`.

Adenike Tokan-Lawal, Maša Prodanović, and Peter Eichhubl. Investigating flow properties of partially cemented fractures in travis peak formation using image-based pore-scale modeling. *Journal of Geophysical Research: Solid Earth*, 120(8):5453–5466, 2018/08/07 2015. doi: 10.1002/2015JB012045. URL `https://doi.org/10.1002/2015JB012045`.

Adenike Tokan-Lawal, Maša Prodanović, Christopher J. Landry, and Peter Eichhubl. Influence of numerical cementation on multiphase displacement in rough fractures. *Transport in Porous Media*, 116(1):275–293, Jan 2017. ISSN 1573-1634. doi: 10.1007/s11242-016-0773-0. URL `https://doi.org/10.1007/s11242-016-0773-0`.

Michael C. Tsenn. *Permeability of Partially Cemented Fractures*, chapter 8, pages 115–127. American Geophysical Union (AGU), 2015. ISBN 9781118877517. doi: 10.1002/9781118877517.ch8. URL `https://agupubs.onlinelibrary.wiley.com/doi/abs/10.1002/9781118877517.ch8`.

Daniela B. van den Heuvel, Einar Gunnlaugsson, Ingvi Gunnarsson, Tomasz M. Stawski, Caroline L. Peacock, and Liane G. Benning. Understanding amorphous silica scaling under well-constrained conditions inside geothermal pipelines. *Geothermics*, 76: 231–241, 2018. doi: https://doi.org/10.1016/j.geothermics.2018.07.006. URL `http://www.sciencedirect.com/science/article/pii/S0375650517303796`.

Anna Vass, Daniel Koehn, Renaud Toussaint, Irfan Ghani, and Sandra Piazolo. The importance of fracture-healing on the deformation of fluid-filled layered systems. *Journal of Structural Geology*, 67, Part A:94 – 106, 2014. ISSN 0191-8141. doi: http://dx.doi.org/10.1016/j.jsg.2014.07.007. URL `http://www.sciencedirect.com/science/article/pii/S0191814114001539`.

A. Verma and K. Pruess. Thermohydrological conditions and silica redistribution near high-level nuclear wastes emplaced in saturated geological formations. *Journal of Geophysical Research: Solid Earth*, 93(B2):1159–1173, 2018/11/15 1988. doi: 10.1029/JB093iB02p01159. URL `https://doi.org/10.1029/JB093iB02p01159`.

John D. Weeks and George H. Gilmer. *Dynamics of Crystal Growth*, pages 157–228. Wiley-Blackwell, 2007. ISBN 9780470142592. doi: 10.1002/9780470142592.ch4. URL `https://onlinelibrary.wiley.com/doi/abs/10.1002/9780470142592.ch4`.

F. Wendler, A. Okamoto, and P. Blum. Phase-field modeling of epitaxial growth of polycrystalline quartz veins in hydrothermal experiments. *Geofluids*, 16(2):211–230, 2016. doi: 10.1111/gfl.12144. URL `http://dx.doi.org/10.1111/gfl.12144`.

Art F White and Susan L Brantley. The effect of time on the weathering of silicate minerals: why do weathering rates differ in the laboratory and field? *Chemical Geology*, 202(3–4):479 – 506, 2003. ISSN 0009-2541. doi: http://dx.doi.org/10.1016/j.chemgeo.2003.03.001. URL `http://www.sciencedirect.com/science/article/pii/S0009254103002560`. Controls on Chemical Weathering.

Viktoriya M. Yarushina and David Bercovici. Mineral carbon sequestration and induced seismicity. *Geophysical Research Letters*, 40(5):814–818, 2013. doi: 10.1002/grl.50196. URL `http://dx.doi.org/10.1002/grl.50196`.

Zheng Yong-Fei. Calculation of oxygen isotope fractionation in anhydrous silicate minerals. *Geochimica et Cosmochimica Acta*, 57(5):1079–1091, 1993. doi: https://doi.org/10.1016/

0016-7037(93)90042-U. URL `http://www.sciencedirect.com/science/article/pii/001670379390042U`.

D. Yu and A.J.C. Ladd. A numerical simulation method for dissolution in porous and fractured media. *Journal of Computational Physics*, 229(18):6450 – 6465, 2010. ISSN 0021-9991. doi: https://doi.org/10.1016/j.jcp.2010.05.005. URL `http://www.sciencedirect.com/science/article/pii/S0021999110002573`.

Robert W. Zimmerman and Gudmundur S. Bodvarsson. Hydraulic conductivity of rock fractures. *Transport in Porous Media*, 23(1):1–30, 1996. doi: 10.1007/BF00145263. URL `https://doi.org/10.1007/BF00145263`.

Appendix A

Supporting Information for ”Fracture sealing by mineral precipitation: The role of small-scale mineral heterogeneity”

Contents of this file

1. Detailed overview of experimental methods
2. Nonreactive dye tracer animations (Movies S1 and S2)
3. 1D advection-reaction model

Additional Supporting Information (Files uploaded separately)

1. Movie S1 and S2

A.1 Detailed overview of experimental methods

In section 2 of the manuscript, we briefly describe the measurements used to quantify precipitation-induced transport alterations and the resulting changes in local precipitation rates. In this section of the supplementary information, we provide a more detailed discussion of the initial calcite seeding procedure, fracture aperture and transmitted light measurements, and nonreactive dye tracer measurements:

To create mineral heterogeneity, we seeded the flat borosilicate surface with isolated regions of $CaCO_3$ using a modified procedure developed by Nancollas and Reddy (1971). We placed the flat glass in a mixture of $NaHCO_3$ (0.1M) and $CaCl_2$ ($8x10^{-4}$M) ($\log(\Omega_{CaCO_3})$=1.44 at 22^oC) and warmed the unstirred batch reactor to 30^oC to initiate $CaCO_3$ precipitation on the glass surface. After 7 days we lowered the temperature to 22 ± 1^oC and replaced the fluid weekly for approximately 12 weeks to increase the size of the $CaCO_3$ regions.

A red LED panel (PHLOX Red LLUB Backlight) backlit the transparent fracture and a 12-bit charged-coupled-device camera (Photometrics Quantix KAF-6303e) measured changes in transmitted light. An electronic controller synchronized light pulses with camera exposure to create reproducible, high-resolution (83x83-μm pixels) images. Transmitted light measurements provided a direct measure of both the spatial distribution of $CaCO_3$ and fracture aperture, b, over the entire flow field throughout the duration of the experiment.

Precipitated $CaCO_3$ absorbed more light than the glass, which allowed us to filter images of the fracture filled with clear fluid and generate binary maps of the $CaCO_3$ regions (Figure 1a in manuscript). The initial distribution of $CaCO_3$ was heterogeneous and isotropic and $CaCO_3$ initially covered 12% (27 cm^2) of the fracture surface. Microscope images indicated that the initial $CaCO_3$ regions were randomly distributed clusters of rhombohedral crystals with an average edge length of approximately 10 μm. Measurements during the reactive flow experiment demonstrate that precipitation only occurred at preexisting $CaCO_3$ regions.

To measure fracture aperture, b, we filled the fracture with a non-reactive dye tracer (1/16 g/L of FD&C Blue #1, $\log(\Omega_{CaCO_3}) = 0$) and measured the light absorbance, $\ln(I_{cl}/I_{dye})$, where I_{cl} and I_{dye} are measured intensities with the fracture filled with clear and dyed water (Detwiler et al., 1999). We measured the fracture aperture field both before reactive flow initiation (Figure 1b in manuscript) and weekly during the reactive flow experiment. The initial aperture field had a mean of 0.0142 cm and a standard deviation of 0.0042 cm. Small undulations of the rough glass surface caused mild long-wavelength aperture variations oriented perpendicular to the mean flow direction. As the experiment progressed, precipitation-induced flow channeling made it progressively more difficult to uniformly fill the fracture with dyed fluid. As a result, small regions of the aperture field (maximum of 0.5% of the total area) were underestimated; we disregarded these regions when calculating local precipitation rates.

During the reactive flow experiment, continuous-flow syringe pumps (Teledyne ISCO, MODEL 500D) injected a well-mixed $CaCl_2$–$NaHCO_3$ solution, $log(\Omega_{CaCO_3}) = 1.44$, into the fracture at 0.5 ml/min. The reactive fluid was the same solution used for creating the initial mineral heterogeneity, thus ensuring similar precipitation mechanisms throughout the duration of the experiment. To prevent precipitation in the inflow plumbing, a constant temperature bath cooled the $CaCl_2$–$NaHCO_3$ inlet reservoir to 15^oC. Type-T thermocouples placed in the inlet and outlet manifolds monitored temperature in the fracture over the duration of the experiment ($T_{exp} = 22 \pm 1^oC$, $log(\Omega_{CaCO3}) = 1.44 \pm 0.1$). We paused reactive flow during weekly aperture measurements and imaged the fracture while filling it with the nonreactive dye. We used the corresponding light absorbance measurements to calculate the evolving dye concentration field (C/C_o, where C_o is the injected dye concentration) within the fracture (Detwiler et al., 2000).

A.2 Nonreactive dye tracer animations (Movies S1 and S2)

Nonreactive ($log(\Omega_{CaCO_3}) = 0$) tracer measurements acquired during weekly fracture aperture measurements provide a quantitative measure of precipitation-induced flow field alterations. The included movie files show the nonreactive dye tracer (1/16 gr/l FD&C #2 blue dye) injection process prior to reactive flow ($t = 0$ days, Movie S1) and after 82 days of $CaCl_2$-$NaHCO_3$ injection (Movie S2) . We imaged the dye injection process using a high-resolution CCD camera (83 x 83 μm) and used Beer-Lambert's law to relate absorbance to the local dye concentrations. A syringe pump injected the nonreactive tracer into the fracture at 1 ml/min, which is twice the $CaCl_2$-$NaHCO_3$ flow rate, in order to minimize the time required to ensure C = 1/16 gr/l across the flow field and limit the pause in reactive flow required during fracture-aperture measurements. The normalized dye concentration videos (C/C_o, where C_o is the injected dye concentration) show the nonreactive tracer injected from left to right. We acquired C/C_o measurements every 30 seconds prior to the onset of reactive flow (t = 0 days) and every 10 seconds during the measurement for t = 82 days. Snapshots at 0.3 injected pore-volumes are presented in Figure 3 and are used to demonstrate how alterations in the flow field affect fracture-scale precipitation rates.

Movie S1. C/C_o measurements prior to the onset of reactive flow show that initial aperture variability induces velocity variations across the flow field. C/C_o shows weak preferential flow paths with thin tendrils of elevated C/C_o at the leading edge of the dye front. Variations in the mean velocity caused long-wavelength variability in C/C_o. The large regions over which $C/C_o \sim 1$ indicate that mixing between fast and slow paths quickly dampens initial concentration variations across the flow field.

Movie S2. C/C_o measurements after 82 days of $CaCl_2$-$NaHCO_3$ injection show that mineral precipitation alters the flow field. Precipitation within the first 60 mm of the fracture focuses preferential flow into large-aperture paths that spread laterally after exiting the reaction zone. Mineral precipitation along the primary flow path boundaries create low-flow regions that experience small dissolved ion fluxes. Travel times into low-flow regions increase which suggests that precipitation rates in regions where $C/C_o < 1$ decreases over the duration of the experiment.

A.3 1D Advection Reaction Model

In section 3 of the letter, we introduce a 1D advection-reaction model that is used to predict precipitation rates along the fracture length. We derived the one dimensional model by performing a mass-balance over a differential volume of the fracture. The characteristic volume was represented using the mean aperture and average reactive surface area. The mass-balance yields the following equation for concentration along the fracture length:

$$\frac{dc}{dx} = -\frac{k \cdot A_R}{v \cdot b} * (\Omega_{CaCO_3} - 1)^3 \tag{A.1}$$

where k is the reaction rate coefficient $(\frac{\mathrm{cm}^2}{\mathrm{cm}^2\mathrm{s}})$, A_R is the available reactive mineral surface area per unit width of the fracture $(\frac{\mathrm{cm}^2}{\mathrm{cm}^2})$, v is the mean velocity $(\frac{\mathrm{cm}}{\mathrm{s}})$, b is the mean aperture (cm), and Ω_{CaCO_3} is the saturation index of the pore fluid with respect to calcite. Calculating the saturation index, $\Omega_{CaCO_3} = \frac{a_{Ca^{2+}} a_{CO_3^{2-}}}{K_{sp}}$, where $a_{Ca^{2+}}$ and $a_{CO_3^{2-}}$ are the activities of Ca^{2+} and CO_3^{2-}, respectively, and K_{sp} is the solubility product, requires a detailed description of the chemical composition of the $\mathrm{CaCl_2}$–$\mathrm{NaHCO_3}$ mixture used in our experiment. In lieu of tracking each complex in the mixture, we chose to adopt a single-species reactive transport approach. The equivalent single-species advection-reaction equation is given by:

$$\frac{dc}{dx} = -\frac{k \cdot A_R}{v \cdot b} * (\frac{C}{C_s} - 1)^3 \tag{A.2}$$

where we define C as the concentration of Ca^{2+} ions, and C_s is the solubility concentration of Ca^{2+} at atmospheric conditions. Because Ω_{CaCO_3} depends on the ionic strength of the solution, C/C_s cannot be directly substituted for Ω_{CaCO_3} without incorporating the change in ionic strength due to precipitation. We empirically derived a relationship between C/C_s and Ω_{CaCO_3} to account for the effects of ionic strength by running a series of numerical experiments using Phreeqc (Parkhurst and Appelo, 2013). The Phreeqc simulations were performed as batch-reactions using the same fluid composition as the reactive fluid in our experiment. 500 ml of 0.02M $NaHCO_3$ and 500 ml of $8\text{x}10^{-4}$M $CaCl_2$ were numerically mixed and allowed to precipitate until a desired Ω_{CaCO_3}. Each simulation output Ω_{CaCO_3} and the corresponding Ca^{2+} concentration, which allowed us to generate a functional relationship between Ω_{CaCO_3} and C/C_s. C_s was calculated by finding the soluble Ca^{2+} concentration when the batch reactor was allowed to precipitate until the solution reached equilibrium.

Figure A.1 shows Ω_{CaCO_3} plotted against C/C_s. The linear relationship between Ω_{CaCO_3} and C/C_s supports a singe species modeling approach. Thus, we incorporate the effects of ionic strength on precipitation rates by substituting $\Omega_{CaCO_3} = 1.3\frac{C}{C_s} - 0.78$ into equation A.1 to get:

$$\frac{dc}{dx} = -\frac{k \cdot A_R}{v \cdot b} * (1.3\frac{C}{C_s} - 1.78)^3 \tag{A.3}$$

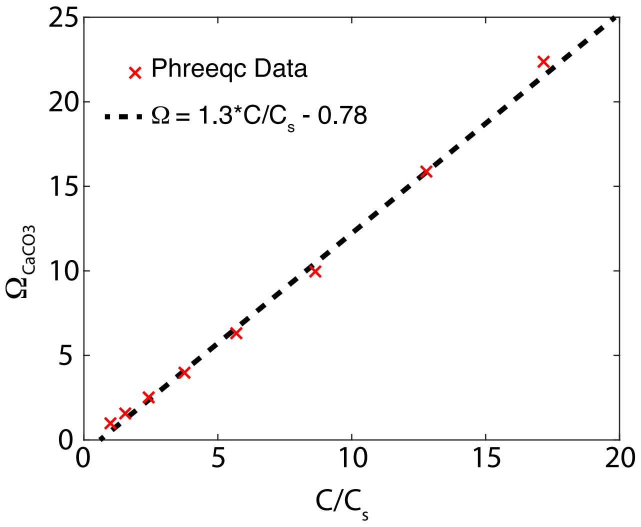

Figure A.1: Ω_{CaCO_3} plotted against C/C_s shows a linear relationship between calcite saturation index and Ca^{2+} concentration, which supports the use of a single species reactive transport model. Both Ω_{CaCO_3} and C/C_s were calculated using Phreeqc.

Equation A.3 predicts Ca^{2+} concentrations along the length of the fracture. We used these Ca^{2+} concentrations to model our measured width-averaged precipitation rates, $\bar{R}$ ($\frac{\text{cm}}{\text{s}}$), by plugging the predicted Ca^{2+} concentrations into $\bar{R} = \frac{M_{CaCO_3}}{\rho_{CaCO_3}} \cdot k \cdot A_R(1.3\frac{C}{C_s} - 1.78)^3$, where M_{CaCO_3} is the molar mass of CaCO$_3$ ($\frac{\text{g}}{\text{mol}}$), and ρ_{CaCO_3} is the density of calcite ($\frac{\text{g}}{\text{cm}^2}$). When the correlation length of the aperture and mineral heterogeneity is much shorter than the length of the fracture, equation A.3 can accurately describe Ca^{2+} transport along the fracture length. However, equation A.3 is not capable of capturing long-wavelength concentration variations that are caused by initial variability in either the mean velocity, mean aperture, or average surface mineralogy.

The nonreactive dye tracer measurements, $\log(\Omega_{CaCO_3}) = 0$, acquired during weekly aperture measurements show variations in the mean velocity across the fracture at the onset of our experiment. In order to use equation A.3 to predict $\bar{R}$ along the fracture, we segmented the fracture into individual streamtubes that contained similar mean velocities. The streamtubes were determined using the nonreactive dye tracer measurements and were used as masks to isolate specific regions of the fracture when calculating $\bar{R}$ from aperture measurements and

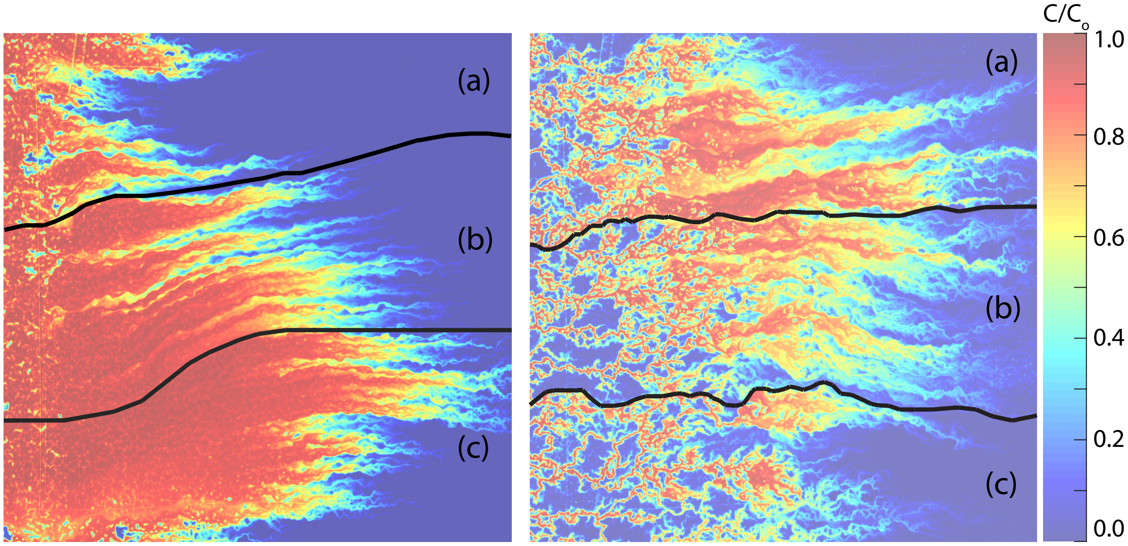

Figure A.2: Streamtubes (denoted by black lines) superimposed on top of the normalized dye concentration measurements, C/C_o, where C is the local dye concentration and C_o is the injected dye concentration. Flow is from left to right. At onset of our experiment, $t = 0$ days, the three streamtube shows a long-wavelength trend towards the upper portion of the fracture. Velocity is largest in streamtube (c) and slowest in streamtube (a). At later time, $t = 82$ days, $CaCO_3$ precipitation within the reaction zone diminished initial variations in the mean velocity, which resulted in much more uniform streamtubes. Although the characteristic streamtubes at late time are uniform, flow is much more localized.

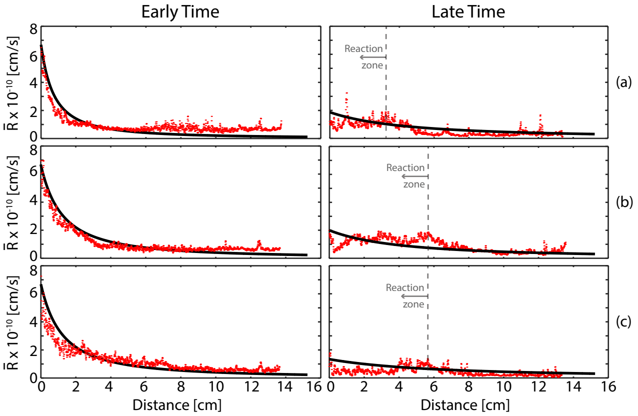

Figure A.3: Measured width-averaged precipitation rate (red dots), $\bar{R}$ ($\frac{\text{cm}}{\text{s}}$), compared with $\bar{R}$ predicted using equation A.3 (black lines). At early time, the 1D advection-reaction model agrees very well with our measured precipitation rates. At later time, predicted and measured $\bar{R}$ deviate significantly. Measured $\bar{R}$ shows a non-monotonic trend in precipitation rate along the fracture length, while equation A.3 predicts a monotonic decrease away from the fracture inlet. This discrepancy results from the development of preferential flow.

predicting $\bar{R}$ from equation A.3. Figure A.2 shows the outlined streamtubes (black lines) superimposed on top of the nonreactive dye tracer measurements at early and late time. At early time, the streamtubes show a long-wavelength trend towards the upper portion of the fracture. At later time, $CaCO_3$ precipitation near the inlet diminished the variability in mean velocity and the streamtubes became much more uniform.

At early time, Figure A.3 shows that the one-dimensional model agrees very well with the measured precipitation rates along the length of the fracture using a value of $k \cdot A_R = 10^{-14.46} \frac{\text{mol}}{\text{cm}^2 \cdot s}$. The agreement between predicted and measured $\bar{R}$ demonstrates that despite local aperture and mineral heterogeneity, a simple 1D model, that uses average aperture, reactive surface area, and velocity, effective predicts mineral precipitation rates along the length of a streamtube. At early time, $\bar{R}$ shows a monotonic decrease for both the predicted and measured rates. In the upper streamtube (a), $\bar{R}$ decreases rapidly due to long residence times and a slow mean velocity along the streamtube length. In the lower streamtube (c), the relatively fast velocity allows $\bar{R}$ to remain relatively high farther into the fracture.

At late time, as discussed in the letter, the predicted and measured $\bar{R}$ deviate significantly.

In all three streamtubes, the best fit to our measured data required a 70% reduction of $k \cdot A_R$, which corresponds closely to our observed reduction in projected $CaCO_3$ area. Equation A.3 predicts a monotonic decline in $\bar{R}$ along the fracture length in all three streamtubes. However, $\bar{R}$ calculated from our aperture measurements clearly demonstrate a non-monotonic trend across the fracture length. The measured $\bar{R}$ shows that precipitation rates are largest at the leading edge of the reaction zone, and decrease downstream of the zone of altered aperture. Within the reaction zone, $\bar{R}$ either remains relatively constant or increases slightly, which is a likely indicator of the local abundance of $CaCO_3$ reaction sites. In all three streamtubes, the 1D advection-reaction model is incapable of capturing the non-monotonic trend in $\bar{R}$ because the development of preferential flow focuses large dissolved ion fluxes into regions of low reactivity. As this process further develops, the average aperture, velocity, and mineralogy used in equation A.3 became less representative of the fracture properties that control mineral precipitation.

Appendix B

Supporting Information for ”Model development: Using the level set method to quantify the role of mineral heterogeneity on transport properties”

Contents of this file

1. Precipitation in a homogeneous fracture: Comparison to a 1D analytical solution
2. Mass preservation with the level set model
3. Animation captions
4. Introduction to model files and instructions to access GITHUB repository

Additional Supporting Information (Files uploaded separately)

1. Animations for Simulations presented in Section 3

Introduction

In this supporting document, we provide additional details that support the results presented in Section 3 of the manuscript. To do this, we first derive the ODE used to validate the 3D level set surface alteration model then compare simulation results with the analytical solution. After this, we present our approach for quantifying mass-conservations during fracture surface alteration and demonstrate the ability of the level set model to preserve mass during reactive transport simulations.

In addition, we have attached animations for the results presented in Section 3 of the manuscript. Each animation contains a corresponding caption that briefly describes the qualitative results as well as the quantitative implications of different reactive transport conditions on the evolution of the reactive transport. Lastly, we provide a detailed discussion of the model files (provided in the linked GITHUB repository). The repository includes all level set functions, reactive transport solvers, and input files used to generate results for the simulations presented in the manuscript.

1. Precipitation in a 1D fracture

To validate the level set surface alteration method, we compared simulation results to a 1D analytical solution derived from the quasi-steady-state depth-averaged advection-diffusion-reaction equation. Depth-averaging the advection-diffusion-reaction equation yields:

$$\nabla \cdot (qc) - \nabla \cdot (Db\nabla c) = R(c) \tag{B.1}$$

where q is the local fluid flux, D is the molecular diffusion coefficient, b is the fracture aperture, and c is the local dissolved ion concentrations. When diffusion is much slower than the advective flux through the fracture, (B.1) reduces to:

$$\nabla \cdot (qc) = R(c) \tag{B.2}$$

The local reaction rate, $R(c)$, is described using a Transition-state-theory rate law:

$$R(c) = k_m(1 - \Omega) \tag{B.3}$$

where k_m is the reaction rate constant for mineral m and $\Omega = \frac{IAP}{K_{sp}}$. The ion activity product, IAP, for calcium carbonate is $a_{Ca^{2+}} \cdot a_{CO_3^{2-}}$ and K_{sp} is the solubility product. Because Ω depends on the activity of both Ca^{2+} and CO_3^{2-}, which changes with ionic strength of the solution, (B.1) leads to a system of coupled ODE's that cannot be integrated analytically. However, over the range of geochemical conditions explored throughout our simulations, Figure SB.1 shows that $[Ca^{2+}]/[Ca^{2+}]_s$ provides a reasonable estimate of Ω. This simplifies (B.3) to:

$$R(c) = k_m(1 - \frac{c}{c_s}) = k(c_s - c) \tag{B.4}$$

For simplicity we have lumped the solubility concentration, c_s, into the single-species rate constant, k, which describes the flux of dissolved ions onto the fracture surface. Applying this simplification and combining (B.4) and (B.2) subject to constant flow boundary conditions yields:

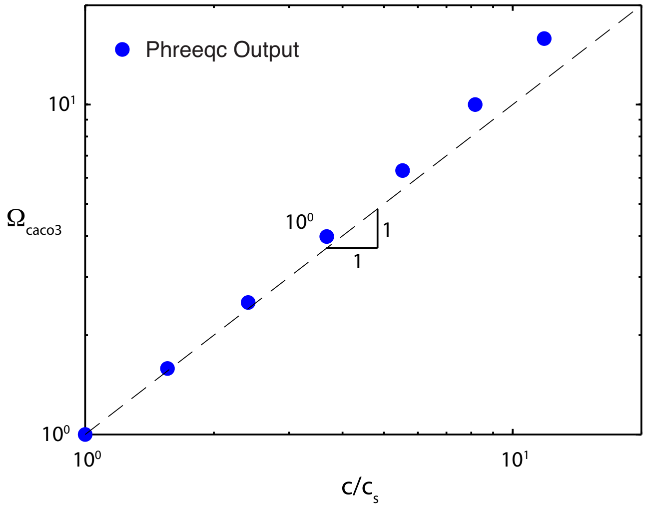

Figure B.1: Normalized 1D aperture alteration profiles computed using the analytical solution (solid lines), the 1D vertical growth model (green diamonds), and 3D level set model (black asterisks). The simulation results are shown at t = 0.75* t_f, for Da = 14, 1.4, 0.14, and 0.014.

$$\frac{dc}{dx} = \frac{k}{q}(c - c_s) \tag{B.5}$$

Equation (B.5) is an ODE that can be integrated analytically to yield a simple analytical solution for the 1D concentration profile in a homogeneous fracture:

$$c(x) = c_s + (c_o - c_s) * exp(-\frac{k}{q}x) \tag{B.6}$$

where c_s and c_o are the solubility and inlet concentration of the dissolved ion. Local disequilibrium between the dissolved ion concentration and mineral solubility drives precipitation onto the fracture surface. This precipitation process is described through (B.7)

$$\frac{db}{dt} = \frac{k(c - c_s)}{\alpha\rho} \tag{B.7}$$

where ρ is the density of the precipitating mineral, and α is the stoichiometric coefficient that relates the moles of dissolved ions to moles of the produced solid phase.

Combining (B.6) and (B.7) and integrating in time yields an analytical solution for precipitation-induced aperture alterations in a 1D homogeneous fracture:

$$b(x,t) = b_o + \frac{t}{\alpha\rho}(c_o - c_s)exp(\frac{-k}{q}x) \tag{B.8}$$

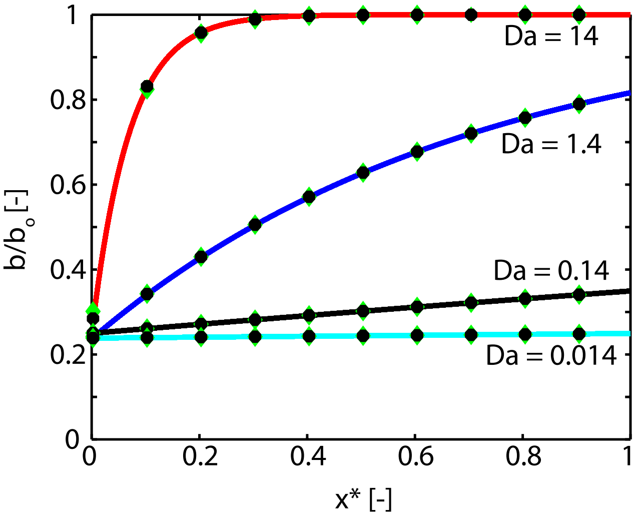

Figure B.2: Normalized 1D aperture alteration profiles computed using the analytical solution (solid lines), the 1D vertical growth model (green diamonds), and 3D level set model (black asterisks). The simulation results are shown at t = 0.75* t_f, for Da = 14, 1.4, 0.14, and 0.014.

Figure SB.2 shows the 1D aperture profiles computed with (B.8) (solid lines), the 1D vertical growth model (green diamonds), and the 3D level set model (black dots). The y-axis shows the aperture profile, b, normalized by the initial aperture, b_o. Small b/b_o values indicate that mineral precipitation has reduced the fracture aperture, while b/b_o values equal to 1 indicate regions of the fracture that have remained unaltered. The 1D aperture profiles are shown at 75% of the fracture sealing timescale, t_f.

Results from Figure SB.2 demonstrate very good agreement between the level set reactive transport model and (B.8). At low Da numbers, mineral reactions persisted throughout the entire length of the fracture, and the gradient of the aperture profile remained relatively small. Under these conditions, both the 3D level set model and 1D vertical growth model reproduced the analytical solution very well, producing a maximum error of approximately 0.012%.

The largest discrepancy between the numerical and analytical solutions occured at $Da = 14$. Under these conditions, Figure SB.2 shows that precipitation at the fracture inlet led to large curvature in the aperture profile. Despite using a first-order gradient approximation, the 3D level set model reproduced this profile very well - at the fracture inlet the 3D level set model overestimated the aperture by only 3%, while the 1D vertical growth model overestimated the inlet aperture by 11%.

2. Mass preservation with the Level Set Model

Although the reactive transport equations are inherently mass conserving, it is important to test that the numerical algorithm preserves mass throughout the surface alteration process. Specifically, the level set method is know to generate mass during reinitialization (Sethian, 1990), which may lead to non-physical results during the reactive transport simulations. In order to ensure that mass is accurately preserved throughout the reactive transport, we measured mass preservation (e.g. mass error) over a wide range of geochemical conditions and fracture surface geometries.

We quantified mass error by comparing the change in mass flow rate through the fracture to the mass flow rate onto the fracture surfaces. The mass flow rate through the fracture is:

$$\dot{m}_Q = \sum_{i=1}^{n_x} (Q \cdot c)_{in} - \sum_{i=1}^{n_x} (Q \cdot c)_{out} \tag{B.9}$$

where Q is the local flow rate and n_x is the number of grid-blocks along the fracture width. The mass flow rate onto the fracture surface is:

$$\dot{m}_R = \sum_{j=1}^{n_x * n_y} \frac{1}{\rho} \frac{\Delta V}{\Delta t} \tag{B.10}$$

where ΔV is the volume added to the fracture surface between simulation outputs, Δt is the time step, $n_x * n_y$ is the number of grid block across the fracture surface, and ρ is the density of the precipitated mineral. The mass error after each time steps is the difference between (B.9) and (B.10).

Figure SB.3A shows the cumulative mass error for three different initial fracture geometries: (1) a parallel plate fracture with uniform surface mineralogy (smooth-uniform), (2) a parallel plate fracture with heterogeneous surface mineralogy (smooth-variable), and (3) a rough-walled fractured with heterogeneous surface mineralogy (rough-variable). The mass error is reported as the sum of squared error between $\dot{m}_Q$ and $\dot{m}_R$ after mineral precipitation has reduced the fracture permeability by an order of magnitude. The mass errors are plotted against Da to quantify the impact of changing transport conditions on our method's ability to conserve mass. Figure SB.3B shows the difference in mass flux, $\dot{m}_Q - \dot{m}_R$, for the rough-rough simulation at $Da = 750$.

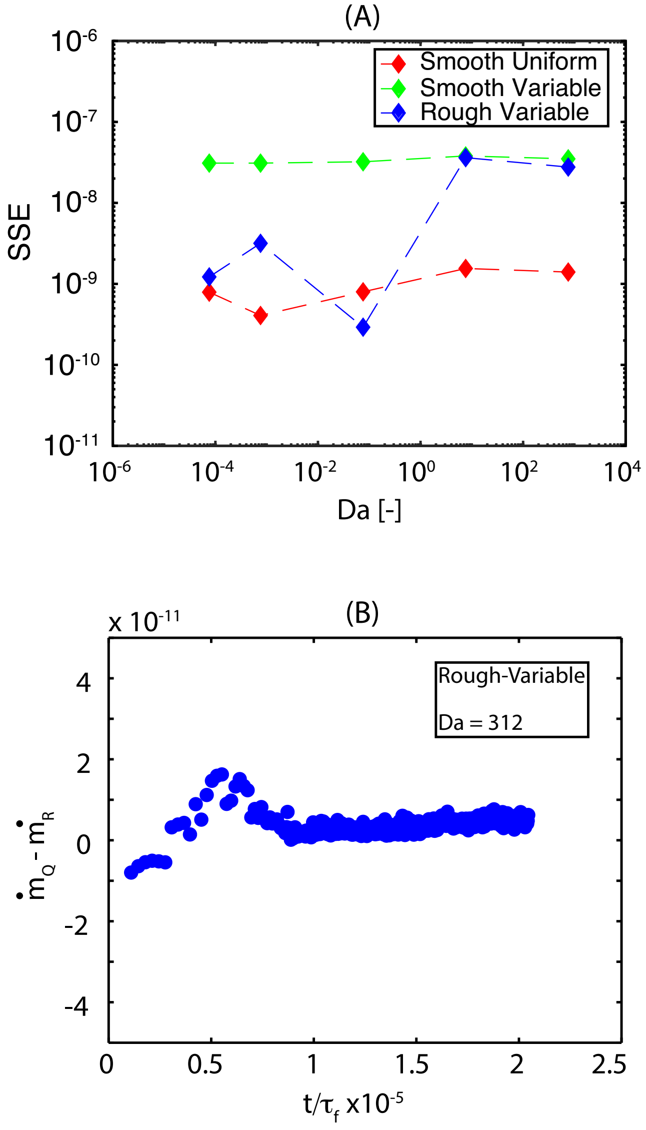

Figure B.3: (A) Cumulative mass error after an order-of-magnitude reduction in fracture transmissivity when simulating reactive transport with the 3D level set model. Three fracture geometries were tested: (1) smooth-walled fracture with no mineral heterogeneities (smooth-uniform), (2) smooth-walled fracture with mineral heterogeneities (smooth-variable), and (3) a rough-walled fracture with mineral heterogeneities (rough-variable). These three fracture geometries were examined over a 7 order-of-magnitude range of Da numbers. (B) Temporal evolution of the mass errors after each reactive-transport/surface evolution step for the rough-variable simulation.

Figure SB.3A shows that the 3D level set model preserves mass well. The cumulative mass error was smallest for the smooth-smooth case, where the maximum mass error of 1.5e-9 occurs at $Da = 8$. In general, the largest mass error values occured with the smooth-variable simulations. For these simulations, the mass error varied between 2.7e-8 and 3.5e-8, and remained relatively constant across all Da. The largest variability in cumulative mass error occurred in the fully heterogeneous simulations (rough-variable). At low Da, the mass error followed similar trends as those generated in the smooth-smooth simulations. However, as Da increased, the mass error increased to the same order of magnitude as the smooth-variable simulations.

To further assess the propagation of these errors throughout the reactive transport simulations, we show the mass error after each time step for the rough-variable simulation at $Da = 750$. Figure SB.3B shows the mass error for this simulation plotted against normalized time. At early time, the 3D level set method slightly overestimated the mass of precipitated mineral (e.g. $\dot{m}_Q - \dot{m}_R < 0$). After relatively short time, the level set representation of the mineral volume accurately reflected the change in mass calculated from the reactive transport solver. At the end of the simulation, $\dot{m}_Q - \dot{m}_R = 5.8x10^{-12}$, which is a mass error of approximately 1%.

3. Simulation Animations

Simulated dissolved ion concentrations ($\bar{c}$), normalized aperture (b/b_o), and transmissivity (T) provide a quantitative measure of the feedback between precipitation and local transmissivity and the resulting effects on dissolved mineral transport. The animations included as additional supporting information depict the temporal evolution of $\bar{c}$, b/b_o, and T for the simulations presented in Section 3.2 and 3.3 of the manuscript. In these simulations, we inject a supersaturated $CaCO_3$ solution ($\log_{10}(\Omega) = 1.44$) into the fracture from left to right at a 0.5 ml/min. We output simulation results in 1% increments of decreasing transmissivity and stop the simulations after precipitation has reduced T by two-orders-of-magnitude. In Section 3.2 of the manuscript, we show and discuss the simulation results at $t^* = 0.1$, 0.5, and 2.0. To simplify the presentation of results in Section 3.3 of the manuscript, we show simulation results after precipitation has reduced transmissivity by an order-of-magnitude.

Movie S1

Results for the simulation presented in Section 3.2. In this simulation, the solution chemistry was similar to that described in Reddy and Nancollas (1971); thus we used the corresponding rate constant ($k = 10^{-6.86}$ mol $\cdot$ m^{-2} $\cdot$ s^{-1}) measured from their experiments. At early-time, surface roughness and mineral heterogeneity induced variations in $\bar{c}$ across the fracture. The relatively fast precipitation rates led to enhanced lateral spreading of $CaCO_3$ at the fracture inlet, which perturbed flow and enhanced $\bar{c}$ variations across the domain. These dynamics are not captured when precipitation-induced surface alterations are modeled as a 1D process.

Movie S2

Results for $Da = 0.03$ (k $= 10^{-8.7}$ mol $\cdot$ m^2 $\cdot$ s^{-1}). Precipitation rates remained relatively uniform across the fracture throughout the simulation, which led to uniform growth of the $CaCO_3$ reaction sites. As precipitation sealed the local aperture, flow became increasing focused into a single preferential flow path. Sealing occurred rapidly ($t^* = 2.62$) due to uniform growth of the reactive minerals.

Movie S3

Results for $Da = 400.0$ (k = $10^{-5.6}$ mol $\cdot$ m^2 $\cdot$ s^{-1}). The fast kinetics led to faster precipitation rates at the fracture inlet than the outlet. As a result, lateral growth of $CaCO_3$ was rapid, significantly enhancing preferential flow at the fracture inlet. Flow focusing limited precipitation to $CaCO_3$ regions that bordered preferential flow paths. This enhanced transport limitation significantly increased sealing timescales ($t^* \sim 24$).

Model Files and Repository

The model files used to simulate mineral precipitation in a heterogeneous fracture are available through a public GITHUB repository: `https://github.com/spl-detwiler/LS_SFRT`.

Within the repository, the model files are separated into three different categories: (1) Level set functions, (2) flow and transport functions, and (3) Run scripts. All subroutines used to calculate surface alterations using the level set method are found in the "Level set functions" directory, and similarly all subroutines required to simulate flow and dissolved ion transport through the fracture are found in the "flow and transport" directory. The run script directory contains a sample run script that employs both the level set surface alteration and 1D vertical growth method for simulating precipitation. There is also a sample $\phi(\vec{x})$ field and sample input file, both of which are needed to run the matlab script. Each function contains a header that describes the proper usage, input, and output for each subroutine. When available, we use built-in optimized matlab linear algebra functions, such as "circshift", "diff", and the "\" command. During large-scale simulations, we run these scripts on a High Performance Computing platform, where we compile the MATLAB functions and run the simulation on a 16-core node.

Below, we provide a brief description of each MATLAB function within the GITHUB repository:

Flow and Transport: ap_gen.m

A random field generator that can be used to generate both random aperture and mineralogy distributions.

Flow and Transport: flow_2d.m

A depth-averaged 2D flow solver. Flow is assumed to be injected from left to right. Constant head boundary conditions are applied to the left and right boundaries, and either no-flow or periodic boundary conditions are applied to the top and bottom boundaries. User specifies the type of upper and lower boundary conditions.

Flow and Transport: transport_2d.m

A depth-averaged reactive transport solver. Using the output flow field calculated from flow_2d.m, transport_2d.m calculates the steady-state concentration field across the 2D fracture plane. Similar to flow_2d.m, the user specifies the upper and lower boundary conditions types (either no-flow or periodic). The solver requires a fixed concentration boundary condition at the fracture inlet. Reactions are currently limited to linear kinetics. Output is a concentration field that can be used to calculate the local reaction rate.

Level Set Function: applyrate3D.m

A function that applies the local reaction rate to the three-dimensional fluid-rock interface (e.g. fracture surface).

Level Set Function: calcA_3D.m

Surface integral of the 3D level set function that provides an estimate of the local reactive surface area. Output is a 2D array that constrains the surface area within each column of the 3D level set domain.

Level Set Function: calcB.m

Volume integral of the 3D level set function that provides solid-volume fractions within each cell of the level set domain. After calculating the volume integral, calcB.m sums the total solid volume within a given column and normalizes by the cross-sectional area of the cell to output a 2D surface elevation.

Level Set Function: diffPhi.m

Performs forward and backward difference approximations to the local gradient of $\phi(\vec{x})$ across the 3D level set domain. The forward differences at the fracture outlet and bottom of the fracture are fixed and set to zero. The backward differences at the fracture inlet and top of the fracture are fixed and set to zero. At the boundaries parallel to the mean flow direction, the use specifies the boundary condition type: periodic or no-flow. If no-flow, then the backward difference at the left boundary = 0, and the forward difference at the right boundary = 0. If the user specifies periodic boundary conditions, diffPhi.m will not fix the local gradient at the left and right boundary. diffPhi.m is used when performing the implicit gradient approximation following the scheme presented in Peng et al. (1999).

diffPhi.m is used during the reinitialization and velocity extension step. It is not used when advecting the fracture surface interface.

Level Set Function: Fext3D.m

Performs the velocity extension step prior to advecting the level set function/fracture surface geometry. This function takes a rate that initially defined solely on the fracture surface and extends it across the level set domain using the local surface normal. Fext3D.m uses an explicit time integration scheme and only requires convergence within a small region near the fracture interface.

Level Set Function: gradPhi.m

Explicitly calculates the local gradient using forward or backward differencing (less computationally intensive then implicit methods). Forward and backward differences are first-order accurate. The differencing direction is chosen such that information propagates away from the interface. Boundary conditions follow the same logic that is outlined in diffPhi.m.

gradPhi.m is used when integrating and advecting the level set equation to alter the fracture surface geometry. More computationally efficient that diffPhi.m.

Level Set Function: heaviArea.m

Heaviside function that segregates the level set field into solid and liquid nodes. This function is used in calcB.m.

Level Set Function: integratePhi.m

An implicit integration method used during the reinitialization step. This method calculates the local gradient using a Godunov-based approach and performs a first-order Euler integration in time. Although this is more computationally expensive than the explicit gradient approximation (e.g. using gradPhi.m), this approach handles discontinuities in the level set field well and ensures numerical stability during the reinitialization process.

Level Set Function: readInput.m

Reads a text file that defines the reactive transport parameters. Please see structure of readInput.m to ensure that your input file is structured correctly.

Level Set Function: reinitPhi3d.m

Reinitialization function that is called after each level set advance. This function resets the level set function to a signed-distance function after the surface geometry is altered.

Run script: ADRE.m

This is the run script that couples the level set surface alteration to the reactive transport solver. The attached version of this script runs both the level set surface alteration and 1D vertical growth surface alteration model to provide the ability to compare simulation outputs throughout the reactive transport.

Run script: Input.txt

Input file that constrains reactive transport parameters. If you change the structure of the input file, please change readInput.m to ensure that each line is being interpreted correctly by the reactive transport solver.

Run script: runme.csh

A typical compilation script that compiles ADRE.m and runs the resulting executable. We ran this compilation code on an HPC node that executed the code in batch mode.